EADS INNOVATION WORKS

International Committee on Aeronautical Fatigue 2011

Review of Aeronautical Fatigue Investigations in Germany during the Period 2009 to 2011

Dr. Claudio Dalle Donne
Katja Schmidtke
EADS Innovation Works
CTO/IW-MS-2011

Review of Aeronautical Fatigue Investigations in Germany during the Period May 2009 to April 2011

Dr. Claudio Dalle Donne
Katja Schmidtke
EADS Innovation Works
CTO/IW-MS

CTO/IW-MS-2011-055 Technical Report
EADS Innovation Works

Title

Review of Aeronautical Fatigue Investigations in Germany during the Period May 2009 to April 2011

Author
Dr. Claudio Dalle Donne
Katja Schmidtke

Project-No.

Phone	Department/Work area	Date	Report-Nr.
+49-89.607 27728	CTO/IW-MS	May 2011	CTO/IW-MS-2010-055

Abstract

This review embodies a compilation of abstracts on aeronautical fatigue investigations in Germany during the period May 2009 to April 2011 and is presented within the scope of the Meeting of the International Committee on Aeronautical Fatigue in Montreal Canada, 29.-30. May 2011.

The contribution of summaries by German aerospace manufacturers, governmental and private research institutes, universities as well as aerospace authorities was completely voluntary, and is acknowledged with sincere appreciation by the authors of this review.

Enquiries concerning the contents should be addressed directly to the author of the corresponding summary.

Distribution to

CTO/IW-OP-IP-Patents (e-mail to Mrs. Rotter)
M&W Zander / KD – Dokumentenverarbeitung/Mikrofilm
Coverpage: CTO/IW – Yann Barbaux, CTO/IW-MG – Mr. Lindemann (via e-mail in pdf. format)

pages	photos	drawings	diagrams	tables
79				

Keywords for database
International Committee on Aeronautical Fatigue, ICAF 2011, National Delegate Review

1 Classification

1 generally accessible
2 free distribution inside EADS
3 confidential
4 highly confidential

Acceptance

Dr. Claudio Dalle Donne
Head of responsible department

EADS

Table of contents

1 Introduction

This review embodies a compilation of abstracts on aeronautical fatigue investigations in Germany during the period May 2009 to April 2011 and is presented within the scope of the Meeting of the International Committee on Aeronautical Fatigue in Montreal Canada, 29.-30. May 2011.
The contribution of summaries by German aerospace manufacturers, governmental and private research institutes, universities as well as aerospace authorities was completely voluntary, and is acknowledged with sincere appreciation by the authors of this review.
Enquiries concerning the contents should be addressed directly to the author of the corresponding summary.

Mailing addresses of contributing companies and institutes:

Abbreviation	Details
Airbus	Airbus Operations GmbH; Kreetslag 10, D-21129 Hamburg, Germany, www.airbus.com
Aleris	Aleris Aluminum Koblenz GmbH; Carl-Spaeter-Straße 10, D-56070 Koblenz, Germany, www.alumitechinc.com
Astrium ST	Astrium GmbH Space Transportation; Airbus-Allee 1, D-28199 Bremen, Germany, www.astrium.eads.net
Böhler	Böhler Schmiedetechnik GmbH &Co KG, Mariazeller Strasse 25, A- 8605 Kapfenberg, Germany www.bohler-forging.com
CTC	Composite Technology Center Stade, Airbus-Straße 1, D-21684 Stade, Germany, www.ctc-gmbh.com
DLR	German Aerospace Center DLR, Institute of Materials Research, Linder Höhe, 51174 Cologne, Germany, www.dlr.de
EADS IW	EADS-IW European Aeronautic Defence and Space Company, Innovation Works; D-81663 Munich, Germany, www.eads.net
Eurocopter	Eurocopter Deutschland GmbH; Industriestrasse 4, D-86607 Donauwörth, Germany, www.eurocopter.com
Fraunhofer Halle	Fraunhofer Institut für Werkstoffmechanik, Walter-Hülse-Straße 1, D-06120 Halle, Germany, www.iwm.fraunhofer.de
HS Osnabrück	University of Applied Sciences, Faculty of Engineering and Computer Science, Albrechtstr. 30, D- 49076 Osnabrück, Germany, www.ecs.hs-osnabrueck.de
HZG	Helmholtz-Zentrum Geesthacht; Max-Planck-Straße 1,D-21502 Geesthacht, Germany, www.hzg.de
IABGmbH	Industrieanlagen-Betriebsgesellschaft mbH; PO-Box 1212, D-85503 Ottobrunn, Germany, www.iabg.de
IFS	Academic Institute for Creating Fundamental Sciences; Augustenstraße 28, D-80333 Munich, Germany
IMA	IMA Materialforschung und Anwendungstechnik GmbH; Postfach 80 01 44, D-01101 Dresden, Germany, www.ima-dresden.de
IMR	University of Siegen, Institut für Mechanik und Regelungstechnik; Paul-Bonatz-Strasse 9-11, D-57076 Siegen, Germany, www.uni-siegen.de
LMW	University of Siegen, Research Group for Material Science and Material Testing; Paul-Bonatz-Strasse 9-11, D-57076 Siegen, Germany, www.uni-siegen.de
RUAG	RUAG Aerospace Structures GmbH; Friedrichshafener Straße 6A, D-82205 Gilching, Germany, www.ruag.com

Abbreviation	Details
Tata Steel	Tata Steel Research, Development & Technology, PO Box 10000, 1970 CA Ijmuiden, The Netherlands, www.tatasteel.com
TU Chemnitz	Chemnitz University of Technology, Composite Materials Group, D- 09107 Chemnitz, Germany www.wsk.tu-chemnitz.de
TUM LLB	Technische Universität München, Institute of Leightweight Structures; Boltzmannstr. 15, D-85747 Garching, Germany, www.llb.mw.tum.de
Uni. Cranfield	Cranfield University, College Road, Cranfield, Bedfordshire, MK43 0AL, Damage Tolerance Group, Building 88, UK, www.cranfield.ac.uk
Uni. Patras	University of Patras, Laboratory of Technology and Strength of Materials, Department of Mechanical and Aeronautical Engineering; Panepistimioupolis, Rion, 26500, Greece, m_papado@mech.upatras.gr
Uni. Porto	University of Porto, Mechanical Engineering Department, Faculty of Engineering; Rua Dr. Roberto Frias, 4200-465 Porto, Portugal, sergio.tavares@fe.up.pt

2 Full Scale Testing

2.1 Overview of Full Scale Fatigue Tests (May 2011)

Project	Customer	Test Structure	Schedule	Laboratory
A400M	Airbus-D	VTP to HTP lug structure (Attach-ment Fitting)	2007-2010	IMA
MERGE	Airbus-D	Several curved fuselage panels	2009-2010	IMA
BR-725 Engine	Rolls-Royce	Intermediate casing fatigue test	2009 - 2010	IMA
A400M-Doubler Ramp Panel	Airbus-D	Wing structure represented by a Flat Panel	2010-2011	IMA
A380 Skin Panel Fatigue Test	Airbus-D	VTP structure represented by Flat Panel	2010	IMA
A400M	Airbus-D	THSA Attachment Fitting	2008-2011	IMA
A380	Airbus	Fatigue Test	2003-2010	IABG / IMA
A380 EF	Airbus-D	Complete airframe	2005-2011	IABG
A320 NEF2	Airbus-D	Centre fuselage with both wings	2008-2010	IABG
A320 NEF3	Airbus-D	Rear fuselage	2008-2010	IABG
A400M	Airbus-D	Complete airframe	2011-2012	IABG

Table 1: Overview of full scale tests; currently running and/or finalised between 2009 and 2011

2.2 A380 Full Scale Fatigue Test - Provision of test infrastructure- Performance of specimen inspections

Dr. R. Buchholz, Prof. Dr. Th. Fleischer (IMA)

IMA Dresden contributes to Full Scale Fatigue Testing of the Airbus A380-800*. The principle task is the provision of test equipment (test hangar, hydraulic and pneumatic hardware) as well as its monitoring and maintenance during testing.
IMA Dresden is also primarily responsible for the regular inspection and Non Destructive Testing (NDT). Used Non-Destructive inspection methods are visual-, eddy-current-, ultra-sonic-, and x-ray inspection.

Figure 2.1 pump station (capacity 6000l/min, hydraulic test equipment)

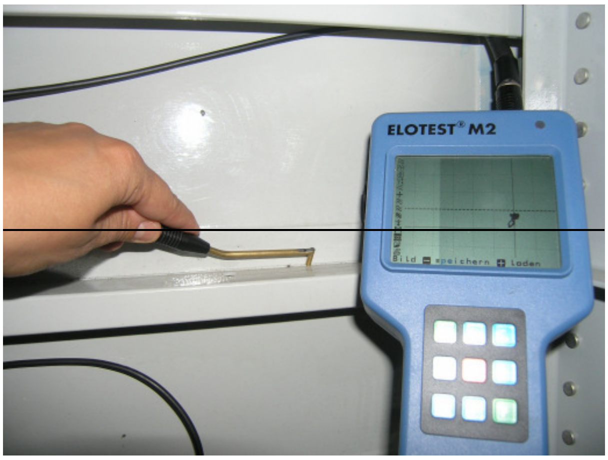

Figure 2.2 structure inspection

* …. in cooperation with the customer AIRBUS Operations GmbH and the main contractor IABGmbH

2.3 A380 Full Scale Fatigue Test

F. Eichelbaum (IABGmbH)

Throughout the years 2009 and 2010 IABG continued to conduct the A380 full scale fatigue test at its Dresden test site. End of 2010 2,5 A/C lifetimes have been demonstrated. By that time, some 75 special measurement campaigns had successfully been conducted by IABG.
The A380 fatigue testing is continued to take maximum benefit out of the test setup before the final phase of Residual Strength Test will be performed and before the specimen is being dismantled and investigated in Tear Down Inspection by Airbus Experts. IABG is responsible for the mechanical test set-up in terms of the loading rig, inspection rig, and loading trees as well as for the control- and monitoring and data acquisition systems, respectively and the more than 180 hydraulic actuators.

Figure 2.3 IABG experts inspecting the hydraulic loading system underneath the LH wing of the A380EF

2.4 Completion of the A320 Development Fatigue Testing Program

G. Hilfer (IABGmbH)

In 2007, IABG has been contracted by Airbus for defining the design, set-up and performance of the two major structure fatigue tests related to the continued development of the Airbus Single Aisle Family, namely the NEF2 (centre fuselage with both wings) and NEF3 (rear fuselage) tests.

In support of the analytical development of fatigue and damage tolerance capabilities of the A320 family aircraft, the performance of min. 180,000 **S**imulated **F**lights (SF) on each of the two major airframe structures is requested. The first test phase until 2009 has been presented at the ICAF Symposium 2009.

Since then, fatigue testing has continued to make major progress so that the two fatigue testing programs which were scheduled to run until mid of 2011 were completed already by summer/autumn 2010. As an example, the test progress of NEF2 is displayed in Figure 2.4. This outstanding test progress was achieved as a result of various measures and optimizations implemented already during preparation and further on during operation of the tests.

As in previous tests, the performance of comprehensive systems simulations proved to be a valuable tool not only to gain design data for the hydraulic system but also to shorten commissioning and the subsequent optimization of control parameters significantly.
The repair support by IABG using qualified personnel helped to reduce the coordination effort of external repair teams, travel cost and overall processing time of repairs.

A detailed analysis of all test systems based on the specific requirements of these two tests brought forth further improvements for the loading program on Airbus side as well as for control parameters and the pneumatic system on IABG side.

Efficient maintenance procedures as well as a tailored redundancy and spare parts policy enhanced facility availability up to 98.2%.

The entire package of implemented improvements resulted in a test speed increase of more than 30% with respect to the initial value while maintaining measurement accuracy and facility availability.

Figure 2.5 displays the test speed which was achieved for the NEF2 and NEF3 tests. An overall average test speed of approximately 1.1 (NEF2) to 1.4 (NEF3) seconds per load case was reached. This test speed value includes the pressurisation and depressurisation load cases of the fuselage. Without the pressurization and depressurization cycles which affect the overall speed considerably, the average load cycle time is reduced to 1.0 (NEF2) and 0.87 (NEF3) seconds, respectively. These average values give an impression of how fast the mechanical load cycles have been applied considering the size of the structures, the significant number of control channels involved and the large displacements particularly at the wing tips.

According to the ESG test schedule, the remaining work on the testing program consisting of the preparation and performance of the residual strength test campaign is underway.

A dedicated publication about the fatigue test completion phase of this testing program as well as an oral presentation will be part of the ICAF 2011 symposium.

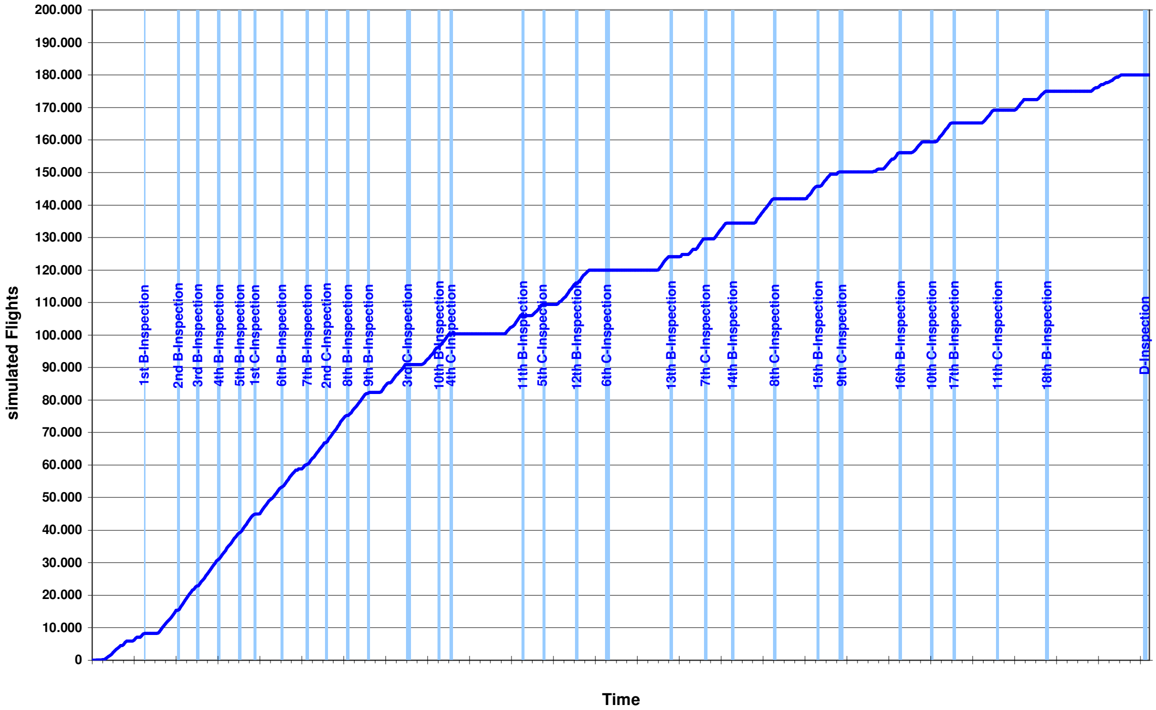

Figure 2.4 Test progress of NEF2

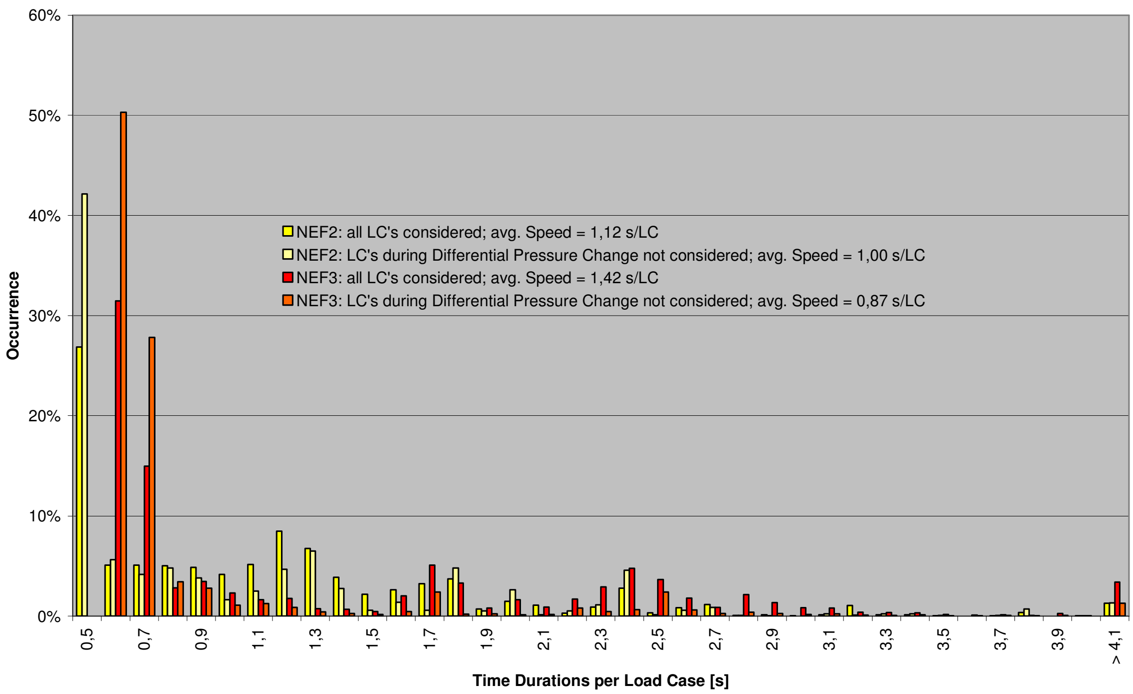

Figure 2.5 Test speed

2.5 New Connection Strap Concepts for A320 Main Landing Gear Area tested during the recent A320 Full Scale Fatigue Development Test

N. Cenic, B. Zapf (RUAG)

The full scale fatigue development test of Airbus A320 took place at the IABG test site in Ottobrunn, Germany in 2009 and 2010. It provided a possibility to test new connection strap concepts in the wheel well area of the main landing gear (Figure 2.6). The goal of the test campaign was to gain a better insight into the structural behaviour of the MLG bay area with different connection straps installed at the location marked in Figure 2.6 and Figure 2.7 under the simulated flight and ground loading conditions.

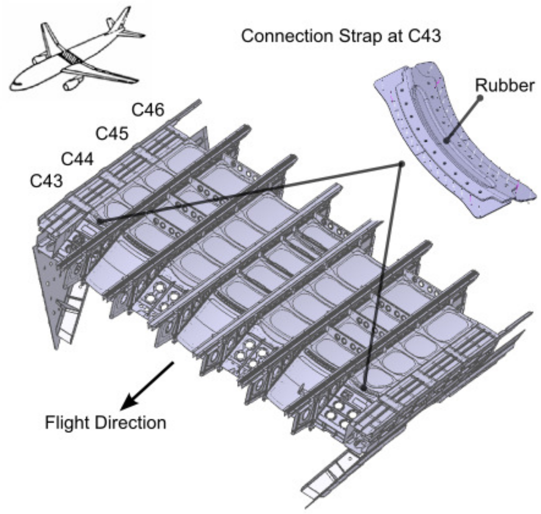

Figure 2.6 Floor Section of A320 MLG Area with the existing connection strap concept

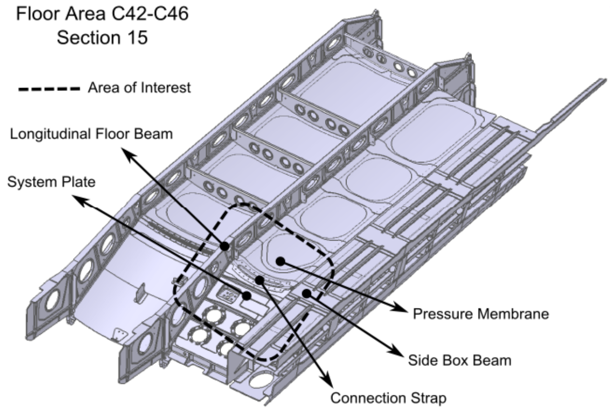

Figure 2.7 Structural elements of interest for the test campaign

In order to improve the fatigue strength of damage tolerant Principal Structural Elements an approach was taken to modify the load distribution within the MLG Bay Area by replacing rubber connection straps with a more effective load carrying solution. Five different connection strap concepts were tested by installing them in the test airframe. Two concepts were based on 2024 Aluminum, two on CFRP and one was a fiber-metal laminate (Figure 2.8). The test loading was based on the most damaging fatigue load cases. The effect of different connection straps on the structural behavior was monitored using strain gauges, displacement transducers and an ARAMIS deformation measurement system. The prediction of the crack growth rate in the Side Box Beam flange was accomplished using Forman's formulation and an edge crack stress intensity function calibrated with the full scale fatigue test evidence. The effects and trade-offs between different connection strap designs were analyzed with respect to fatigue, damage tolerance and weight saving opportunities.

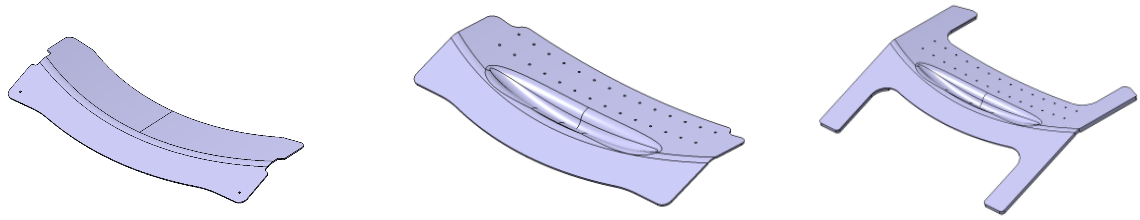

Aluminum 2024 | CFRP | Fiber-Metal Laminate

Figure 2.8 Different Connection Strap concepts that were developed and tested

2.6 FE-Model validation by GOM ARAMIS - Optical 3D Deformation Analysis

S. Hotter, B. Zapf, N. Cenic (RUAG), J. Hoffmann (TUM LLB)

Optical Metrology has been found to be a very user friendly technology for validating FE-Models in the A320 Full Scale Fatigue Development Tests (FSFDT) Programme. Since the year of 2010, RUAG in partnership with TUM, has investigated the possibilities of implementing optical 3D measuring techniques from GOM-ARAMIS ® towards verifying the accuracy of FE-Analysis deformation results. Essentially this deformation under load results comparison procedure is used for validating FE-Models by comparing the deformations obtained numerically, with those deformations obtained by means of optical metrology on the 1:1 scale testing facility at IABG. See Figure 2.9.

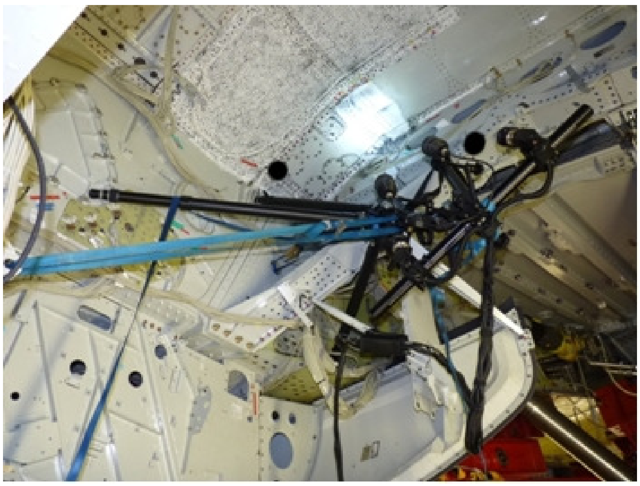

Figure 2.9 Optical Metrology rig from GOM-ARAMIS on the full scale A320 testing facility at IABG in Ottobrunn.

To make FE-Model validation even more user friendly and reliable, RUAG in cooperation with GOM and TUM LLB, have recently developed an interface that makes it possible to post process numerical FEM deformation results obtained from NASTRAN. This Interface enables the direct comparison of numerically and optically obtained deformation results by a best-fit overlaying. Differences of the optical measured test results and the calculated FEM results are later visualized and quantified in GOM ARAMIS. Currently RUAG is implementing this optical metrology technique inside the A320 FSFDT Project for validating the DFEM-GFEM FE model integration. Process “Fine Tuning” and an appraisal of this optical technique´s tolerances and implementation limitations are right now our main development tasks towards verifying and validating the procedure itself. See Figure 2.10 and Figure 2.11.

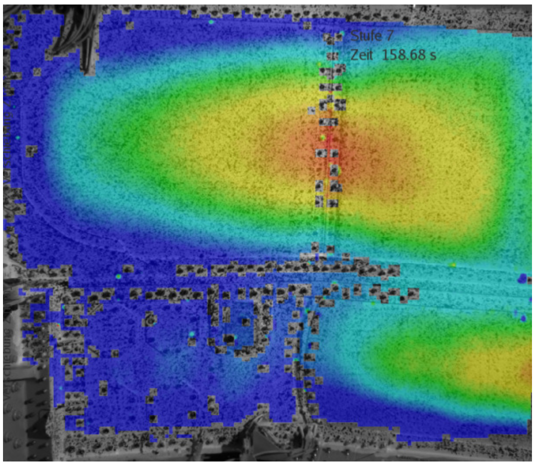

Figure 2.10 Digitized deformation results obtained on the full scale testing facility

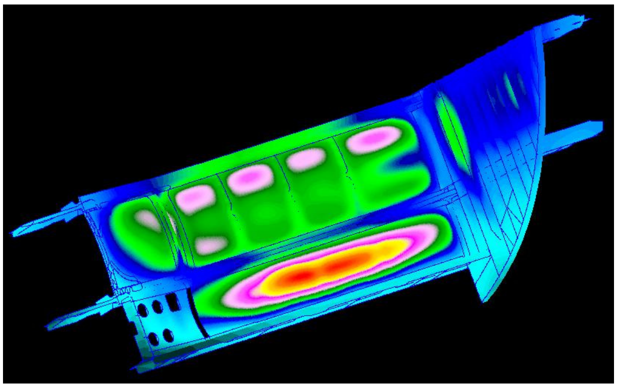

Figure 2.11 Analytically obtained deformations on the Detailed FE Model (DFEM) after integration in the General FE Model (GFEM)

2.7 Detailed FE Model of A320 Lower Side Shell Section 15

B. Selk, R. Parenti; B. Zapf (RUAG)

Within the scope of the A320 Full Scale Fatigue Development Test Program, a detailed FE Model (*DFEM*) for the Lower Side Shell has been built and integrated in the Global FEM of Section 15 (*GFEM*) provided by Airbus. Parts modelled with a fine mesh (element size around 8mm) include: side box, rear and forward skin with stringers, slanting frames. Connections elements (bolts, rivets) are singularly modelled.

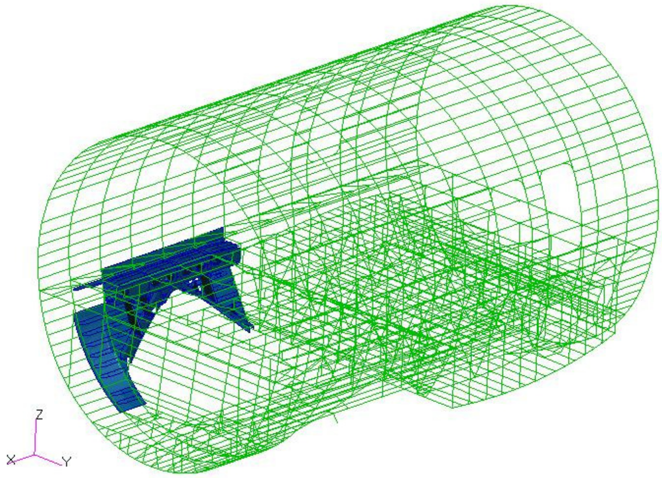

Figure 2.12 Location of the DFEM in the Global FEM of Section 15

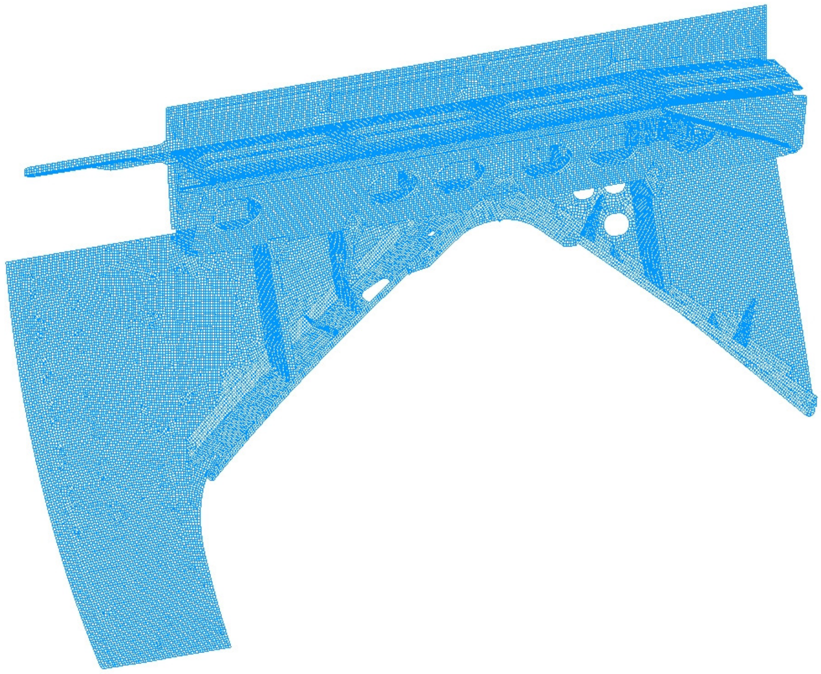

Figure 2.13 Overview of the DFEM

The DFEM can be used for several purposes: it allows a detailed static and fatigue analysis for the parts which are finely modelled. Each part, fasteners included, can be singularly verified as a result of more realistic load paths. The DFEM is also used for a comparison between FE simulation and test results.
The integration of the DFEM is accomplished by means of RBE3, which can transfer loads and deformations from the GFEM. For this reason, no additional definition of boundary conditions is required.

2.8 A350 Full-Scale Fatigue Tests - Status

W. Göbel (Airbus)

Currently the full-scale fatigue tests for A350XWB are in preparation. These tests form the most upper level of the A350XWB test pyramid (sometimes also called building block approach) supporting Means of Compliance (MoC) for metallic and composite fatigue and damage tolerance together with an ES static test, EW wing box and fuselage barrel composite fatigue and damage tolerance tests.

The fatigue tests are performed in line with the airworthiness rules EASA CS 25.571 and FAA FAR 25.571 (including the new rule for WFD issued Jan. 2011).

The test objective is focused on Metal and Composite Fatigue and Damage Tolerance, i.e. damage initiation and damage propagation.

The tests are representing the primary structure of the airframe, i.e. fuselage and wing.
Load introduction dummies representing the landing gears, pylon, moveables, horizontal and vertical tail plane (HTP and VTP).

The EF1 consists of cockpit and fwd fuselage sections 11, 12 and partially section 13. Center Fuselage section 15 and center wing box section 21 and a pair of wings are forming the EF2. The EF3 major test includes the aft fuselage section 18 and 19. The EW-test consists of a left wing clamped to a dummy center wing box.

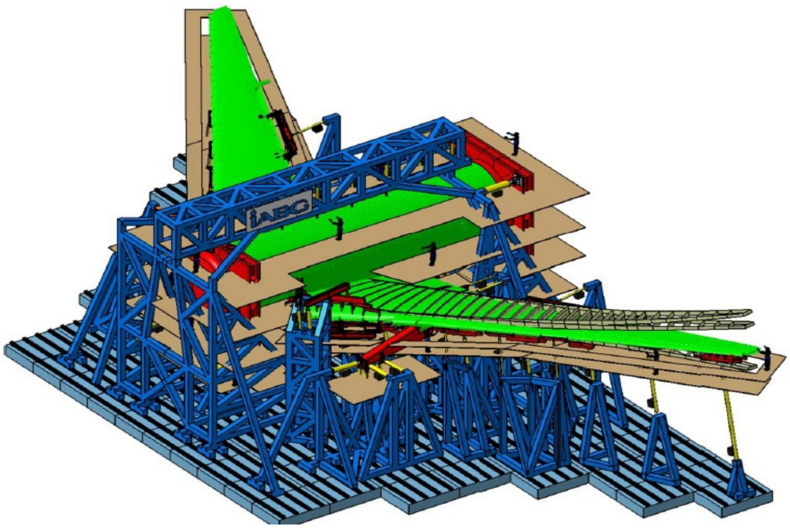

Figure 2.14 A350XWB EF2 Test

The external loads will be simulated by about 8 to 88 jacks (dependent on the test), distributed by loading trees to wing ribs or fuselage floor structure.

The loading programme will simulate a minimum of 1 ½ up to 3 design service goals, representing the anticipated typical aircraft usage of a mission mix with short, medium and long range flights. The flight-by-flight sequences will include pressurisation of fuselage, vertical and lateral gusts, vertical and lateral manoeuvres, rotation/lift-off, landing and all events occurring during ground operation like towing/pushback, turning, braking, taxiing, take-off run, landing run.

The test will be split into three major phases 1. fatigue (damage initiation), 2. damage tolerance (damage growth) incl. artificial damages and finally 3. residual strength.

Frequent inspections will be scheduled during the test. These inspections could be general visual, detailed visual and non-destructive inspections.

An artificial damage programme will support fatigue and damage tolerance analysis with damage growth measurements under load redistribution. Monitoring of “accidental damages” and repairs of artificial damages will support development and validation of the structure repair manual (SRM) and establishment of the structure maintenance programme.

Measurement of strains or deflections with strain gauges, ARAMIS system for out of plane displacement measurements, e.g. global buckling pattern and comparison with DFEM, photostress for full field strain measurements and deflection transducers for displacement measurements will be defined.

The test houses EF1 at CEAT in Toulouse, EF2 at IABG in Munich, EF3 at Airbus in Hamburg and EW at IABG in Munich are meanwhile selected.

The test definition phase is nearly completed, i.e. the structure configuration for the test is defined, the jack positions, strokes and sizes are defined, sizing data for rigs delivered to the test houses.

Next steps will be the generation of the loading programme and detailed definition of measurement locations (strain gauge positions) will continue until test start.

Test start is planned for June 2012 and Jan 2013 and will last until end of 2014.

2.9 Automatic Fatigue Spectra Generation - A350 XWB Rear Cargo Door Surround

E. Yip, N. Cenic, B. Zapf (RUAG)

Fatigue and Damage Tolerance Calculations during design and development stages were performed for the A350 XWB Rear Cargo Door Surround. Calculations were made using Airbus Stress Tools ISAMI and ISSY/DYNFEST in addition to a set of in-house developed tools used for estimating unit fatigue stresses and creating related fatigue spectra. Due to inability of Airbus Stress Tools to access and use directly the stress results of RUAG's detailed FE model of the Rear Cargo Door Surround a set of tools including Microsoft Excel VBA macros and Linux scripts were developed to speed-up structural verification with respect to F&DT. The tools act as a link between the detailed FEM and Airbus Stress Tools and they convert the unit stresses of 1D and 2D FE elements into corresponding fatigue unit stresses using fatigue load case definition files supplied by Airbus. The obtained fatigue unit stresses are then formatted to match the required input format for further processing using the Airbus Stress Tools. The ultimate goal is to automate the process in such a way that minimal manual manipulation is required and the fatigue spectra for locations of interest can be generated quickly and efficiently directly from the detailed FEM.

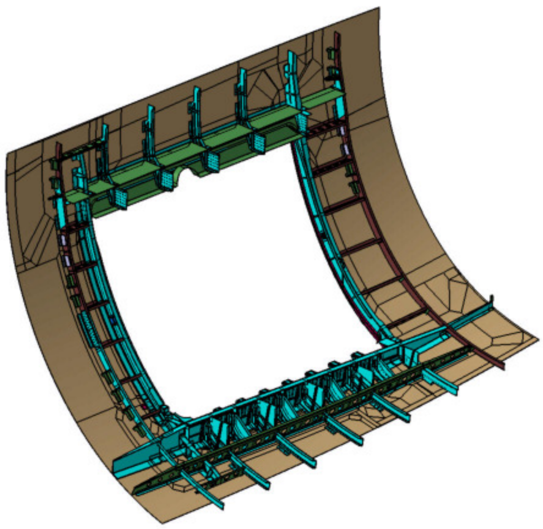

Figure 2.15 DMU A350 XWB – Rear Cargo Door Surround

2.10 Engine Structure Test

M. Semsch (IMA)

IMA Dresden performed fatigue test of an magnesium aircraft engine component in 2009 and 2010. Special dummy structures were designed and manufactured to ensure correct loading of the specimen. These dummy structures replaced the bypass duct, fan case and accessory gearbox. The challenge of designing dummies is to meet the correct stiffness of the original part. All additional adjoining parts were original engine components.

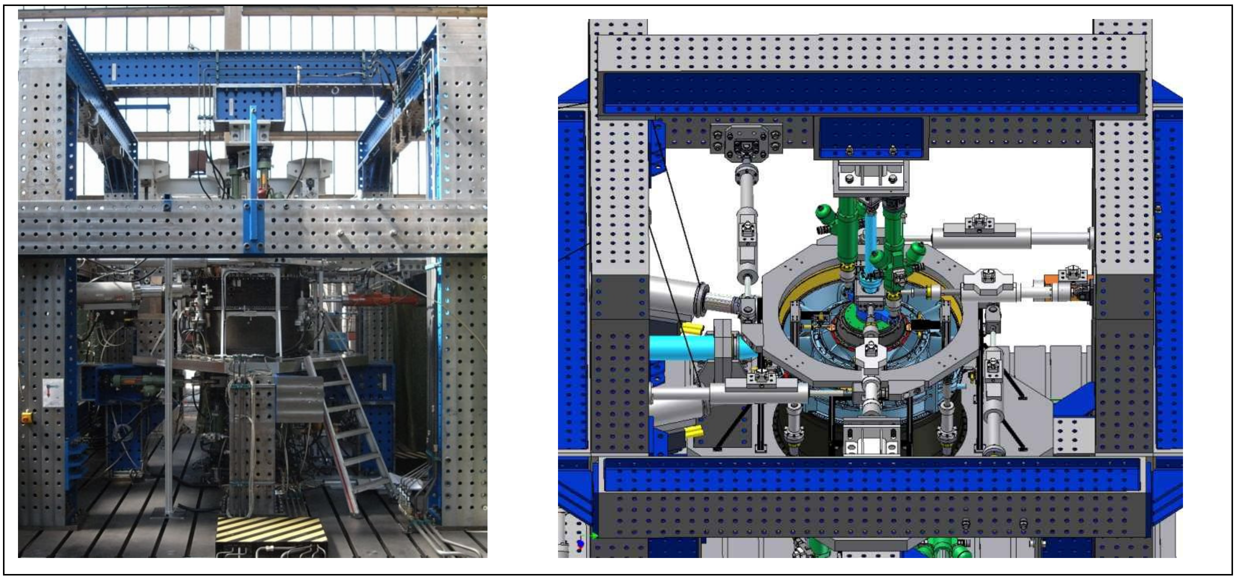

Figure 2.16 Test set-up

In total, 31 hydraulic actuators were used to load the specimen at different flanges and at bearing supports. The high number of forces and the locations to be loaded required some sophisticated actuator set-up. The instrumentation consisted of 120 strain gauge channels and 48 displacement sensors.

2.11 Rolls Royce BR725– Rear Mount Ring Static and Fatigue Tests

O. Tusch (IABGmbH)

The titanium rear mount ring (RMR) of the Rolls Royce BR725 turbine engine has been exposed to a series of static tests and fatigue testing at the IABG test laboratories, Ottobrunn, Germany.

The test specimen has successfully demonstrated the strength of the rear mount. At the beginning of 2010 the fatigue test has been completed with the fulfillment of test requirements of the rear mount ring.

The test specimen was integrated between two CFRP dummies. IABG was responsible for the design and build of these dummies which had a customized stiffness distribution similar to the adjacent engine bypass duct structure and the engine thrust reverser unit. The loading of the specimen has been introduced by 16 hydraulic actuators which were acting onto the inside and outside of the rear mount ring structure and onto the dummy structures. The limited internal diameter of the test article and the number of actuators defined to apply the internally acting loads required a very efficient usage of the available space.

The test specimen has been instrumented with 63 strain gauge channels applied on titanium and 24 displacement transducers. Measurements were taken during the fatigue cycling of approximately 140.000 load cycle.

Figure 2.17 Test Set-up of the BR725 Rear Mount Ring test

2.12 Information Management for Aircraft Structural Tests

V. Kempe, Dr. R. Buchholz (IMA)

The performance of aircraft structural and component static or fatigue tests include inspection work. IMA Dresden developed a proprietary information management system which provides an optimised base for planning of inspections while aircraft structure tests. It includes all required information, like

- inspection requirements,
- inspection results, status,
- analysis of results,
- further resulting actions or new requirements etc.

This system allows the management of different test project using the experiences from each other.

The initial inspection requirements include information regarding location, inspection method, inspection threshold and interval. The results of each inspection work are documented into the system. Based on these entries the further actions according to occurred damages will be defined, for instance

- extended inspection requirements (second method, extended area),
- shortened inspection interval,
- repair or modification procedures.

Furthermore, after modification or repairs the resulting status is documented by this system. The information management system consists of four parts:

- Part 1 Area Inspection: It includes the data for inspection of predefined areas. The job cards describe the inspection requirements for these areas.
- Part 2 Damage Inspection: The inspection of existing artificial or natural damages will describe in Part 2. The job cards describe specific inspection requirements.
- Part 3 Inspection Result: The inspection results are the central part of the information management system. The digital documentation of the inspection results is the basis for parameters of further inspection requirements which will be implemented into Part 1 or 2.
- Part 4 Status: It allows analysing of the status of inspections as well as the status of result analysis.

The Parts 1, 2 and 3 contain procedures which allow the monitoring of each inspection item regarding status, analysis and documentation. These procedures are available at any time. Part 4 provides the current status of the whole test campaign regarding the visualisation of progress, inspection work und damages.

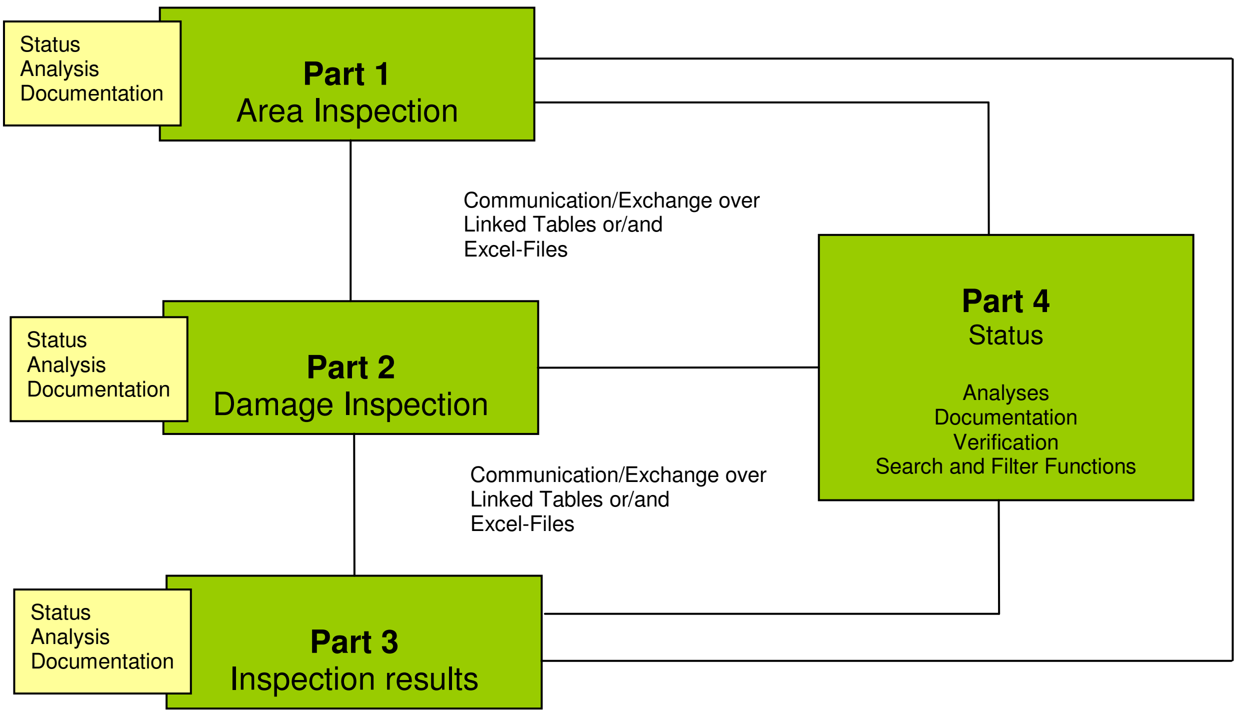

Figure 2.18 Master Plan

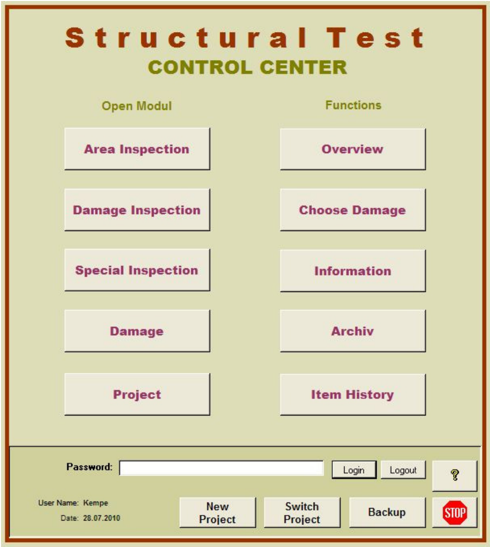

Figure 2.19 Main Menu – Control Center

2.13 Static and Fatigue Testing of the Main and Nose Landing Gear of a medium sized Helicopter

N. Abramovici, G. Hilfer (IABGmbH)

The nose landing gear (NLG) and main landing gear (MLG) of a medium sized helicopter will be tested within the scope of qualification by IABG. The qualification test program planned from September 2011 to December 2012 includes static tests up to ultimate load and 4 lives of fatigue testing.

For each test article, the retraction/extension (R/E) loads will be realized with 1 hydraulic jack (RTJ = retraction jack) at the position of the retraction actuator and the ground loads with following jacks to the wheel axle:

- Each of both NLG wheels will be replaced by one wheel dummy loaded with 3 jacks:
  - 1 X jack on the wheel axle (drag load),
  - 1 Y jack at the floor contact point (side load) and
  - 1 Z jack and 1 Z strut with resulting load on the wheel axle (vertical load).

- The single MLG wheel will be replaced by one wheel dummy loaded with 5 jacks:
  - 1 X jack on the wheel axle (drag load),
  - 1 X jack at the floor contact point (brake load),
  - 1 Y jack at the floor contact point (side load) and
  - Z jacks with resulting load on the wheel axle (vertical load).

Each test article will be tested at different shock absorber positions (SAT = shock absorber travel) and with different roll radius (RR = distance between wheel axle centre and floor contact point, i.e. Z position of the side and brake jacks on the wheel dummy). Furthermore, all X, Y and Z jacks have to be positioned at the start of each strength test such that they will be aligned exactly in X, Y or Z direction at the maximum test article deformation corresponding to the maximum load level. All these different test configurations require a modular test set-up for which IABG chose to design the test rig for its MTA (Modular Test Area), which is composed of a clamping plate, numerous modular rig parts and an entire dedicated supplies infrastructure consisting of electrical, pneumatic and hydraulic power as well as appropriate data acquisition systems and control and monitoring systems.

The test articles will be instrumented with strain gages and displacement transducers and regularly inspected by Non Destructive Testing (NDT).

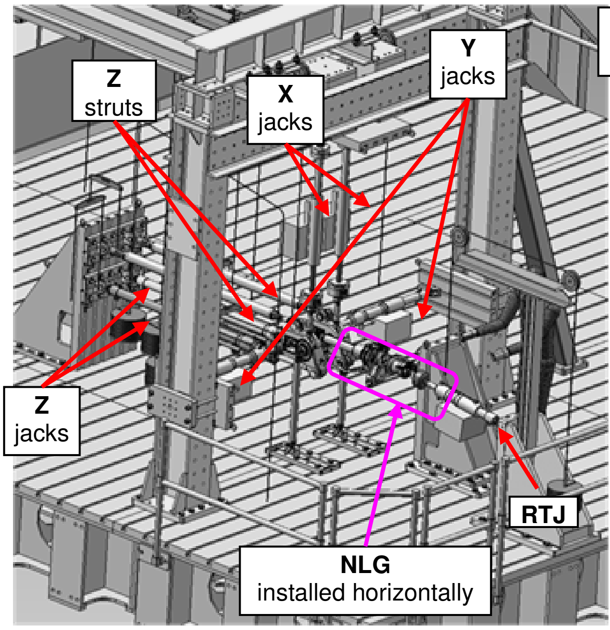

Figure 2.20 NLG test set

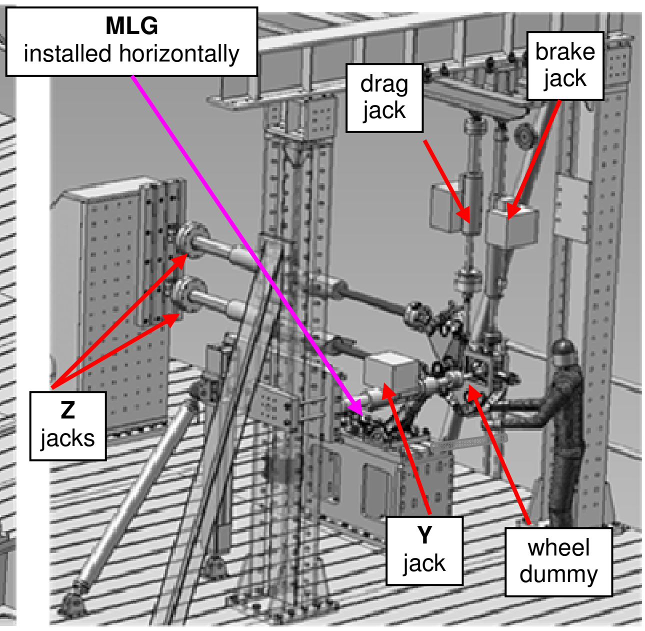

Figure 2.21 MLG test set up

2.14 Lifetime calculation of titanium tubes considering ovality due to bending process

F. Blume (Eurocopter)

It is known that the ovalities have a significant impact on the fatigue life of hydraulic pressure tubes. The definition of ovality can be seen in Figure 2.22.

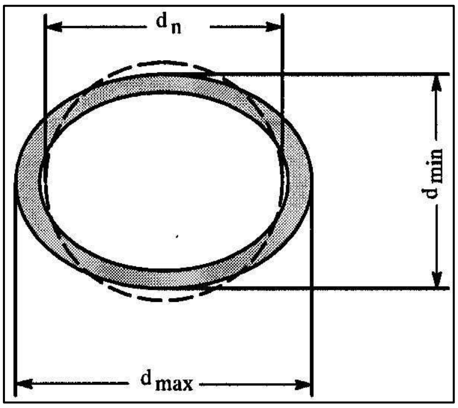

$$\text{ovality}\,(\%) = \frac{d_{max} - d_{\min}}{d} \cdot 100$$

Figure 2.22 Definition of ovality

Analytical investigation

At the beginning the influence of different ovalities on the overall stress was investigated with the Finite Element Method (FEM) with following parameters:

- Inside pressure 280bar (28 MPa),
- Tube bending radius 3*d,
- Bending angle 120° *
- Ovality variation from 0% to 15%

In order to visualize the effect of ovality, a diagram with stress increase versus ovality was created with the calculation results. (Figure 2.23)

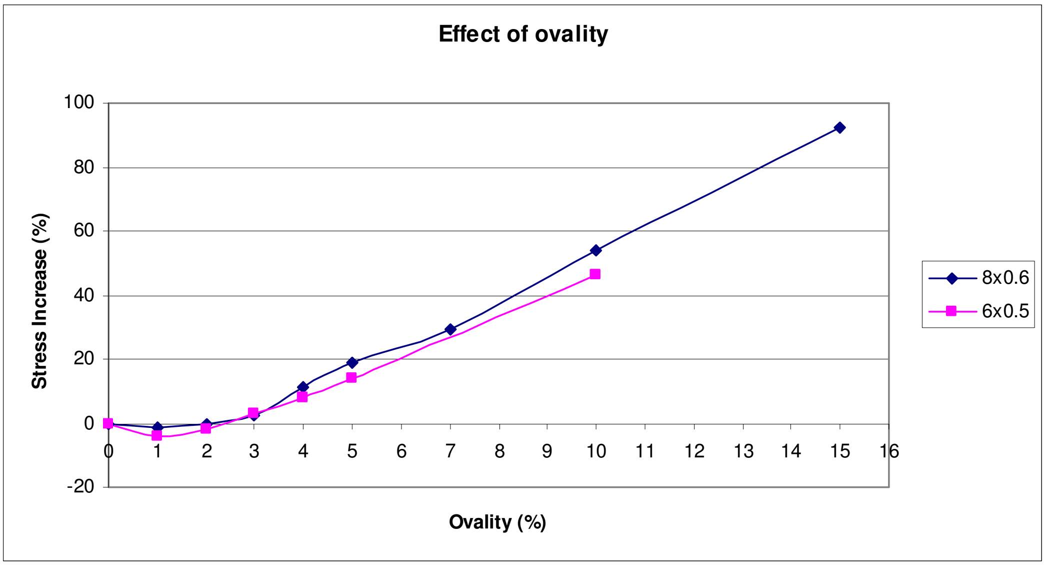

Figure 2.23 Von Mises stress increase (%) vs. ovality (%) for diameter 6 mm and 8 mm

As shown in Figure 2.23, the stress decreases slightly when ovality is between 0% and 2%. The explanation to this phenomenon can be the increasing radius in the inner wall of the pipe.

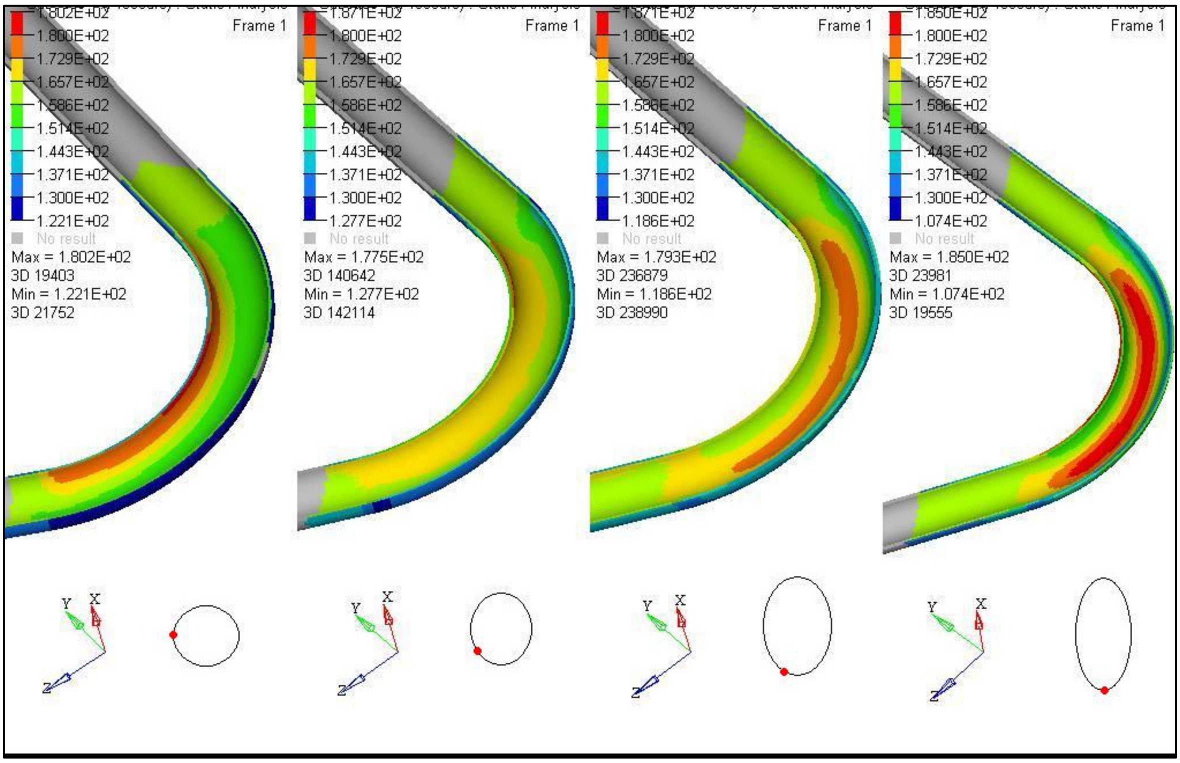

Figure 2.24 Von Mises stress distribution with increasing ovalities

Figure 2.24 shows how the stress distribution changes with respect to ovality. The stress peak area transfers from the inner wall of the pipe to the top and bottom walls of the tube where the cross-sectional radius decreases.

Fatigue Test

In order to determine the fatigue limit of pressure tubes with potential ovality, impulse fatigue tests were performed with titanium tube samples with diameters DN5, DN6, DN8, DN10 mm and max. ovality 12.5%. The tests were performed according MBBN 6001-6003 and ISO 6772.

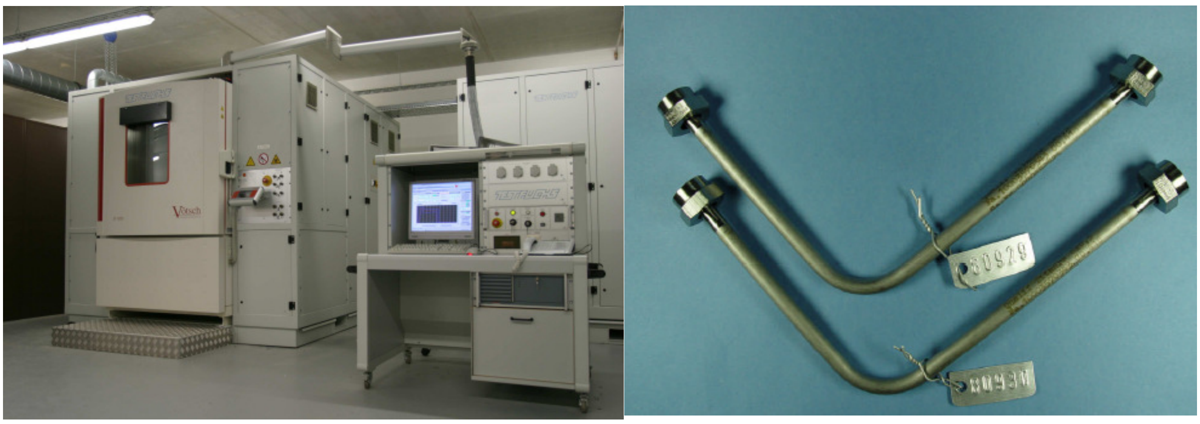

Figure 2.25 left side Test Bench; right side Test Samples

The test results showed that the amount of ovality has a significant influence on the fatigue potential but the great amount of scatter also shows that it is not the only contributing factor. Further investigation showed that the combination of ovality with different geometrical parameters (constriction, wall thinning, grooves) caused by the bending process leads to an early failure of the tube. Figure 2.26 shows an S/N curve for a titanium tube with DN8 mm.

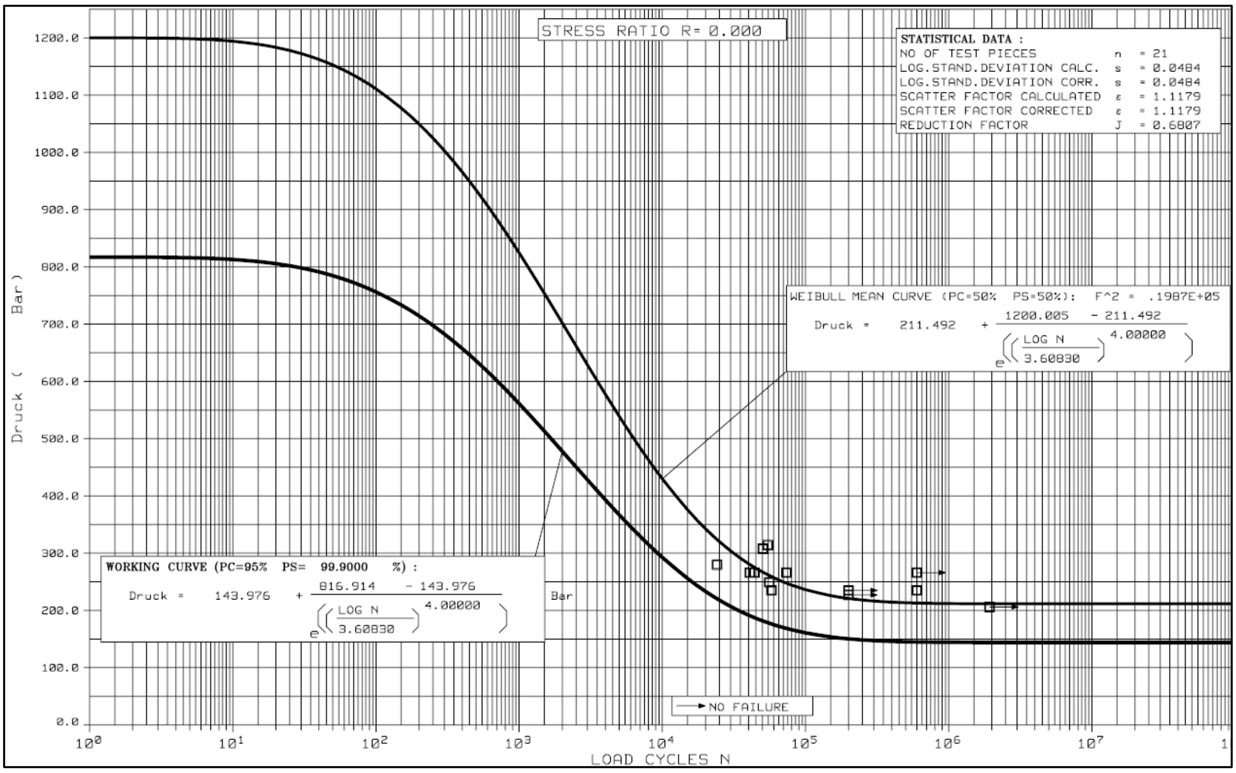

Figure 2.26 S/N curve for titanium tubes with DN8

References:

[1] F.Blume T291M0505E01, Lifetime calculation of titanium hydraulic tubes

2.15 ALCAS – Advanced Low Cost Aircraft Structures

A. Bertsch, H. Istok, A. Hofmann, V. Steffke, B. Zapf (RUAG)

ALCAS is a European Commission co-funded integrated project which was started in 2005 and will be completed by the end of April 2011.

The purpose of ALCAS is the investigation of different materials and manufacturing methods on a carbon fibre reinforced composite horizontal stabilizer which is based on the Falcon 7X Horizontal Tail Plane architecture.

RUAG Switzerland Ltd. is responsible for the complete structural static and dynamic testing of this validation article. Within this project RUAG Aerospace Structures GmbH, Oberpfaffenhofen near Munich, has been in charge for the design and the analysis of the 4 loading systems and the test rig. The design of the parts has been carried out as welded steel assemblies. Provisions for the installation of 14 low-friction servo-valve controlled hydraulic actuators have been made.

With the installation of the hydraulic equipment and the validation article the test set-up has been completed. The static and fatigue testing have been successfully completed. Rupture of the validation article upper panel at the root section was reached during the last static session. Throughout the whole test campaign the test equipment was fully reliable and performed as planned.

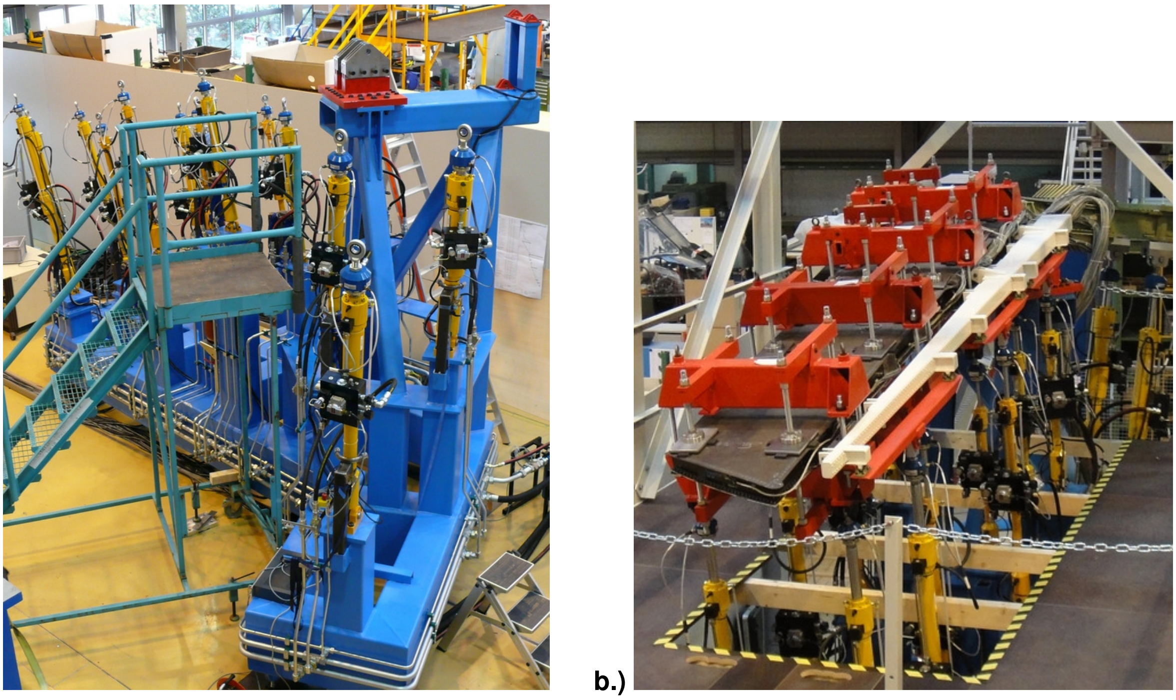

a.) b.)

Figure 2.27 a.) Test rig (equipped); b.) Loading systems + validation article

Acknowledgements
The research leading to these results has received funding from the European Community´s Framework Programme FP6 under the contract AIP4-CT-2005-516092.

3 Fatigue and Fracture of Fuselage Panels and Joints

3.1 Curved Panel Fatigue and Damage Tolerance Testing

M. Semsch (IMA)

For the Airbus research project MERGE (Metallic Fuselage next Generation) fatigue and damage tolerance tests of three new metallic fuselage concepts were carried out at one of IMA Dresden's curved fuselage panel test rigs. Airbus' objective is the development of thin metallic stiffened fuselage shells with a large damage capability (LDC) of the structure. One of the panels was manufactured out of advanced Al-Lithium materials inclusive new design principles for skin and frame.
The matter of particular interest for this test was the application of a new skin material development regarding damage tolerance properties as well as a new frame concept concerning material, design and manufacturing process.

Four artificial damages, circumferential cracks, were introduced before the test start. Configuration was across broken stringer as well as in-between two stringers. Crack propagation values were obtained by loading the panel with a flight spectrum.
Another artificial damage, a longitudinal crack across broken frame, was introduced after that cycling. It was again subject to cyclic loading. After reaching an extension of a 2-bay crack, the residual strength in terms of over-pressurization, was determined.

Figure 3.1 Panel after failure

3.2 Friction Stir Welding – Overlap Joints Performance Overview

S.M.O.Tavares (Univ. Porto), M. Papadopoulos (Univ. Patras), M. Pacchione (Airbus)

The application of new joining processes in the production of airframes will lead to significant improvements in structural efficiency, as in the case of integral structures with Friction Stir Welding (FSW) butt joints that present high joint efficiencies with very low defect rates. The application of FSW in an overlap configuration might be an attractive replacement to the riveting process for the assembly of fuselage primary structures, due to the similarity in tolerance management, which makes its implementation easier in comparison to other joint geometries such as butt welds.
Static and fatigue strength of this joint geometry were assessed and analyzed through an experimental program on AA2024 sheets comprising several configurations such as single and multiple welding passages and different tools, coordinated by Airbus.
Cross-sectional analysis and mechanical tests indicated that the joint strength is strongly depending on the welding process parameters and configuration. As regards static strength, it was observed that values close to the base material strength can be achieved. However the fatigue strength is low, as mentioned in the literature, [1-2], and might be unrealistic for primary struc-

tures. This weakness is instigated by the material flow, that originates a hook shaped unwelded defect at the interface of the plates near the nugget, highly detrimental to the fatigue properties, Figure 3.2 a).
The low fatigue strength of FSW overlap joints in high-load transfer configurations restricts their potential application in primary structures, where high fatigue resistance is imperative. The understanding of the relationships between the welding parameters, the weld configuration and the mechanical properties of the welds is necessary before the welding process can be optimized. In addition, a corrosion protection concept needs to be developed and assessed in order to ensure the structural integrity under all service conditions.

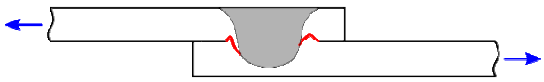

Single pass weld

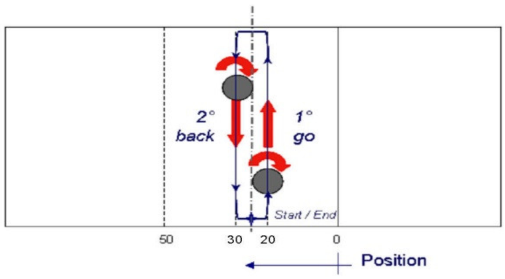

Double pass weld

a) FSW overlap typical interface defect b.) Distance between FSW passages

Figure 3.2 Overlap weld FSW configuration

Experimental Procedures

In frame of the European Union project COINS, FP6-2005-Aero-1, Contract No. AST5-CT-030825 overlap friction stir welded samples were manufactured at EADS-IW, Ottobrunn, using conventional tool and at EADS-IW, Suresnes, using a bobbin tool. The overlap welds with the standard tool composed by a Ø13 mm shoulder and a Ø5 mm pin, were performed with a forging force of 8kN, a welding speed of 140 mm/min and a rotational speed of 500 rpm. The overlap welds with the bobbin tool (through thickness) were performed with forging load of 0kN, welding speed of 100 mm/min and a rotational speed: 500 rpm. A total of 10 different configurations were welded in AA2024-T3 bare, no clad, plates with 250mm (clear length) x 50mm (width) x 2mm (thickness of each plate), and overlapped 50 mm. In these configurations was applied different number of passages (1, 2 and 3 passes) in each joint and with different distances, Figure 3.2 b). Three tensile tests and six fatigue tests were performed at Patras University from each specimen configuration.

Results

The lowest tensile strength was obtained with the single line welds. The double line welds showed an increase of the weld efficiency with the increase of the transition distance between the passages. The best performance was achieved with double pass weld distanced of 30mm. The same variation is reached for triple passage weld specimens, with a highest efficiency in this configuration achieved in the welds distance 20 mm (40 mm between the inner and outer weld). The highest efficiency was achieved by the double weld configuration using a bobbin tool, where the tensile strength of the weld was very close to that of the base material.
No direct correlation of fatigue performance with static strength values was found. The best fatigue performance was obtained with the double weld configuration using a bobbin tool, particularly for high stress amplitudes, whereas for lower stress amplitudes this effect was less pro-

nounced. Figure 3.3 shows the tensile and fatigue strength efficiencies for the different welding configurations compared to the respective properties of the base material.

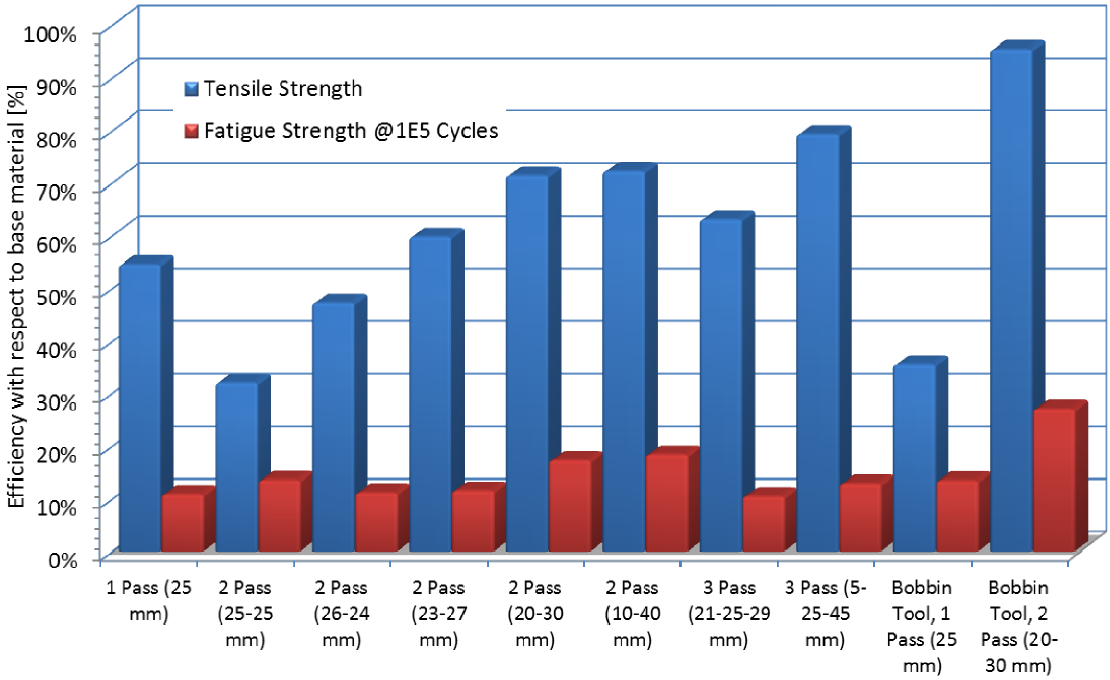

Figure 3.3 Static and fatigue strength efficiencies, comparison to the base material.

Conclusions

Tensile strength of FSW overlap joints can be improved with multiple welding passage lines and the increase of their distance improves the static strength. Static strength very close to the base material value is feasible with proper tuning of the welding process parameters and configurations. However, the increase of tensile strength of overlap welds does not necessarily lead to an increase of fatigue properties. The latter are possibly dominated by the welding defects whereas the tensile strength is connected to the distance between the outermost welds. Welds performed using a bobbin tool and multiple weld lines exhibited the best tensile strength and the best fatigue properties. Nevertheless, the fatigue performance of FSW overlap joints is very poor compared to the respective behaviour of the base material, due to the interface defects. The application of FSW in overlap configuration for structures with high fatigue requirements is not recommended.

References

[1] L. Cederqvist and A.P. Reynolds, ‘Factors affecting the properties of friction stir welded aluminum lap joints’. Welding Journal Research Supplement, pp. 281-287, 2001.

[2] M. Ericsson, R. Sandstrom, ‘Fatigue of FSW overlap joints in Aluminium welded with different tool designs’. In: Fifth International Symposium on Friction Stir Welding, September 14-16, 2004, Metz, France.

[3] S.M.O.Tavares, M. Papadopoulos, M. Pacchione; ‘Mechanical Behaviour of Friction Stir Overlap Welds for Aeronautical Applications’; 1st EASN Association Workshop on Aerostructures; October 07-08, 2010; Suresnes, France.

3.3 Biaxial Fatigue Tests on Friction Stir Welded Aluminium Lithium

V. Richter-Trummer (Univ. Porto, HZG), P. E. Irving and X. Zhang (Univ. Cranfield), M. Pacchione (Airbus), M. Beltrão and J. dos Santos (HZG)

Biaxial fatigue crack growth tests have been performed on friction stir welded aluminum lithium AA2198-T851. The influence of the welding process, the alloy and of the pad-up on fatigue crack growth were studied. In this context, the influence of the rolling direction was also investigated, which is important, since longitudinal joints in the aircraft skin are normally performed in rolling direction, and circumferential joints are consecutively performed in transversal direction. Only the upper fuselage section was analyzed in the present work, being the biaxiality ratio therefore 1:1, which includes the pressurization and bending loads.

The specimen geometry included pocketing, with a depth of 1.6 mm, and the welds were performed in a 3.2 mm thick pad-up. The initial notch was placed in the geometric centre of the specimen parallel to the weld, in the transition zone between the heat affected zone and the thermo mechanically affected zone.

The experiments were performed on a triaxial servo-hydraulic testing machine, but only two axes were used. The machine capacity of 1 MN on each cylinder was very high in comparison to the maximum load of 40 kN with a load ratio of 0.1. Nevertheless, the noise could be kept at an acceptable level for the experiments. The PIDL controller allowed maintaining the centre of the specimen in the centre of the machine while applying the required load. The delay (L) synchronized the axes in addition to the standard proportional (P), integral (I) and derivative (D) components of the controller. No phase shift between both axes was introduced and a load corresponding to a nominal stress of 100MPa in the pad-up was applied.

The finite element method was used to optimize the specimen geometry in order to allow using a specimen without slots for load distribution. The specimen arms were designed keeping in mind a uniform stresses in the central area of the specimen.

The specimens were initially slightly distorted due to machining of pockets in a plate with rolling residual stresses and due to the welding process. In the present case the influence of the rolling direction on distortion was higher than the influence of the welding process. Slightly higher distortion was found on specimens welded orthogonally to the rolling direction.

Digital scales in both directions were used for crack tip position determination and a Zeiss optical microscope with CCD camera connected to a computer monitor was used for crack tip detection. Resistive strain gauges were used to verify the strain distribution on the specimen surface. Among others this data provided comparison parameters for a numerical model. Strain was recorded during static loading prior to the fatigue experiment and at each stop for crack length measurement during the fatigue experiment. During clamping, the distorted specimens were forced into a flat shape and the strain gauges were zeroed with the specimen hanging unloaded inside the rig before forcing it to this flat shape. Relatively high surface strains were recorded due to the clamping process. This may be explained by the specimens' initial distortion. This information is useful for reminding the influence of manufacturing induced distortion on in service strains on real engineering structures. The clamped specimen can be seen in Figure 3.4.

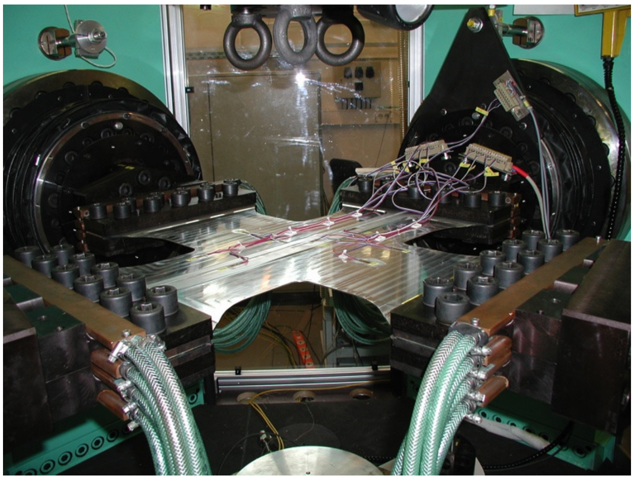

Figure 3.4 Specimen clamped inside the testing rig

The initial notch was 2a = 40 mm and crack initiation only happened after around 10k cycles. On the specimens welded orthogonally to the rolling direction (circumferential joint), the crack growth was faster on one crack tip than on the other. On the other hand, specimens welded parallel to the rolling direction (longitudinal joint) had similar crack growth behaviour on both sides of the initial notch. The average crack growth speed on the specimens welded orthogonally to the rolling direction was higher than on the specimens welded parallel to the crack growth direction On the specimens welded orthogonal to the rolling direction, the crack growth path was not symmetric since the side of the crack entering the welded material was slowed down. On the specimens welded parallel to the welding direction, the crack growth path was symmetric. A comparable result was obtained on duplicate specimens tested. Crack growth behaviour may be expected to be different in the welded material than in the base material. A comparison between the crack growth path in a specimen representing a longitudinal joint and a specimen representing a circumferential joint are shown in Figure 3.5.

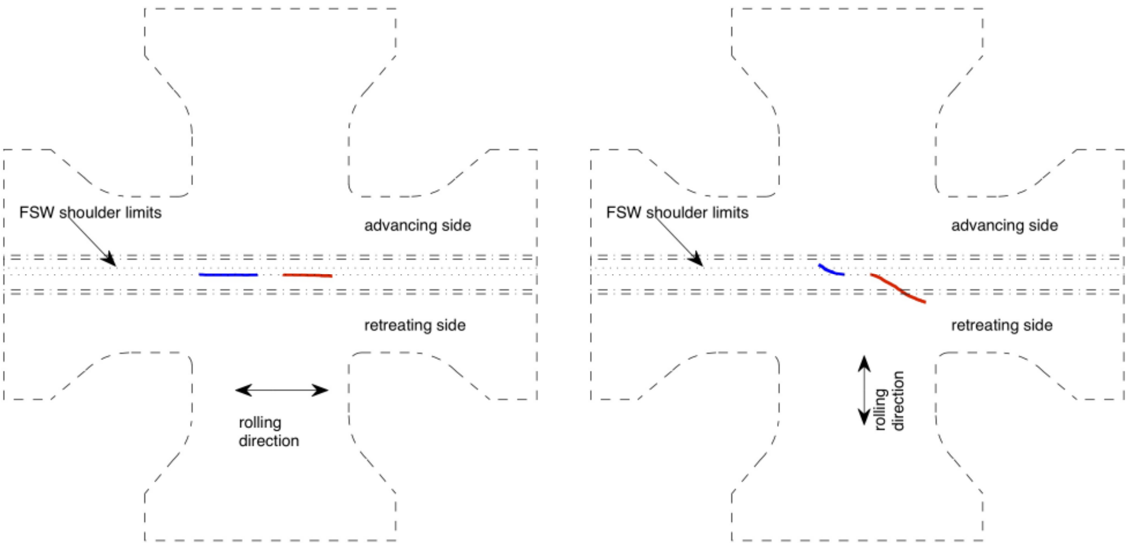

a) longitudinal joint: welded parallel to the rolling direction

b) circumferential joint: welded orthogonally to the rolling direction

Figure 3.5 Crack growth path on two similar specimens, being the only difference the rolling direction

As could be seen, the rolling direction was found to significantly affect the crack growth direction. The rolling residual stresses were found to be partially responsible for specimen distortion after machining. Although to a smaller degree, welding was also found to have an influence on this behaviour. Secondary cracks in the corners between two adjacent loading arms on some of the specimens could not be prevented with the proposed specimen design, but it was possible to control these secondary cracks well enough to prevent an influence on the primary crack growth behaviour.
It was possible to see that the cracks had a high tendency of resisting entering the welded material and that the preferred crack growth direction was the rolling direction. The crack initiation also happened at a later stage than expected based on experience with uniaxial fatigue tests. Furthermore it was learned that the proposed specimen design needs to be optimised in regards to the corner radius between two adjacent loading arms, but was adequate for guaranteeing a mainly uniform stress distribution in the specimen centre.

Acknowledgements:

The authors acknowledge the cooperation of J. Knaack, A. Roos, K.-H. Balzereit and O. Kreienbring. The present work was partially funded by the European Union COINS project, FP6-2005-Aero-1, Contract No. AST5-CT-030825 and the PhD scholarship SFRH / BD / 41061 / 2007 of the Portuguese Foundation for Science and Technology.

3.4 Laser beam welded dissimilar joint of aluminium AA6056 and titanium Ti6Al4V for aeronautical applications

W. V. Vaidya , M. Horstmann, V. Ventzke, B. Petrovski, M. Koçak (HZG), R. Kocik (Astrium-ST), G. Tempus (Airbus)

Dissimilar welds of the aluminium alloy AA6056 and the titanium alloy Ti6Al4V were produced by laser beam welding and their structure-property relationship was investigated on laboratory coupons [1-3]. Such welds combine strength and corrosion resistance of titanium with weight reduction through aluminium, and can be attractive for aerospace applications such as passenger seat track shown in Figure 3.6

This dissimilar weld is, however, a challenge due to differences in physical properties of the base materials such as the melting point, the crystal structure, the thermal conductivity, the density and the modulus of elasticity. Moreover, the formation of the intermetallic phase $TiAl_3$ which being brittle, can be a limiting factor for applications. Hence, the width of $TiAl_3$ at the weld interface must be kept to minimum. This was achieved by a novel technique shown schematically in Figure 3.7. AA6056 sheet was machined at one end to U-slot to intake Ti6Al4V sheet and butt-welded by split laser beam in conductive mode by melting only the Al-alloy U-slot, *without* using a filler wire. The laser beam welding was carried out at BIAS in Bremen. Temperature reached on the Ti-side was less than 1000 °C. Hence, this side remained practically unaffected during welding and retained its initial microstructure: decorating. The Al-side, on the other hand, exhibited the fusion zone and the heat affected zone and its microstructure was affected up to about 23 mm from the weld interface. A very thin layer of $TiAl_3$ with a width of about 1.8±0.3 µm was formed at the weld interface. The coupons investigated had the dimensions, length 300 mm and width 94 mm; the uniform thickness on the Al-side was 2 mm and on the Ti-side 1.8 mm.

The effect of initial microstructure on properties was studied on two temper conditions of AA6056; laser beam welding in T4 (under ageing) followed by tempering to T6 (peak ageing) and laser beam welding in T6 (peak ageing) [1-2]. The post weld tempering improved hardness and strength, whereas welding in T6 exhibited softening in the fusion zone and the heat affected zone. Although $TiAl_3$ was formed at the weld interface, its width was comparable in both cases and the tensile fracture occurred away from the weld interface in a soft zone (within a hardness dip) adjacent to the heat affected zone. The resistance to fatigue crack propagation and fracture was found to be better in the T6-welded specimens than those post weld tempered to T6. When compared to fatigue crack propagation and fracture in the fusion zone and the heat affected zone, the ranking of the weld interface was, however, the lowest in both welding conditions.

Thus, although the weld interface was sound, it did impair properties. As an immediate remedy to reduce the formation of $TiAl_3$ the weld interface was decreased by chamfering Ti6Al4V as shown in Figure 3.8, while keeping the welding conditions unchanged [3]. This seemingly insignificant joint modification refined microstructure and increased hardness and strength slightly.

The most impressive feature was the improved resistance to fatigue crack propagation as shown in Figure 3.8, whereby the fracture mode in the fusion zone of AA6056 adjacent to the weld interface changed from partially intercrystalline to completely transcrystalline. We propose that the changes in volume of Ti6Al4V and AA6056 at the same heat input lead to faster cooling rate in the modified joint. This refines and improves binding (with $TiAl_3$). Moreover, grain size in the fusion zone is reduced, segregation at grain boundaries is suppressed and more solute is retained in the matrix for subsequent hardening during natural or artificial ageing. Thus, means to increase the cooling rate in the fusion zone could indeed be a proper measure to refine microstructure and to improve properties also for similar welds of precipitation hardenable Al-alloys.

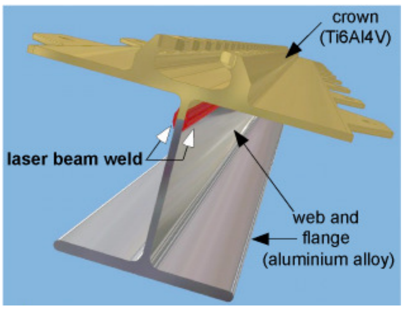

Figure 3.6 Seat track (conceptual design after AIRBUS).

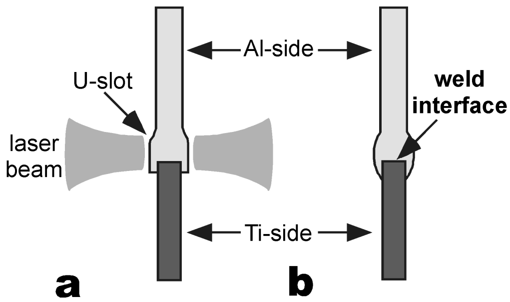

Figure 3.7 Novel technique for laser beam welding (schematics after AIRBUS)

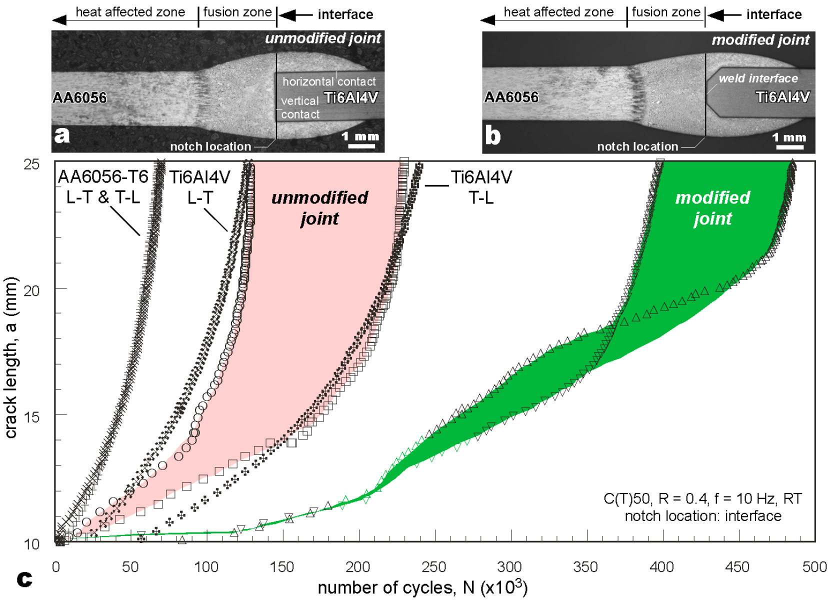

Figure 3.8

The joint configuration (a, b) and the improvement in resistance to fatigue crack propagation at the weld interface through the joint modification (c) for laser beam welding in the T6 condition. Base material data in L-T and T-L orientations are also shown for the reference.

References

[1] Vaidya W. V., Horstmann M., Ventzke V., Petrovski B., Koçak M., Kocik R., Tempus G., Structure-property investigations on a laser beam welded dissimilar joint of aluminium AA6056 and titanium Ti6Al4V for aeronautical applications, Part I: Local gradients in microstructure, hardness and strength, Mater. Sci. Engng. Technol. (Mat.-wiss. u. Werkstofftech.), 40 (2009) 623.

[2] Vaidya W. V., Horstmann M., Ventzke V., Petrovski B., Koçak M., Kocik R., Tempus G., Structure-property investigations on a laser beam welded dissimilar joint of aluminium AA6056 and titanium Ti6Al4V for aeronautical applications, Part II: Resistance to fatigue crack propagation and fracture, Mater. Sci. Engng. Technol. (Mat.-wiss. u. Werkstofftech.), 40 (2009) 769.

[3] Vaidya W. V., Horstmann M., Ventzke V., Petrovski B., Koçak M., Kocik R., Tempus G., Improving interfacial properties of a laser beam welded dissimilar joint of aluminium AA6056 and titanium Ti6Al4V for aeronautical applications, J. Mater. Sci., 45 (2010) 6242.

3.5 Optimization of the crenellation pattern for maximum FCP life improvement

Y.J. Chen, M.V. Uz, N. Huber (HZG)

Thickness variations (crenellations, Figure 3.9) can improve the fatigue crack propagation (FCP) life of integrally stiffened aluminum panels significantly [1]. The source of this improvement is the stress intensity factor (K) modification due to the geometry change caused by the crenellations.

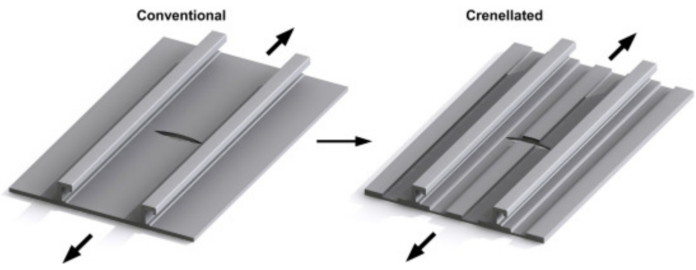

Figure 3.9 Schematic representation of a) conventional and b) crenellated panel with one stringer bay crack under tensile loading. The weights of the panels are equal.

The crenellation pattern controls the *K*-distribution as function of crack length (*a*) and therefore indirectly the extent of the FCP life improvement that can be achieved.
The limits of this improvement were investigated by optimizing the crenellation pattern with a numerical methodology, which couples finite element analysis and artificial neural networks techniques [2]. During the optimization, only the non-linear relationship between ΔK and FCP rate, which is one of the two mechanisms contributing to the fatigue life extension by crenellations (for details see [1]) was considered. The loading history effects were not taken into account for ease.
A Python code was written to create 1180 random crenellation patterns by changing characteristic dimensions (Figure 3.10 a). For each pattern, the *K* factors and the corresponding FCP lifetime were calculated based on the Paris law. The analysis results are presented in Figure 3.10-b. Here the X and Y axes present certain dimensions in the crenellation geometry (given in Figure 3.10 a) and the Z axis (ξ) shows the FCP life of the crenellated panel normalized by that of conventional panel having equal weight.

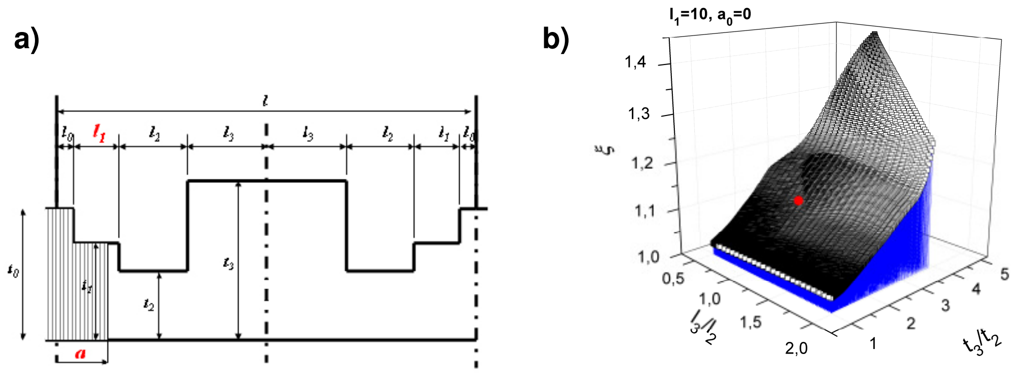

Figure 3.10 a) geometry parameters of the crenellation pattern b) normalized FCP life of the crenellated panel as a function of the geometry parameters given in a)

The figure reveals that the FCP life ratio of crenellated and reference panels is always larger than 1. In other words, independent of the chosen parameters l_1, l_3/l_2 and t_3/t_2, the crenellations always improve the FCP life. The red point on the Figure 3.10-b corresponds to the formerly tested pattern and as can be seen the Paris law predicts only about 10% longer FCP life for this geometry compared to the conventional reference panel. However, there is enough room up to 45% improvement when an optimal crenellation pattern is chosen. At this point it should be noted again that this improvement is based only on one of the two mechanisms operating together on a crenellated panel. The test result of the panel with “non-optimized” crenellation pattern demonstrated 65% FCP life improvement under constant amplitude loading and even 150% under spectrum loading conditions [1]. This study was performed to increase this improvement further [2]. The experimental part of the study is currently running.

References

[1] M. V. Uz, M. Koçak, F. Lemaitre, J.-C. Ehrstöm, S. Kempa, F. Bron, Int. J. of Fatigue 31, pp. 916-926, 2009

[2] M. V. Uz, Y. J. Chen, N. Huber, Proc. of ICAF 2011, Montreal, Canada (also will be presented orally)

3.6 Numerical analyses of bonded structural members for aircraft structures with improved damage tolerance

S. Khan, J. Mosler (HZG)

Adhesive bonding can provide solutions for cost effective and low weight aircraft fuselage structures – in particular, if damage tolerance (DT) is the critical design criterion. By combining selective reinforcements, bonded structures can guarantee slow crack propagation and even crack arrest resulting eventually in a long lifetime of the respective structural member.
One structural member in aircrafts for which the aforementioned solution strategy seems to be very promising is the stringer-skin connection. Here, material failure can be strongly influenced by means of low-cycle-fatigue (LCF), cf. [1]. This is due to the high tensile stresses observed in the stringer. Such stresses have been reported as close to the Ultimate Tensile Strength (UTS) of the stringer material. As a consequence, only a relatively small number of loading cycles is necessary for making the stringer fail.
For avoiding material failure or more precisely, for estimating the lifetime of structural members such as the stringer-skin connection, suitable design criteria are needed. Most frequently, purely empirical or heuristic criteria have been considered for that purpose. Although they have been successfully applied to the modelling of fatigue-induced failure – also for comparably complex structures – they are not sufficient for understanding the complex failure process associated with the stringer-skin connection. For that reason, more detailed finite element analyses based on a novel constitutive model have been conducted.
The novel constitutive model used within the aforementioned finite element analyses captures most of the relevant damage processes observed within the high-strength aluminium alloy Al2024-T351. In particular, it accounts for the complex interaction between ductile damage accumulation caused by void growth and quasi-brittle material degradation related to fatigue crack propagation. This model is a result of research activities in different areas ranging from experiments and characterization to the numerical implementation. While the model characterizing the ductile damage mechanism is similar to a rather standard and already well established model proposed by Lemaitre (see [2]), a new approach has been developed for describing brittle damage, cf. [3].
The stringer-skin connection has been analyzed numerically by embedding the novel damage model within a finite element code. The structure has been loaded displacement-controlled with the same loading magnitudes in tension and compression. For smearing the stress singularities, the crack front has been approximated by an elliptical crack front (see Figure 3.11, lower left hand side). The results of the simulation are summarized in Figure 3.11. According to Figure 3.11, the plastic stored energy is highly localized in the vicinity of the crack tip. Since crack initiation is assumed within the model, if the plastic stored energy reaches a certain threshold value, a fatigue crack is finally observed. This crack will eventually form a macroscopic crack

defining the lifetime of the structure. As a consequence, the proposed constitutive model allows predicting the lifetime of complex engineering structures.
Based on the novel constitutive model, the lifetime of different stringer-skin connections can be effectively analyzed by reducing the number of time-consuming and expensive experiments. As a result, this virtual testing facility can be used for efficiently developing novel and innovative structural members for aircrafts with an improved damage tolerance resulting in a longer lifetime.

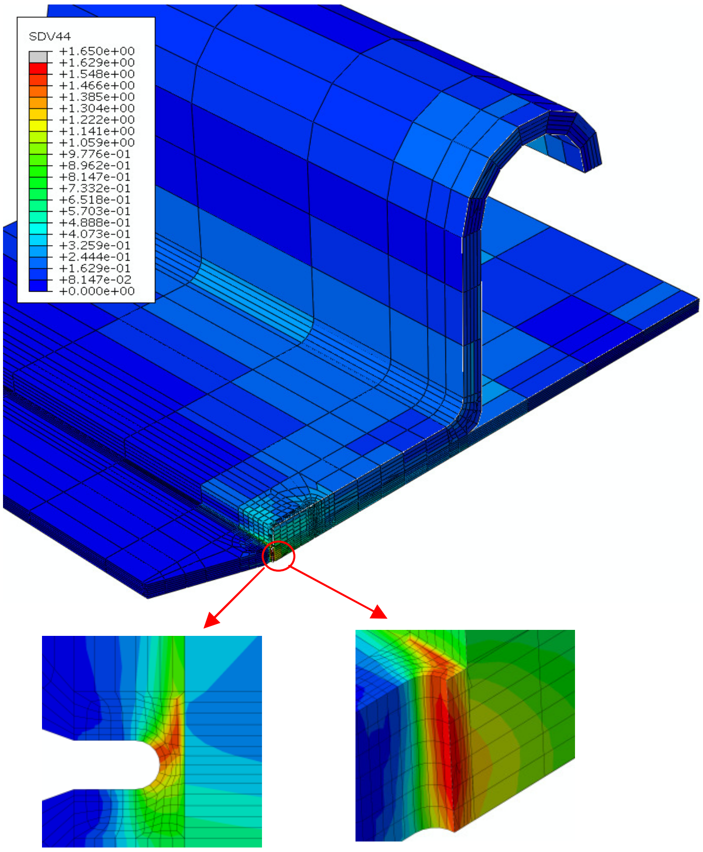

Figure 3.11 Evolution of the stored plastic energy driving damage initiation. Lower left hand side assumed elliptical crack front (top view), lower right hand side the profile of plastic stored energy (side view).

References

[1] Meneghin I. Damage tolerance assessment of stiffened panels. University of Bologna, Technical report 2010.

[2] Lemaitre J, editor A course on damage mechanics. Berlin, Heidelberg, New York: Springer-Verlag, 1992.

[3] Kintzel O, Khan S, Mosler J. A novel isotropic quasi-brittle damage model applied to LCF analyses of Al2024. International Journal of Fatigue 2010;32:1948.

3.7 Friction Stir Welded Aircraft Structures - Window frame

D. Knerr, B. Zapf (RUAG)

The aim of the German LuFo IV research project „ASSYMET" (**Ass**embly **met**allische Rumpfstruktur) as a part of the joint research project "KOMET" (**Ko**steneffiziente **met**allische Rumpfstruktur) is to optimize the manufacturing and the assembly of metallic fuselages to save weight, manufacturing costs and assembly time. Within one of the work packages RUAG Aerospace Structures GmbH tries to improve the join technology and the assembly technology by applying more automated processes. At first, a new method to attach window frames to the skin is tested. Instead of riveting the window frame, it is welded into the skin using friction stir welding (FSW). The welding is performed using a 6-axis industrial robot, so it is possible to realize the three dimensional shape of the welding seam. Because of the high process forces of FSW, the biggest problems are the residual stresses and the distortion of the material. During the welding process, the distortion is watched via the measuring system ARAMIS®. With this test set-up it is possible to optimize the welding sequence, the welding parameters and the FSW-tool to get as little distortion as possible.
There are several ways to integrate the welded window into the side shell. In a first step, the window frame is welded into a double sheet and this is bonded or riveted into the skin. The next step forward is welding the window frame straight into the skin. Thereby it can be possible to modify the design of the window frame into an optimized welding geometry. It is expected, that the wide boundary that is needed for the rivets could be designed smaller. This reduces the weight of the window frame and the costs for the forging.

Figure 3.12 Kuka Robot, FSW tool, airframe (source: RUAG, EADS, KUKA)

Next aim is to develop a tooling and an automated clamping system for the serial production. The clamping has to be very tight, to ensure a robust process in spite of the immense forces during FSW.
The achievements of the new window frame design are a lower weight and a faster mounting.

The research project ASSYMET as a part of the joint research project KOMET has received funding from the German Federal Ministry of Economics and Technology's LuFo-Project IV Call 2 under grant agreement no. 20W0807C.

4 Fatigue Life Assessment and Prediction

4.1 Bulging correction factors for cracks growing in longitudinal direction between and under intact and broken frames

W.D.T. Spanjer (Tata Steel), M. Miermeister (Aleris)

For a pressurized fuselage the dominant loading condition is the Ground-Air-Ground (GAG) cycle. During this load cycle the pressurization of the fuselage will create stresses in both longitudinal and circumferential direction. For cracks growing in longitudinal direction, between intact frames or under a broken or intact frame, not only the so-called hoop stress is relevant, but also the bulging of the crack due to internal pressurization. The bulging factor is an additional boundary correction to obtain an analytical stress intensity factor at the crack-tip. Several authors have investigated the bulging behavior of cracks in pressurized vessels, with or without reinforcements. Commonly used methods are described by Swift, Chen and others. However, it was found that these analytical methods provide only accurate solutions for cracks not in close proximity of the frames, e.g. only for small cracks. Stress intensity factor calculations using finite element methodology has proven to be very accurate and is therefore an appropriate tool to investigate the influence of the reinforcements etc. on the bulging behaviour.

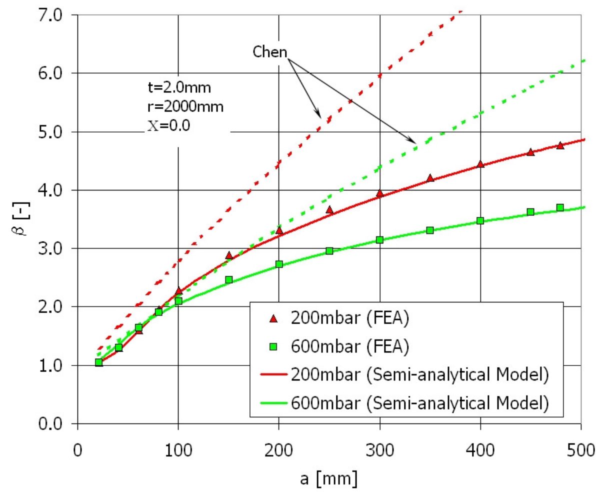

Figure 4.1 Normalized Stress Intensity Factor as a function of the (half) crack length

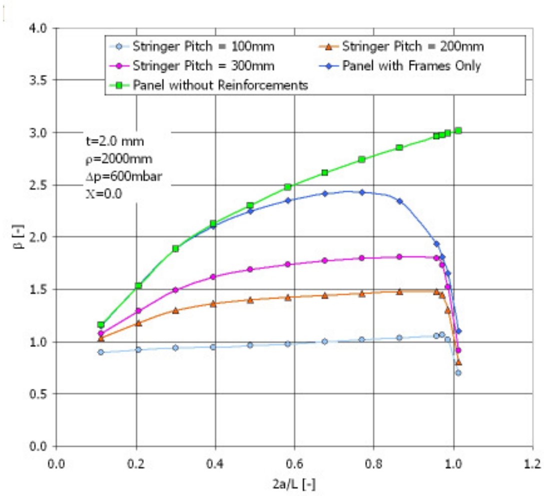

Figure 4.2 The influence of the stringer pitch on (normalized) stress intensity factor for a crack between two frames (frame pitch L)

The first step in the investigation was to look at a cylindrical pressurized shell; a comparison is made between the analytical solutions and finite element solutions. The finite element model consists of shell elements with a longitudinal crack and loading is introduced by internal pressurization. The commonly used Chen equation gives good results for small crack lengths and low pressurization values, which is also confirmed by FEA. For larger cracks and higher internal pressures, Chen's equation is not valid anymore and the analytical model deviate strongly from the finite element results (symbols in Figure 4.1). Based on the basic form of Chen's semi-analytical solution a new solution has been found that encloses also larger cracks and higher pressure loads (Figure 4.1, solid curves).
The next step was to look at the influence of the reinforcements on the bulging behaviour. The finite element model was therefore extended with frames and stringers. One of the major con-

clusions is that the influence of the stringers on the bulging can not be neglected (Figure 4.2), contrary to the assumptions made in previous work of others. The parametrical set-up of the finite element model gives the opportunity to look at the influence of various parameters. Besides the crack length and the pressure load, parameters like the panel curvature and thickness, the biaxiality and the stringer and frame pitch can be varied. In addition to the already mentioned semi-analytical solution for un-stiffened cylindrical shells, correction terms have been developed that accounts for the influence of the reinforcements. These equations will be implemented in the Tata Steel-Aleris Fatigue Crack Growth Tool.

4.2 Prediction of fatigue crack propagation rates in compressive residual stress fields

D. Schnubel, M. Horstmann, N. Huber (HZG)

Residual stresses induced in integral metallic structures by welding or other manufacturing processes can have a significant impact on the observed fatigue crack propagation [1].
To gain predictions of the fatigue crack propagation taking into account the effect of residual stresses, commonly the residual stress is characterized experimentally and the results are then used in combination with the weight functions or the finite element method to extract the stress intensity variation due to the residual stresses K_{res}. Implying pure linear behavior, then the superposition principle given with $K_{tot} = K_{res} + K_{appl}$, is used to calculate the total acting stress intensity factors K_{tot} due to combined external load and residual stresses [2] and use them in empirical crack growth laws to predict the resulting fatigue crack propagation rates.
Even though, this general approach is well accepted, there are two issues that need to be addresses to gain general predictions also large structures and cracks growing though areas of compressive residual stresses. Firstly, residual stress measurements are costly and difficult to perform for large complex structures, while delivering only information for a limited number of stress components and measurement points. Secondly, when dealing with the scenario of a fatigue crack growing in a compressive residual stress field at a small applied load ration R_{tot}, it becomes necessary to introduce corrections to prevent a physically not reasonable overlapping of the crack faces behind the crack tip in the prediction models [2]. Doing so directly implies that the superposition rule is not valid any more, for this case $K_{tot} \neq K_{res} + K_{appl}$, hence the extraction of K_{tot} needs to be done from a model being subjected to both the residual stresses and the externally applied load in the same time.
Addressing these two issues we propose the following approach [3]:

- Usage of transient numerical process simulation to predict the production induced residual stress field of the full structure [4]. This way reasonable residual stress predictions can be generated also for large complex structures.
- Extraction of the total stress intensities K_{tot} due to combined external load and residual stresses in a mechanical restart finite element simulation on the process simulation results by subsequent cutting of the model and the introduction of a contact condition on the crack faces.
- Prediction of the fatigue crack propagation rate da/dN using the extracted K_{tot} in suitable empirical crack growth law, e.g. the Walker equation.

The capabilities of the proposed course of actions are demonstrated in the following on the case of a fatigue crack growing in an AA2198 C(T)100 specimens containing one line of local laser heating as shown in Figure 4.3 (a). For the experimental validation of the prediction results base material specimens and specimens subjected to laser heating were tested with a sinusoidal variation of the externally applied load between 0.41 kN and 4.10 kN.

Figure 4.3 (b) shows the prediction results for both base material specimens without and laser heated specimens with residual stresses. The upper graph of Figure 4.3 (b) shows the numerically predicted variation of the longitudinal residual stress induced by the local heating and the middle graph shows the resulting impact on the calculated total stress intensities K_{tot} in comparison to the base material specimen that was assumed to be stress free. The resulting prediction of the fatigue crack propagation rates using the Walker equation with AA2024 material parameters are shown in the lower graph together with the experimental results. As seen a good agreement can be found.
It should be pointed out that for the given configuration the crack starts growing in an area of compressive residual stresses, extending towards the area of high tensile stresses. The developed modeling approach is capable of predicting the actual change in crack growth rates for this case reasonably.
The presented results also highlight the basic fact, that compressive residual stresses retard the fatigue crack propagation. The proposed prediction methodology shall be used in the future together with optimization methods, to examine the possibility of fatigue crack growth retardation in integral metallic structures via the well-directed introduction of residual stresses.

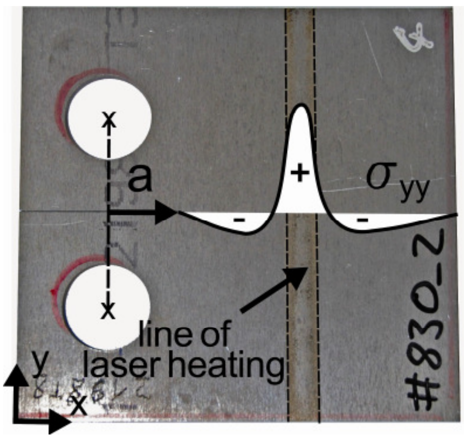

(a)

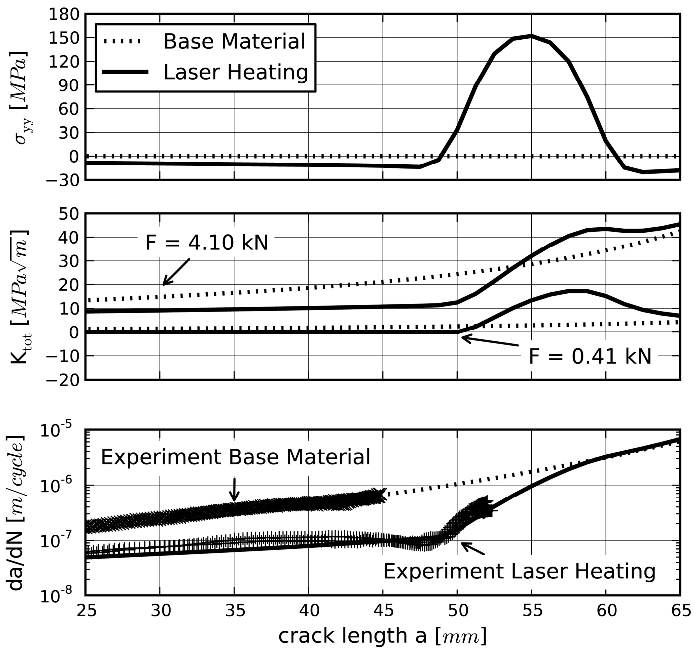

(b)

Figure 4.3 **(a)** **C(T)100 specimen containing a line of laser heating and**
(b) **Comparison of the numerically predicted and measured FCP rates**

References

[1] Irving P, Ma Y E, Zhang X, Servetti G, Williams S, Moore, G, dos Santos J and Pacchione M. Control of crack growth rates and crack trajectories for enhanced fail safety and damage tolerance in welded structures. Proceedings of the 25th ICAF Symposium of the International Committee on Aeronautical Fatigue; 2009, p. 387-405.

[2] Parker A. Stress Intensity Factors, Crack Profiles and Fatigue Crack Growth Rates in Residual Stress Fields. In: Throop JF, Reemsnyder HS, editors. Residual Stress Effects in Fatigue; vol. ASTM STP 776. ASTM;1982, p. 13:31.

[3] Schnubel D, Horstmann M, Huber N. Prediction of fatigue crack propagation rates in metallic structures containing residual stresses. Poster session of the 26th ICAF Symposium of the international Committee on Aeronautical Fatigue, 2011.

[4] Radaj D. Welding residual stresses and distortion: Calculation and measurement. DVS Verlag; 2003.

4.3 Variable amplitude load-interaction and its consequences on fatigue crack growth

S. Daneshpour, D. Schnubel, T. Fischer, P. Staron, N. Huber (HZG)

Aircraft structures operate under spectrum loading (variable amplitude cyclic loading) where load history effects occur. The occurrence of an overload (high-low load sequence) has a strong effect on the crack propagation behaviour; tensile overloads lead to favourable crack retardation or even crack arrest [1]. The reliability of fatigue life prediction methods depends mainly on their ability to account for the mechanisms of damage taking place during cyclic loading. Improvements in the accuracy of life prediction methods can be made by taking into account the effect of load interactions that are always occurring in a load spectrum during the fatigue life prediction of aircraft structures and components.

Currently, a research project on crack retardation due to overloads is being conducted in Helmholtz-Zentrum Geesthacht, which is aimed at predicting crack growth rates for post-overload cracks and finally developing a reliable fatigue life prediction based on the combined damage and fracture mechanics approaches. Finite Element (FE) simulations in conjunction with experimental tools, such as crack tip stress/strain measurements by high-energy X-ray diffraction at the synchrotron sources at DESY are being used to quantify the formation and evolution of damage due to application of the overloads occurred during cyclic loading.

The effects of an overload on the significance of internal stresses and on formation of compressive residual stresses ahead of the crack tip can be illustrated by utilising high-energy X-ray diffraction [2]. As an example, in-situ diffraction measurements were performed on the loaded Compact-Tension specimens of A6056-T6 aluminium alloy [3].

Figure 4.4 shows a comparison between the measured and simulated internal stress field $\sigma_y - \sigma_x$ for an applied overload with magnitude of 10.2 kN.

The dots in Figure 4.4 indicate the measurement positions along the crack path. The simulation results were extracted in a similar way from the fine meshed region shown in Figure 4.4a, upper half. In general, a good agreement between simulation and experimental results is observed, especially for the areas a bit further away from the crack tip.

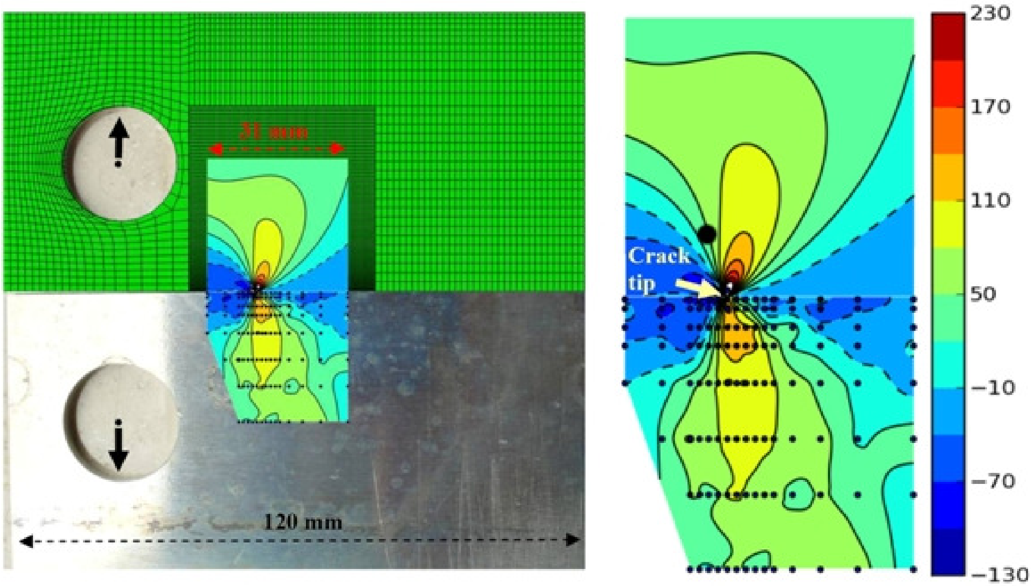

a.) b.)

Figure 4.4 Stress field results $\sigma_y - \sigma_x$ (in MPa) close to the crack tip at an overload of 10.2 kN taken from simulation (top part) and diffraction measurements (bottom part):
a) overview, b) area close to the crack tip

The valuable experimental results can be used for determining the material parameters needed for calibration of the damage model. The FE model coupled to the damage model is being developed for assessing the amount of crack retardation and for predicting the shape of crack front observed after applying overloads [4, 5].

References

[1] S. Daneshpour, M. Koçak, S. Langlade, M. Horstmann: ‘Effect of overload on fatigue crack retardation of aerospace Al-alloy laser welds using crack-tip plasticity analysis’, Int. J. Fatigue, 31, 2009, pp.1603–1612

[2] D. Schnubel, S. Daneshpour, P. Staron, T. Fischer, N. Huber: ‘Residual stress measurements on cracked Al specimens under structural loading in the stress rig’, Hasylab Annual User Experiment Report, http://hasylab.desy.de/annual_report/ , 2009.

[3] P. Staron, et al.: ‘In Situ Experiments with Synchrotron High-Energy X-Rays and Neutrons’, Advanced Engineering Materials, DOI: 10.1002/adem.201000297, 2010.

[4] S. Daneshpour, J. Dyck, V. Ventzke, N. Huber:’Crack retardation mechanism due to overload in base material and laser welds of Al alloys’, Int. J. Fatigue, 2011 (under review).

[5] N. Huber, S. Daneshpour, O. Kintzel, S. Khan, J. Mosler: ’Modeling of Damage Evolution in Metallic Aerospace Structures‘, accepted for inclusion in the poster session in ICAF 2011.

4.4 Least Biquadratic Method in Fundamental Sciences of Estimation, Approximation, and Data Processing

L. G. Gelimson (IFS)

The least square method (LSM) [1] by Legendre and Gauss only usually applies to solving contradictory (e.g. overdetermined) problems, which is always the case in data processing. Overmathematics [2, 3] has discovered a lot of principal shortcomings [4] of this method. Additionally, by more than 4 data points, the second power can paradoxically give smaller errors of better approximations and can be increased due to the least biquadratic method (LBQM) in fundamental sciences of estimation, approximation, and data processing [5-7].

Given n ($n \in N^+ = \{1, 2, ...\}$, $n > 2$) points $[_{j=1}^{n} (x'_j , y'_j)]$ with any real coordinates.

Use centralization transformation $x = x' - \Sigma_{j=1}^{n} x'_j / n$, $y = y' - \Sigma_{j=1}^{n} y'_j / n$. Fit points $[_{j=1}^{n} (x_j , y_j)]$ with a straight line $y = ax$ to minimize the sum of the 4th powers of the ordinate differences between this line and everyone of the n data points $[_{j=1}^{n} (x_j , y_j)]$:
${}^4S(a) = \Sigma_{j=1}^{n} (ax_j - y_j)^4$, $\Sigma_{j=1}^{n} x_j^4 a^3 - 3\Sigma_{j=1}^{n} x_j^3 y_j a^2 + 3\Sigma_{j=1}^{n} x_j^2 y_j^2 a - \Sigma_{j=1}^{n} x_j y_j^3 = 0$.

Introduce $a' = a - \Sigma_{j=1}^{n} x_j^3 y_j / \Sigma_{j=1}^{n} x_j^4$ to reduce cubic equation [1] $a'^3 + pa' + q = 0$ with

$p = 3[\Sigma_{j=1}^{n} x_j^2 y_j^2 / \Sigma_{j=1}^{n} x_j^4 - (\Sigma_{j=1}^{n} x_j^3 y_j)^2/(\Sigma_{j=1}^{n} x_j^4)^2]$,
$q = - \Sigma_{j=1}^{n} x_j y_j^3 / \Sigma_{j=1}^{n} x_j^4 + 3\Sigma_{j=1}^{n} x_j^2 y_j^2 \Sigma_{j=1}^{n} x_j^3 y_j /(\Sigma_{j=1}^{n} x_j^4)^2 - 2(\Sigma_{j=1}^{n} x_j^3 y_j)^3/(\Sigma_{j=1}^{n} x_j^4)^3$,
$Q = (p/3)^3 + (q/2)^2$, $A = (- q/2 + Q^{1/2})^{1/3}$, $B = (- q/2 - Q^{1/2})^{1/3}$,
$a'_1 = A + B$, $a'_{2,3} = - (A + B)/2 \pm 3^{1/2}/2\ i\ (A - B)$ where $i^2 = -1$.

Increasing the power improves the LSM results via the LBQM, especially by not too great data scatter. In numeric tests [Figure 4.5, Figure 4.6 with replacing (x', y') via (x , y)], the LSM gives y = 0.909x + 2.364 and even y = 0.591x + 3.636, whereas the LBQM brings y = 0.968x + 2.127 and y = 0.698x + 3.206. Data symmetry straight line y = x + 2 is the best linear approximation given, e.g., by least squared distance theories.

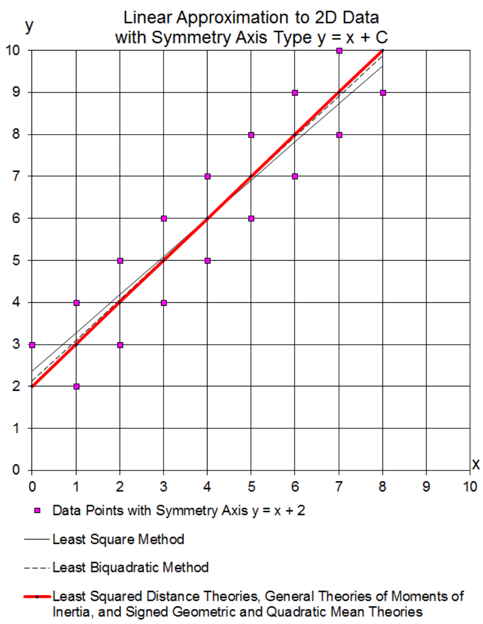

Figure 4.5

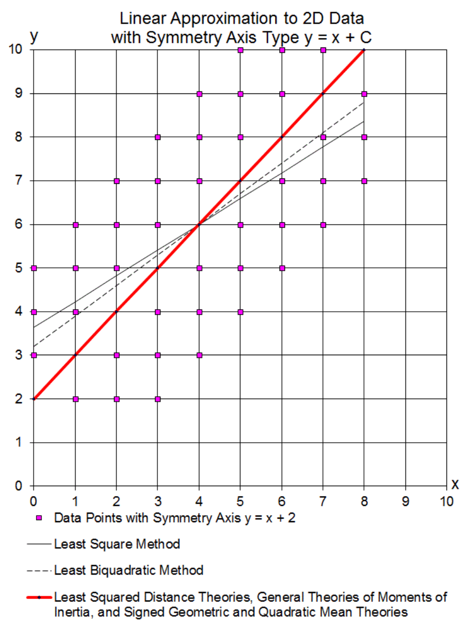

Figure 4.6

The LBQM is invariant, very efficient, and applicable to aeronautical fatigue etc.

Acknowledgements

to Anatolij Gelimson for our constructive discussions on coordinate system transformation invariances and his very useful remarks.

References

[1] Encyclopaedia of Mathematics. Ed. M. Hazewinkel. Volumes 1 to 10. Kluwer Academic Publ., Dordrecht, 1988-1994
[2] Gelimson L. G. Providing Helicopter Fatigue Strength: Flight Conditions. In: Structural Integrity of Advanced Aircraft and Life Extension for Current Fleets – Lessons Learned in 50 Years After the Comet Accidents, Proceedings of the 23rd ICAF Symposium, Dalle Donne, C. (Ed.), 2005, Hamburg, Vol. II, 405-416
[3] Gelimson L. G. Overmathematics: Fundamental Principles, Theories, Methods, and Laws of Science. The "Collegium" All World Academy of Sciences Publishers, Munich, 2010
[4] Gelimson L. G. Corrections and Generalizations of the Least Square Method. In: Review of Aeronautical Fatigue Investigations in Germany during the Period May 2007 to April 2009, Ed. Dr. Claudio Dalle Donne, Pascal Vermeer, CTO/IW/MS-2009-076 Technical Report, International Committee on Aeronautical Fatigue, ICAF 2009, EADS Innovation Works Germany, 2009, 59-60
[5] Gelimson L. G. General estimation theory. Transactions of the Ukraine Glass Institute, 1 (1994), 214-221. The same with its translation into Japanese. The "Collegium" All World Academy of Sciences Publishers, Munich, 2001
[6] Gelimson L. G. General Estimation Theory. The "Collegium" All-World Academy of Sciences Publishers, Munich (Germany), 2004. The same with its translation into Japanese. The "Collegium" All World Academy of Sciences Publishers, Munich, 2010
[7] Gelimson L. G. Fundamental Sciences of Estimation, Approximation, and Data Processing. The "Collegium" All World Academy of Sciences Publishers, Munich, 2010

4.5 Least Squared Distance Theories in Fundamental Sciences of Estimation, Approximation, Data Modeling and Processing

L. G. Gelimson (IFS)

The least square method (LSM) [1] by Legendre and Gauss only usually applies to contradictory (e.g. overdetermined) problems, in particular, by methods of finite elements, points, etc. Overmathematics [2, 3] and fundamental sciences of estimation, approximation, and data processing [4] have discovered a lot of principal shortcomings [5] of the LSM. Its errors increase with data scatter and approximation declination due to regarding data deviations from, e.g., the x-axis. Least squared distance theories (LSDT) consider data deviations namely from approximation graph.

In the simplest 2D linear case, given n ($n \in N^+ = \{1, 2, ...\}$, $n > 2$) points $[_{j=1}^{n} (x'_j , y'_j)] = \{(x'_1 , y'_1),$

$(x'_2 , y'_2), ... , (x'_n , y'_n)]$ with any real coordinates. Use centralization transformation $x = x' - \Sigma_{j=1}^{n} x'_j / n$, $y = y' - \Sigma_{j=1}^{n} y'_j / n$. Fit points $[_{j=1}^{n} (x_j , y_j)]$ with straight line $ax + by = 0$ containing origin

O(0, 0). The distance between this line and the jth data point (x_j , y_j) and the sum of such squared distances to be minimized are

$$d_j = |ax_j + by_j|/(a^2 + b^2)^{1/2},\quad {}^2S(a , b) = \Sigma_{j=1}^n d_j^2 = \Sigma_{j=1}^n (ax_j + by_j)^2/(a^2 + b^2).$$

If $b \neq 0$, $\Sigma_{j=1}^n x_jy_j \neq 0$, denote $A = -a/b$. The quadratic equation has two real solutions:

$$\Sigma_{j=1}^n x_jy_j A^2 - (\Sigma_{j=1}^n y_j^2 - \Sigma_{j=1}^n x_j^2)A - \Sigma_{j=1}^n x_jy_j = 0,$$
$$A_{1,2} = \{\Sigma_{j=1}^n y_j^2 - \Sigma_{j=1}^n x_j^2 \pm [(\Sigma_{j=1}^n y_j^2 - \Sigma_{j=1}^n x_j^2)^2 + 4(\Sigma_{j=1}^n x_jy_j)^2]^{1/2}\}/(2\Sigma_{j=1}^n x_jy_j),$$
$${}^2S''_{AA} = 2/(A^2 + 1)^3 [- 2\Sigma_{j=1}^n x_jy_j A^3 + 3(\Sigma_{j=1}^n y_j^2 - \Sigma_{j=1}^n x_j^2)A^2 +$$
$$6\Sigma_{j=1}^n x_jy_j A + \Sigma_{j=1}^n x_j^2 - \Sigma_{j=1}^n y_j^2] > 0 \text{ (sufficient for that minimum).}$$

Define and determine measures $S_L = [{}^2S_{min}(A) / {}^2S_{max}(A)]^{1/2}$ of data scatter and $T_L = 1 - S_L = 1 - [{}^2S_{min}(A) / {}^2S_{max}(A)]^{1/2}$ of data trend with respect to linear approximation. Also by nonlinearity, $S \leq S_L$. Unlike the LSM, LSDT provide best linear approximation to the given data, e.g. in numeric tests, Figure 4.7 - Figure 4.8 with replacing (x', y') via (x , y):

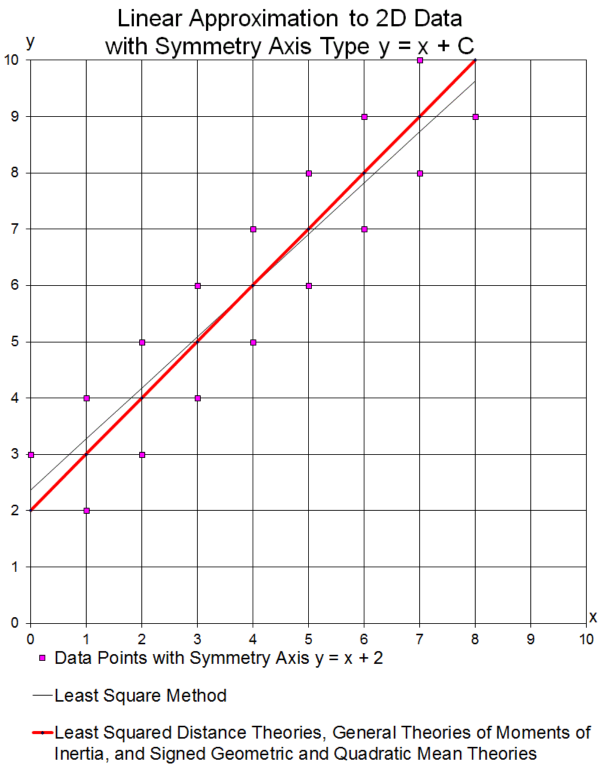

Figure 4.7 S_L = 0.218. T_L = 0.782

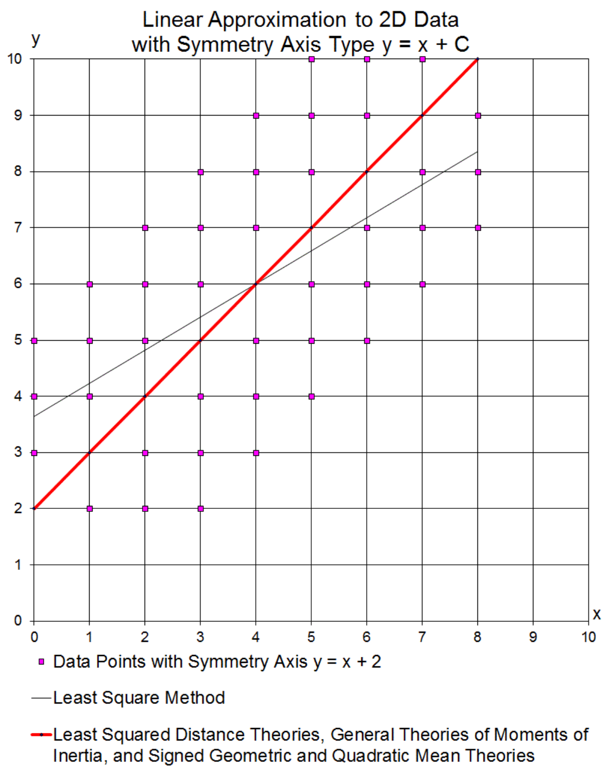

Figure 4.8 S_L = 0.507. T_L = 0.493

Nota bene: By linear approximation, the results of LSDT and general theories of moments of inertia [4] coincide. By data symmetry axis (and the best linear approximation) $y = \pm x + C$, the same also holds for signed geometric and quadratic mean theories [4]. Here $y = x + 2$. The LSM gives the same data center and underestimates the modulus of the declination to the x-axis (which is typical) due to considering data deviations from this x-axis instead of the approximation straight line.

LSDT are very efficient in data estimation, approximation, and processing by rotation invariance and reliable even by great data scatter, e.g. in aeronautical fatigue.

References

[1] Encyclopaedia of Mathematics. Ed. M. Hazewinkel. Volumes 1 to 10. Kluwer Academic Publ., Dordrecht, 1988-1994

[2] Gelimson L. G. Providing Helicopter Fatigue Strength: Flight Conditions. In: Structural Integrity of Advanced Aircraft and Life Extension for Current Fleets – Lessons Learned in 50 Years After the Comet Accidents, Proceedings of the 23rd ICAF Symposium, Dalle Donne, C. (Ed.), 2005, Hamburg, Vol. II, 405-416

[3] Gelimson L. G. Overmathematics: Fundamental Principles, Theories, Methods, and Laws of Science. The "Collegium" All World Academy of Sciences Publishers, Munich, 2010

[4] Gelimson L. G. Fundamental Sciences of Estimation, Approximation, and Data Processing. The "Collegium" All World Academy of Sciences Publishers, Munich, 2010

[5] Gelimson L. G. Corrections and Generalizations of the Least Square Method. In: Review of Aeronautical Fatigue Investigations in Germany during the Period May 2007 to April 2009, Ed. Dr. Claudio Dalle Donne, Pascal Vermeer, CTO/IW/MS-2009-076 Technical Report, International Committee on Aeronautical Fatigue, ICAF 2009, EADS Innovation Works Germany, 2009, 59-60

4.6 Least Squared Distance Theory in Fundamental Science of Solving General Problems

L. G. Gelimson (IFS)

The least square method (LSM) [1] by Legendre and Gauss only usually applies to contradictory (e.g. overdetermined) problems, by methods of finite elements, points, etc. Overmathematics [2-4] and fundamental science of solving general problems [5] have discovered many principal shortcomings [2-6] of this method.
In fundamental science of solving general problems, least squared distance theory (LSDT) is valid by coordinate system rotation invariance.

Given a finite overdetermined set of n ($n > m$; $m , n \in N^+ = \{1, 2, ...\}$) linear equations

$\Sigma_{k=1}^m a_{kj}x_k = c_j$ ($j = 1, 2, ... , n$; $k = 1, 2, ... , m$) (1)

with m unknowns x_k and any given real numbers a_{kj} and c_j. The distance between the jth m-1-dimensional "plane" (1) and any point $[_{k=1}^m x_k] = (x_1 , x_2 , ... , x_m)$, as well as the sum of the squared distances between this point and each of the n "planes", are

$d_j = |\Sigma_{k=1}^m a_{kj}x_k - c_j|/(\Sigma_{k=1}^m a_{kj}^2)^{1/2}$, ${}^2S = \Sigma_{j=1}^n d_j^2 = \Sigma_{j=1}^n (\Sigma_{k=1}^m a_{kj}x_k - c_j)^2/\Sigma_{k=1}^m a_{kj}^2$.

${}^2S$ minimization gives the determined set of m equations with m unknowns x_k :

$\Sigma_{k=1}^m [\Sigma_{j=1}^n a_{ij}a_{kj} /\Sigma_{k=1}^m a_{kj}^2]\, x_k = \Sigma_{j=1}^n a_{ij}c_j / \Sigma_{k=1}^m a_{kj}^2$ ($i = 1, 2, ... , m$).

By $m = 2$, replacing x_1 with x , x_2 with y , a_{1j} with a_j , and a_{2j} with b_j , we finally obtain:

$d_j = |a_jx + b_jy - c_j|/(a_j^2 + b_j^2)^{1/2}$, ${}^2S = \Sigma_{j=1}^n d_j^2 = \Sigma_{j=1}^n (a_jx + b_jy - c_j)^2/(a_j^2 + b_j^2)$;
$\Sigma_{j=1}^n a_j^2/(a_j^2 + b_j^2)\, x + \Sigma_{j=1}^n a_jb_j /(a_j^2 + b_j^2)\, y = \Sigma_{j=1}^n a_jc_j /(a_j^2 + b_j^2)$,
$\Sigma_{j=1}^n a_jb_j /(a_j^2 + b_j^2)\, x + \Sigma_{j=1}^n b_j^2/(a_j^2 + b_j^2)\, y = \Sigma_{j=1}^n b_jc_j /(a_j^2 + b_j^2)$;
$x = [\Sigma_{j=1}^n a_jc_j /(a_j^2 + b_j^2)\, \Sigma_{j=1}^n b_j^2/(a_j^2 + b_j^2) - \Sigma_{j=1}^n a_jb_j /(a_j^2 + b_j^2)\, \Sigma_{j=1}^n b_jc_j /(a_j^2 + b_j^2)]/$
$\{\Sigma_{j=1}^n a_j^2/(a_j^2 + b_j^2)\, \Sigma_{j=1}^n b_j^2/(a_j^2 + b_j^2) - [\Sigma_{j=1}^n a_jb_j/(a_j^2 + b_j^2)]^2\}$,
$y = [\Sigma_{j=1}^n a_j^2/(a_j^2 + b_j^2)\, \Sigma_{j=1}^n b_jc_j/(a_j^2 + b_j^2) - \Sigma_{j=1}^n a_jb_j/(a_j^2 + b_j^2)\, \Sigma_{j=1}^n a_jc_j/(a_j^2 + b_j^2)]/$

$\{\Sigma_{j=1}^{n} a_j^2/(a_j^2 + b_j^2)\ \Sigma_{j=1}^{n} b_j^2/(a_j^2 + b_j^2) - [\Sigma_{j=1}^{n} a_j b_j/(a_j^2 + b_j^2)]^2\}$.

Compare applying LSDT, the LSM, least normed square method (LNSM), autoerror equalizing method (AEM), and direct solution method (DSM) [2-4] to test equation set

$29x + 21y = 50,\ 50x - 17y = 33,\ x + 2y = 7,\ 2x - 3y = 0,$

See Figure 4.9, Figure 4.10. The LSM gives $x \approx 1.0023$, $y \approx 1.0075$ practically ignoring the last two equations with smaller factors (unlike LSDT, the AEM, DSM, and even LNSM):

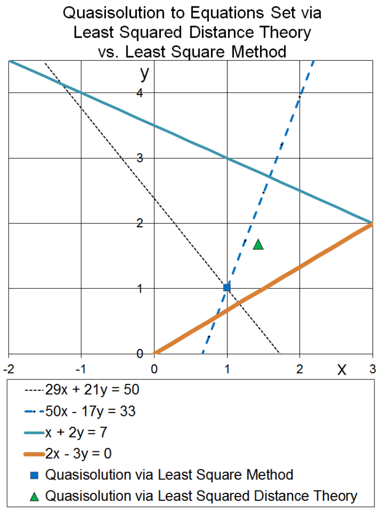

Figure 4.9

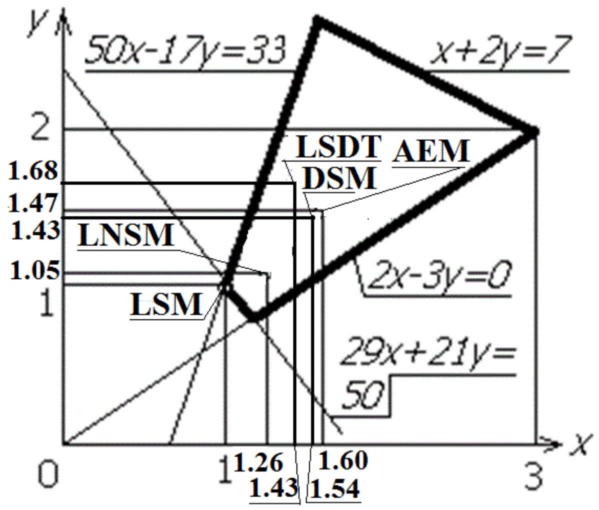

Figure 4.10

Least squared distance theory providing simple explicit quasisolutions (further improvable, e.g., via using biquadratic distances) to even contradictory problems is very efficient by solving very different problems, e.g. in aeronautical fatigue.

Acknowledgements

to Anatolij Gelimson for our constructive discussions on coordinate system transformation invariances and his very useful remarks.

References

[1] Encyclopaedia of Mathematics. Ed. M. Hazewinkel. Volumes 1 to 10. Kluwer Academic Publ., Dordrecht, 1988-1994
[2] Gelimson L. G. Elastic Mathematics. General Strength Theory. The "Collegium" International Academy of Sciences Publishers, Munich, 2004
[3] Gelimson L. G. Providing Helicopter Fatigue Strength: Flight Conditions. In: Structural Integrity of Advanced Aircraft and Life Extension for Current Fleets – Lessons Learned in 50 Years After the Comet Accidents, Proceedings of the 23rd ICAF Symposium, Dalle Donne, C. (Ed.), 2005, Hamburg, Vol. II, 405-416
[4] Gelimson L. G. Overmathematics: Fundamental Principles, Theories, Methods, and Laws of Science. The "Collegium" All World Academy of Sciences Publishers, Munich, 2010

[5] Gelimson L. G. Fundamental Science of Solving General Problems. The ”Collegium” All World Academy of Sciences Publishers, Munich, 2010
[6] Gelimson L. G. Corrections and Generalizations of the Least Square Method. In: Review of Aeronautical Fatigue Investigations in Germany during the Period May 2007 to April 2009, Ed. Dr. Claudio Dalle Donne, Pascal Vermeer, CTO/IW/MS-2009-076 Technical Report, International Committee on Aeronautical Fatigue, ICAF 2009, EADS Innovation Works Germany, 2009, 59-60

5 Fatigue and Fracture of Metallic Fuselage Materials

5.1 General Power Strength Theory in Fundamental Material Strength Sciences

L. G. Gelimson (IFS)

The τ_L/σ_L ratio of shear τ_L and normal σ_L limiting stresses of (also aircraft) materials [1] can substantially deviate from 1/2 (Tresca) and $3^{-1/2}$ (Mises) taking values at least between 0.25 and 1. Limiting surfaces can be convex by $1/2 \le \tau_L/\sigma_L \le 2/3$ only [2].
In fundamental material strength sciences [3, 4], general power strength theory including general linear strength theory generalizing Yu’s twin shear unified strength theory [2] also fits all these and other data. Use principal stresses $\sigma_1 \ge \sigma_2 \ge \sigma_3$, limiting stress σ_L such as yield stress σ_y or ultimate strength σ_u , namely σ_{Lt} in tension and σ_{Lc} in compression with $\sigma_{Lc} \ge 0$ and $\alpha = \sigma_{Lt}/\sigma_{Lc}$ if $\sigma_{Lt} \ne \sigma_{Lc}$. Define relative (reduced) principal stresses σ_j° via dividing σ_j by the modulus $|\sigma_{jL}|$ of σ_{jL} of the same sign in the same direction by vanishing the remaining two principal stresses under the same remaining load conditions: $\sigma_j^\circ = \sigma_j / |\sigma_{jL}|$ (j = 1, 2, 3), $\sigma_1^\circ \ge \sigma_2^\circ \ge \sigma_3^\circ$. Consider one-sided limitations for σ_e and σ_e° whose values can be negative or imaginary and use nonnegative $|\sigma_e|$ and $|\sigma_e^\circ|$. Generalize Hosford’s criterion via

$$\sigma_e = [a_{13}(\sigma_1 - \sigma_3)^k + a_{12}(\sigma_1 - \sigma_2)^k + a_{23}(\sigma_2 - \sigma_3)^k]^{1/k} \le \sigma_L \ (k > 0).$$

Uniaxial limiting stresses in tension and compression give strength criteria form

$$\sigma_e^\circ = \{a(\sigma_1^\circ - \sigma_3^\circ)^k + (1 - a)[(\sigma_1^\circ - \sigma_2^\circ)^k + (\sigma_2^\circ - \sigma_3^\circ)^k]\}^{1/k} \le 1.$$

Pure shear reduced limiting stresses $\sigma_1^\circ = \tau_L/\sigma_{Lt}$, $\sigma_2^\circ = 0$, $\sigma_3^\circ = -\tau_L/\sigma_{Lc}$ give ($k \ne 1$)

$$\sigma_e^\circ = \{(\sigma_{Lt}^k\sigma_{Lc}^k/\tau_L^k - \sigma_{Lt}^k - \sigma_{Lc}^k)/[(\sigma_{Lt} + \sigma_{Lc})^k - \sigma_{Lt}^k - \sigma_{Lc}^k](\sigma_1^\circ - \sigma_3^\circ)^k +$$
$$[(\sigma_{Lt} + \sigma_{Lc})^k - \sigma_{Lt}^k\sigma_{Lc}^k/\tau_L^k]/[(\sigma_{Lt} + \sigma_{Lc})^k - \sigma_{Lt}^k - \sigma_{Lc}^k][(\sigma_1^\circ - \sigma_2^\circ)^k + (\sigma_2^\circ - \sigma_3^\circ)^k]\}^{1/k} \le 1.$$

In the simplest case k = 2 and then additionally by $\sigma_{Lt} = \sigma_{Lc} = \sigma_L$, we have criteria

$$\sigma_e^\circ = \{[\sigma_{Lt}\sigma_{Lc}/(2\tau_L^2) - (\sigma_{Lt}^2 + \sigma_{Lc}^2)/(2\sigma_{Lt}\sigma_{Lc})](\sigma_1^\circ - \sigma_3^\circ)^2 +$$
$$[(\sigma_{Lt}^2 + \sigma_{Lc}^2)/(2\sigma_{Lt}\sigma_{Lc}) - \sigma_{Lt}\sigma_{Lc}/(2\tau_L^2)][(\sigma_1^\circ - \sigma_2^\circ)^2 + (\sigma_2^\circ - \sigma_3^\circ)^2]\}^{1/2} \le 1,$$
$$\sigma_e^\circ = \{[\sigma_L^2/(2\tau_L^2) - 1](\sigma_1^\circ - \sigma_3^\circ)^2 + [2 - \sigma_L^2/(2\tau_L^2)][(\sigma_1^\circ - \sigma_2^\circ)^2 + (\sigma_2^\circ - \sigma_3^\circ)^2]\}^{1/2} \le 1,$$
$$\sigma_e^\circ = \sigma_1^\circ - \sigma_3^\circ \le 1 \text{ (universalized Tresca's criterion) by } \tau_L/\sigma_L = 1/2,$$
$$\sigma_e^\circ = \{[(\sigma_1^\circ - \sigma_3^\circ)^2 + (\sigma_1^\circ - \sigma_2^\circ)^2 + (\sigma_2^\circ - \sigma_3^\circ)^2]/2\}^{1/2} \le 1 \text{ (Mises et al.) by } \tau_L/\sigma_L = 1/3^{1/2},$$
$$\sigma_e^\circ = [(\sigma_1^\circ - \sigma_2^\circ)^2 + (\sigma_2^\circ - \sigma_3^\circ)^2]^{1/2} \le 1 \text{ by } \tau_L/\sigma_L = 1/2^{1/2}.$$

Use general homogeneous symmetric polynomials $P_i(\sigma_{1n}^\circ, \sigma_{2n}^\circ, \sigma_{3n}^\circ)$ of power i :

$$\sigma_e^\circ = [\textstyle\sum_{i=0}^N a_iP_i(\sigma_{1n}^\circ, \sigma_{2n}^\circ, \sigma_{3n}^\circ)]^{1/N} \le 1.$$

In the unstressed state, $\sigma_e^\circ = 0$ is natural and leads to $a_0 = 0$. Case N = 2 gives form

$$\sigma_e^\circ = [a_1(\sigma_{1n}^\circ + \sigma_{2n}^\circ + \sigma_{3n}^\circ) + a_2(\sigma_{1n}^{\circ 2} + \sigma_{2n}^{\circ 2} + \sigma_{3n}^{\circ 2}) +$$
$$b_2(\sigma_{1n}^\circ\sigma_{2n}^\circ + \sigma_{1n}^\circ\sigma_{3n}^\circ + \sigma_{2n}^\circ\sigma_{3n}^\circ)]^{1/2} \le 1.$$

Replace usual $\sigma_1 + \sigma_2 + \sigma_3$ and reduced $\sigma_{1n}° + \sigma_{2n}° + \sigma_{3n}°$ "hydrostatic sums" with their continuous functions f and f° vanishing at $-\sigma_{Lc}$, 0, σ_{Lt} and -1, 0, 1, respectively:

$\sigma_e° = [\sigma_{1n}^{\circ 2} + \sigma_{2n}^{\circ 2} + \sigma_{3n}^{\circ 2} - a(\sigma_{1n}°\sigma_{2n}° + \sigma_{1n}°\sigma_{3n}° + \sigma_{2n}°\sigma_{3n}°) +$
$bf°(\sigma_{1n}° + \sigma_{2n}° + \sigma_{3n}°)]^{1/2} \le 1.$

Constant a provides considering true values of τ_L/σ_L and not only predefined $3^{-1/2}$ by a = 1. This leads by b = 0 to ellipsoidal (by -2 < a < 1) and hyperboloidal (by a > 1) limiting surfaces and to "hydrostatic" strength limited in compression and unlimited in tension with concavity everywhere, respectively. This clearly contradicts strength test data and Drucker's postulate. The Huber-von-Mises-Hencky cylinder lies between those limiting surfaces as their limiting case, see Figure 5.1.

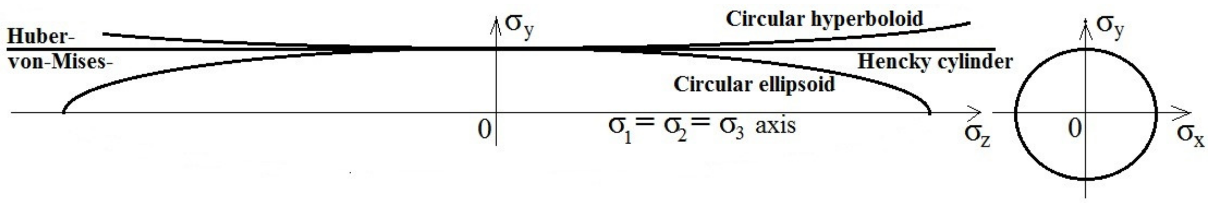

Figure 5.1

Using b ≠ 0 with
$f°(\sigma_{1n}° + \sigma_{2n}° + \sigma_{3n}°) = \sigma_{1n}° + \sigma_{2n}° + \sigma_{3n}° + 1$ if $\sigma_{1n}° + \sigma_{2n}° + \sigma_{3n}° \le -1$,
$f(\sigma_{1n}° + \sigma_{2n}° + \sigma_{3n}°) = 0$ if $-1 \le \sigma_{1n}° + \sigma_{2n}° + \sigma_{3n}° \le 1$,
$f(\sigma_{1n}° + \sigma_{2n}° + \sigma_{3n}°) = \sigma_{1n}° + \sigma_{2n}° + \sigma_{3n}° - 1$ if $\sigma_{1n}° + \sigma_{2n}° + \sigma_{3n}° \ge 1$,

makes limiting surfaces paraboloidal. Hence general power strength theory provides considering any ratio of shear and normal limiting stresses of (also aircraft) materials.

References

[1] Gelimson L. G. Strength Criteria Generally Considering Relations Between the Shear and Normal Limiting Stresses. The "Collegium" All World Academy of Sciences Publishers, Munich, 2010
[2] Yu M. H. Advances in strength theories for materials under complex stress state in the 20th Century // Appl. Mech. Rev. – 2002. – 55. – No. 3. – P. 169 – 218.
[3] Gelimson L. G. Providing Helicopter Fatigue Strength: Unit loads. In: Structural Integrity of Advanced Aircraft and Life Extension for Current Fleets – Lessons Learned in 50 Years After the Comet Accidents, Proceedings of the 23rd ICAF Symposium, Dalle Donne, C. (Ed.), 2005, Hamburg, Vol. II, 589 – 600
[4] Gelimson L. G. Elastic Mathematics. General Strength Theory. – Munich, The "Collegium" All World Academy of Sciences Publishers, 2004. – 496 pp.

6 Fatigue and Fracture of Composites

6.1 Investigations on Environmental Fatigue of CFRP Foam Core Sandwich Structures

M. John, M. Rinker (Fraunhofer Halle), P. C. Zahlen (CTC), R. Schäuble (Fraunhofer Halle)

Sandwich structures made of carbon fibre reinforced face sheets with a lightweight polymeric foam core are predestined for an application as primary structure in commercial aircrafts. Beside the good ratio of bending strength and stiffness to weight the manufacturing process provides high integral modifications of the sandwich elements [1]. The investigated sandwich structure was manufactured in one piece by an open mould vacuum infusion process at CTC GmbH [3]. It consists out of a Polymethacrylimide- (PMI-) foam core, two symmetric face sheets of Non Crimp Fabrics (NCF) and a matrix of epoxy resin.

The service loads of a primary structure are superposed by quite a few environmental conditions over a long life time period. Hence the structure needs a sizing with respect to large cyclic temperature changes. Beside this the influence of moisture uptake at humid environment and the time parameter are important facts which have to be considered [4].
This work was focused on the behaviour after the environmental exposures took place and while special conditions were running. Several experimental investigations were made to determine the time, temperature and moisture dependency of the mechanical behaviour. The studies were made not only for the sandwich composite itself, but also for the single components of the structure.
On the one hand single foam core sheets and single face sheet layers with different thicknesses were stored under 70℃ and 85% relative humidity (RH) to observe the maximum uptake of water at these conditions and estimate the diffusion coefficients of the sandwich parts. Furthermore the relaxation behaviour of the PMI-foam ROHACELL®RIST was determined under uniaxial tension load at various temperatures between 23℃ and 140℃ and different constant strain levels.

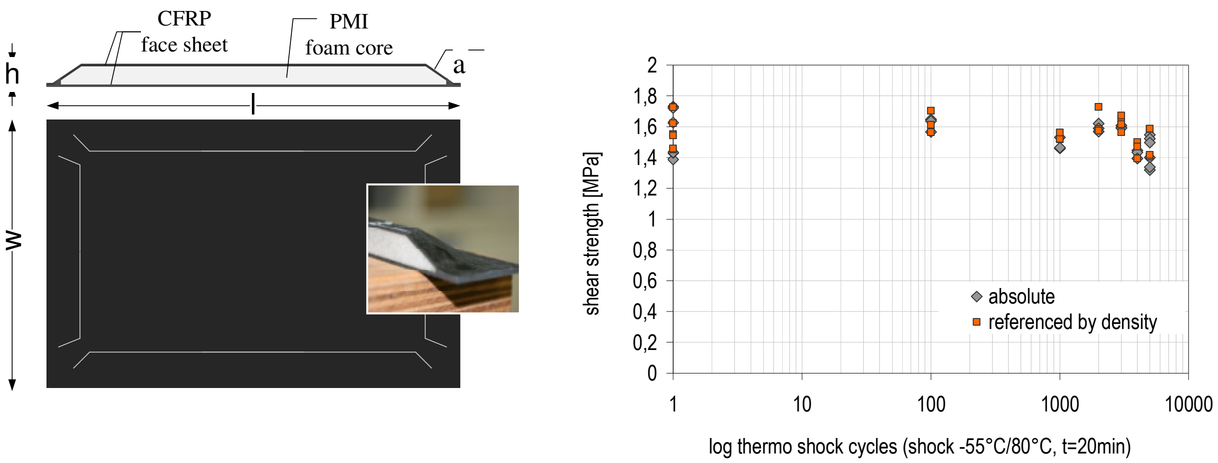

Figure 6.1 a: Geometry of closed CFRP Sandwich Panel; b. Shear strength vs. number of thermo shock cycles [4]

On the other hand the whole sandwich composite is treated under the same hot-wet conditions like the single components at first; the moisture uptake was estimated up to 6 month by weighting. Therefore sandwich panels without open foam sites were used. The laterally closed sandwich structure is called a sandwich pillow because of its dimensions about 560mm x 360mm and the flattened edges of the CFRP face sheet layers, shown in Figure 6.1a. This sandwich pillow was defined as a representative structure on element level. The geometry was estimated by Finite Element calculation with smooth edges to prevent local stress peaks within the foam core. Another series of sandwich pillows was treated by thermo shock experiments by cycling between -55℃ and 80℃ with a rate of 44 K/min.
After the moisture or temperature treatment the sandwich pillow was cut into three 4-Point-Bending-Specimens (4PB) according to the Standard ASTM C-393. The 4PB experiments were made with a servo hydraulic test machine. In addition a contact-free optical measurement sys-

tem was used to determine the exact strain via gray scale pattern on the specimen surface. The typical shear failure of the foam core at 4PB occurred. The estimated strength versus the number of thermo shock cycles is plotted in Figure 6.1b. The shear strength was corrected by the quotient of measured to ideal value of the foam density for each specimen.

At all experimental setups residual stresses are still present. Hence they have to be considered for each environmental situation. The manufacturing process causes thermal induced residual stress by the discrepancy of the different coefficients of thermal expansion (CTE) of the face sheets and the foam core [2].

The influence on mechanical properties by the interaction of residual stresses, temperature and strain dependent relaxation behaviour as well as the influence of water on these phenomena is a process of high complexity. These are hardly to describe independent from each other because they coexist in each situation in service. With the help of the experiments a number of snap-shots of the mechanical behaviour at several atmospheric conditions were caught. In future it is possible to put them together to a multi environmental behaviour of the sandwich structure with the help of analytical descriptions and finite element modelling. The challenge is to describe how strong they are connected and how big the influencing factor of each phenomenon is.
There is some more work to do, but at the current state it has to be recognized that the CFRP foam core sandwich structure could resist extreme thermal and hygrothermal conditions without lost of global mechanical behaviour.

The work presented in this article was partially funded by CTC Stade GmbH and the Bundesministerium für Wirtschaft und Technologie of Germany (Federal Ministry of Economics and Technology). The authors wish to acknowledge this support.

References

[1] A.S. Herrmann, P.C. Zahlen and I. Zuardy: Sandwich Structures Technology in Commercial Aviation. 7th International Conference on Sandwich Structures, Aalborg, 2005.
[2] M. Rinker, M. Gutwinski , R. Schäuble: Experimental and Theoretical Investigation of Thermal Stress in CFRP Foam-core Sandwich Structures. 13th International Conference on Composite Materials, European Society for Composite Materials, Stockholm, 2008.
[3] P.C. Zahlen, M. Rinker, C. Heim: Advanced Manufacturing of Large, Complex Foam Core Sandwich Panels. ICSS 8, Porto, 2008.
[4] John M., Rinker M., Zahlen P. C. and Schäuble R.: Effects of thermal and humidity treatment on mechanical properties of CFRP foam core sandwich structures, ECCM14, Budapest, 2010.

6.2 Simulation and Experimental Evaluation of Mixed Mode Delamination in Multidirectional CF/PEEK Laminates under Fatigue Loading

Parya Naghipour, Janine Schneider, Marion Bartsch, Heinz Voggenreiter (DLR)

The need for light weight structural materials with good resistance to fatigue has led designers of aerospace industry to increasingly employ CFRP structures, when especially cyclic loading is of primary concern. Fiber reinforced composites often exhibit complex failure mechanisms as an interaction of intra-laminar damage modes such as matrix cracking and fiber rupture and interlaminar damage modes, predominantly delamination . One of the most appealing techniques that can be used for simulating delamination initiation and propagation in composites is the cohesive zone approach [1]. The cohesive zone approach adopted in this work makes use of interface finite elements incorporating a cohesive mixed-mode damage model. The zero thickness 8 node cohesive elements, implemented as a user element subroutine, are mainly based on the constitutive model suggested by Turon et al [1]. The relationship between the vector of interface tractions (**τ**) and relative displacements (**δ**) can be written as

$$\boldsymbol{\tau} = \left(\begin{matrix} (1-d)K & 0 & 0 \\ 0 & (1-d)K & 0 \\ 0 & 0 & (1-d)K \end{matrix} \right) + \begin{bmatrix} 0 \\ 0 \\ dK\ H(-\delta_n) \end{bmatrix} \boldsymbol{\delta} \tag{1}$$

K stands for the initial stiffness bonding both faces of the interface element together before any initiation of damage. H stands for the Heaviside function (H (x)=1 if x ›0), which is used to avoid the interpenetration of the interface surfaces under compressive strains. The damage parameter, *d*, governs the softening behaviour of the interface and it increases from 0 (no damage) to 1 (complete separation) for monotonous load progression. As subjected to cyclic loading, the constitutive law of the interface element must be reformulated to account for subcritical damage accumulation and stiffness degradation within subsequent unloading-reloading steps [1]. Therefore, the degradation of the interface stiffness, *K*, or the evolution of the damage parameter, *d*, per cycle must be defined explicitly in order to degrade the mentioned tractions or interfacial strengths in each unloading- reloading step. The followed numerical approach in this work incorporates the interface formulation suggested by Turon et al. [1] for modelling the mixed mode delamination crack growth under cyclic loading further enhanced by reformulation of the cohesive zone area [2]. The fatigue damage evolution law (Equation 2) is a cohesive law that links fracture and damage mechanics to establish the evolution of the damage variable, *d*, in terms of the crack growth rate *dA/dN* or energy release rate, ΔG.

$$\frac{\partial d}{\partial N} = \left\{ \begin{matrix} \dfrac{1}{A_{cz}} \dfrac{(\delta_m^f(1-d)+d\delta_m^0)^2}{\delta_m^f \delta_m^0} C \left(\dfrac{\Delta G}{G_c} \right)^m & \mathrm{G_{th}} < G_{\max} < G_c \\ 0 & 0 \end{matrix} \right\} \tag{2}$$

C, *m,* and G_{th} are Paris plot parameters that are obtained by plotting ∂a/∂n versus cyclic variation in the energy release rate, ΔG, on log-log scale. G_c is the total mixed mode fracture toughness under a specific mode ratio. δ_m^0 stands for delamination onset, and δ_m^f , for final separation in the interface element [2].

The composite laminate in this study is composed of multidirectional carbon fiber reinforced plastic (CFRP) plies with varying fiber orientations. The effect of varying fiber orientations, different stacking sequences and combination of inter- and intra-laminar damage modes on the cyclic mixed mode delamination failure of the constituent have been investigated numerically and experimentally. Two different layups, (layup QI and layup 22.5) have been tested here, with the first designating a quasi-isotropic layup $[[0/\pm 45/90]_6]$ and the second one with alternating +22.5° and -22.5° fiber orientations $[(+22.5/-22.5)_{12}]$. In the numerical finite element model, each CFRP lamina is assumed as an orthotropic homogenized continuum under plane stress, permitting the modelling of damage initiation in each ply under the combination of longitudinal (in fiber direction), transverse and shear stress states.

The interface elements, lying in the delamination plane, are represented via the cohesive zone concept (equation. 1 and 2), implemented as a user defined element routine (UEL) in Abaqus. In conclusion, for the chosen multidirectional layups subjected to 50% cyclic mixed mode loading, the numerical model predicts the degradation of the applied load within successive cycles successfully when compared with the corresponding experiments (Figure 6.2).

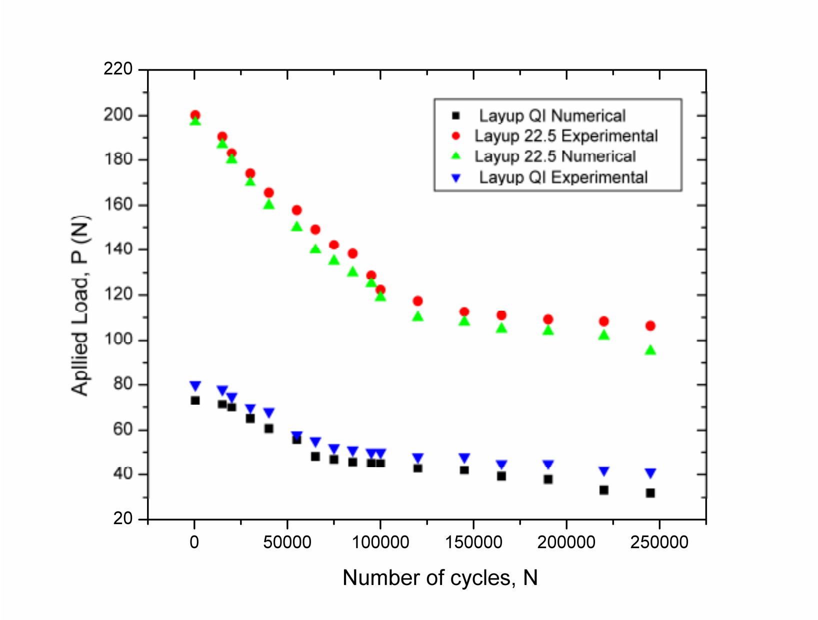

Figure 6.2 Reduction of the applied load (P) within successive cycles with addition of cyclic damage law to the constitutive behaviour of the cohesive elements (mode mixity 50%)

Fracture surfaces of delamination cracks after cyclic loading in mixed mode bending under a mode mixity of 50% were investigated for layup 22.5 and layup QI by SEM, in order to obtain more detailed information about the ongoing cyclic damage mechanisms (Figure 6.3). For layup 22.5 (Figure 6.3a), under cyclic loading a significant fracture feature is the appearance of asperities in the form of shear cusps, which are formed due to microcrack nucleation ahead of the crack tip and inelastic straining of the ligaments until rupture. Appearance of broken fibres or fibres pulled out transversally to the longitudinal direction is also an important fracture surface characteristics observed in layup 22.5. In layup QI, matrix fracture areas, tilted slightly to the overall fracture surface, can be found in the related SEM micrograph (Figure 6.3b). Very few broken fibres are present in the fracture surface compared to layup 22.5, which also results in a lower fracture load of layup QI compared to layup 22.5.

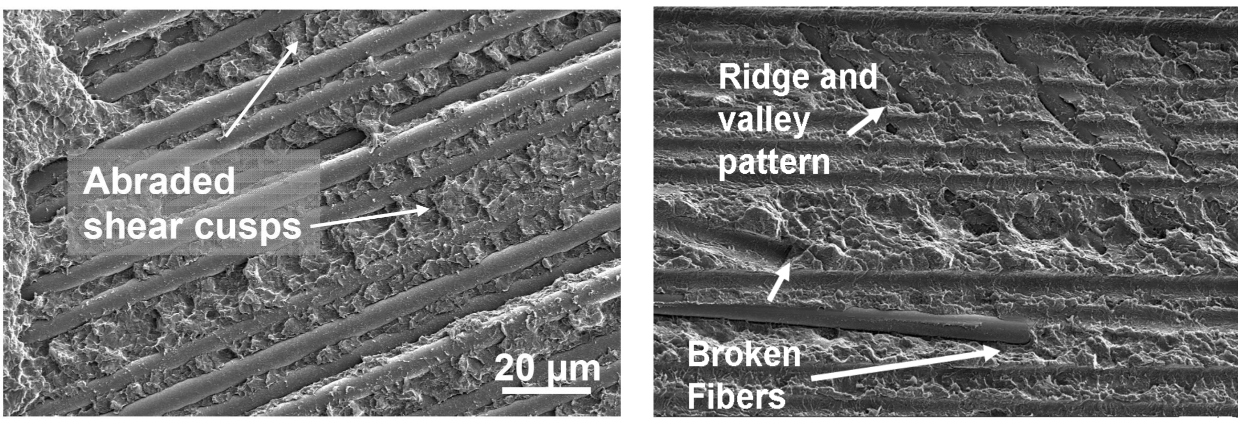

Figure 6.3 a) Fracture surface with deformed and abraded shear cusps (layup 22.5) and b) with ridges and valleys (layup QI)

References:

[1] Turon A, Costa J, Camanho P.P, Davila, C.G. Simulation of delamination in composites under high-cycle fatigue". Composites Part A: 2007; 38 (11):2270-82.
[2] Naghipour P, Bartsch M, Voggenreiter H. Simulation and experimental validation of mixed mode delamination in multidirectional CF/PEEK laminates under fatigue loading. International Journal of Solids and Structures 2011; 48: 1070–1081.

6.3 Fatigue properties of hybrid Ti/CFRP laminates

K. Schulze, J. Hausmann (DLR), B. Wielage (TU Chemnitz)

Introduction:

Hybrid Ti/CFRP laminates, composed of titanium foils with carbon fibre reinforced thermoplastics plies in between, are under development to satisfy the requirements for future aerospace applications. Fibre Metal Laminates (FML) join the advantages of polymer matrix composites, e.g. high specific stiffness and strength and the advantages of the metal, e.g. isotropic properties, electrically conductive and superior bearing capabilities. Thermoplastic Fibre Metal Laminates (TFML) offer additional advantages over their thermosetting counterparts such as outstanding interlaminar fracture properties, high impact tolerance and a superior resistance to aggressive environments.

Material and processing:

Hybrid Ti/CFRP laminates investigated at the German Aerospace Center envelope three layers of titanium (Ti-6Al-4V) and two plies of carbon fibre reinforced polyetheretherketone (CF/PEEK) as shown on Figure 6.4. Before manufacturing the hybrid Ti/CFRP panels the titanium foils were grit blasted to improve the adhesion of the PEEK. In contrast to thermosetting materials hybrid Ti/CFRP laminates were made by autoclaveless vacuum consolidation technique [1]. The titanium foils and CF/PEEK plies were stacked together and covered with a vacuum bag. After applying vacuum, the hybrid panel was heated up to 400℃ to melt the PEEK matrix for consolidation and bonding to the metal. Ti/CFRP laminates with fibre orientations of (a) ± 22.5°, (b) ± 67.5°, and (c) 90° within the CFRP ply are made for investigation. When processing hybrid Ti/CFRP laminates thermal residual stresses arise due to the mismatch of the coefficients of thermal expansion (CTE) between the individual layers and and cooling down from high process temperature.

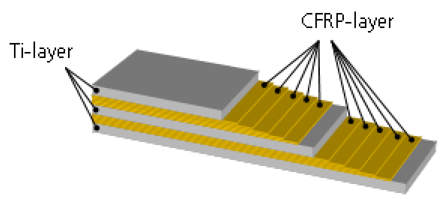

Figure 6.4: Composition of hybrid Ti/CFRP laminates

Tensile and fatigue testing

To determine the ultimate strength of hybrid Ti/CFRP laminates at above mentioned carbon fibre orientations tensile testing was conducted at a universal testing machine at a displacement rate of 1mm/min. The constant amplitude fatigue testing was conducted at a servo hydraulic testing machine in tension-tension loading. The applied frequency was 1.0Hz, the applied stress ratio was R=0.1, and the applied load was 75% of the ultimate tensile strength as maximum stress.

Results and discussion

The lower the angle of the carbon fibres within the CFRP ply of Ti/CFRP laminates related to the applied load the higher the stiffness and strength but the lower the strain. Ti/CFRP laminates with low fibre angles such as $\theta = \pm 22.5°$ exhibit carbon fibre dominated behaviour whereas Ti/CFRP laminates with high fibre angles such as $\theta = \pm 67.5°$ and $\theta = 90°$, respectively, exhibit metal dominated behaviour. With increasing carbon fibre angle within the CFRP ply Ti/CFRP laminates show enhanced fatigue behaviour as shown in Figure 6.5a.
Independent of the carbon fibre orientation the young modulus of the hybrid Ti/CFRP laminate is greater than the young modulus of the CFPR ply and less than the young modulus of the titanium layer. Under consideration of this mismatch the applied tension load on the titanium layers are greater and the applied tension load on the CFRP plies are less than the applied tension load on the laminate. During fatigue testing the applied tensile loading and the residual stresses (tension, compression) superpose. Thus, these stresses have to be taken into account since they affect the fatigue properties. The residual stresses building up within the individual layers (CFRP, titanium) as a function of the fibre orientation within the CFRP plies [2] is shown in Figure 6.5b schematically. Depending on the carbon fibre orientation the individual layers exhibit either residual tension stress or residual compression stress [3]. The superposition of residual tension stress and applied tension loading results actually in greater tension loading. In contrast to that, the superposition of residual compression stress and applied tension loading results actually in less stress within the individual layer. If the magnitude of residual compression stress is great enough the fatigue test condition alters from tension-tension loading to tension-compression loading for the individual layer.

With increasing carbon fibre angle within the CFRP plies the residual stress and thus the actual resulting load of the titanium layers decrease; more precisely at fibre orientations of $\theta < \pm 53°$ the titanium layers exhibit residual tension stress and at fibre orientations of $\theta > \pm 53°$ titanium layers exhibit residual compression stress. At fibre orientation of $\theta = \pm 22.5°$ the resulting maximum stress of the titanium layers is approx. in the range of yield strength. At high fibre angles ($\theta = \pm 67.5°$, $\theta = 90°$) the actual maximal stress of the titanium layers is below the fatigue strength. At fibre orientation of $\theta = 90°$ the condition during fatigue testing exhibit tension-compression loading for the titanium layers.

With increasing carbon fibre angle within the CFRP plies the residual stress and thus the resulting stress of the CFRP plies increase; more precisely at fibre angles of $\theta < \pm 53°$ CFRP plies exhibit residual compression stress and at fibre angles of $\theta > \pm 53°$ CFRP plies exhibit residual compression stress. At fibre angles of $\theta = \pm 22.5°$ the resulting maximum stress of the CFRP plies is below the ultimate strength but due to the great magnitude of residual compression stress the condition during fatigue testing exhibit tension-compression load. At fibre angles of $\theta = \pm 67.5°$ the resulting maximum stress of the CFRP plies is approx. in the range of ultimate strength. At fibre orientation of $\theta = 90°$ the residual tension stress of the CFRP plies is already close to ultimate strength.

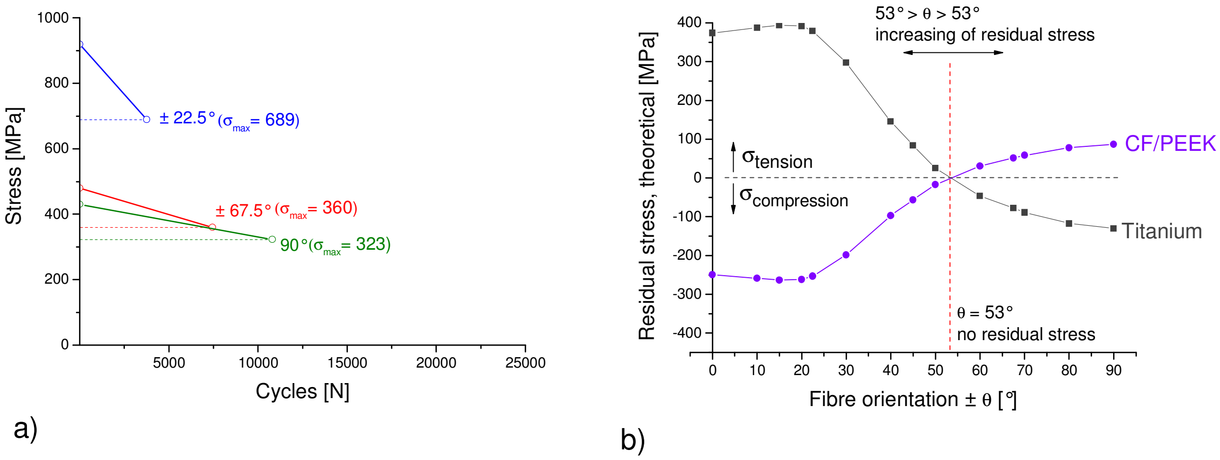

Figure 6.5 a) fatigue behaviour of Ti/CFRP laminates, b) residual stress of Ti- and CFRP ply

Conclusion and Outlook:

Hybrid Ti/CFRP laminates with low carbon fibre orientation angles within the CFRP ply show good tensile but adverse fatigue properties due to the high magnitude of residual tension stress of the titanium layer as well as due to the high magnitude of residual compression stress of the CFRP plies.

Methods for reducing residual stress of hybrid Ti/CFRP laminates with low carbon fibre angle within the CFRP ply, e.g. by post-thermal treatments are investigated prospectively.

References

[1] Horn, M. Kaden, M., Keck, R.: Influence of production technology on the consolidation of fibre reinforced high performance thermoplastics, 14th European Conference on Composite Materials, 7-10 Juni 2010 in Budapest (Ungarn)

[2] Barnes, J. A., Simms, I. J. et al.: Thermal expansion characteristics of PEEK composites, Journal of Materials Science, 26 (1991), S. 2259-2271

[3] Cortés, P. and W. J. Cantwell: The prediction of tensile failure in titanium-based thermoplastic fibre-metal laminates, Composites Science and Technology, 66 (2006) 13, S. 2306-2316

6.4 Numerical and Experimental Investigation on Lap Shear Fracture of Ti/PEEK Joints

K. Schulze, P. Naghipour, J. Hausmann, M. Bartsch, (DLR) B. Wielage (TU Chemnitz)

Introduction:

Lap shear fracture of hybrid Ti/CFRP laminates is an important point of interest for aerospace industry, since these laminates are being considered as reliable candidates to be used in bolted and bonded joints subjected to high values of lap shear loads [1-3]. Nevertheless, lap shear behaviour of hybrid laminates and effects of specimen geometry on the shear fracture of these laminates remains largely unexplored. Papini et al. [4] conducted some experimental, and Kafkalidis and Thouless [5], Shen et al. [6] carried out combined experimental and numerical studies of lap shear behaviour only for metal/metal interfaces but not for hybrid metal/CFRP laminates, which involves more complexity. Therefore, the main objective of this investigation was to thoroughly analyze the quasi-static lap shear fracture of titanium – PEEK joints with a numerical Finite Element (FE) model followed by experimental validations.

Material and processing:

Titanium-PEEK lap shear specimen considered in this study is composed of pre-treated titanium plates (Ti-3Al-2.5V) bonded with a 0.1 mm thick PEEK foil. The used titanium plates have a length of 72.5 mm, a width of 10 mm and a thickness of 1.6 mm. The used PEEK foil has a thickness of 0.1 mm. The lap shear specimens have an adherent area of 10 mm x 5 mm (Fig.1a). Before manufacturing the lap shear specimens the titanium plates were grit blasted with alumina to improve the adhesion of the PEEK. The titanium plates and the PEEK foil were cleaned to remove contamination and to degrease the surface. The cleaned components were dried and the lap shear samples were made in a laboratory furnace at a consolidation temperature of 400°C by using a manufacturing tool for ensuring uniform specimens with uniform adherent areas.

Lap-shear fracture experiments and numerical simulation

The quasi-static lap shear experiment was carried out with a cross-head displacement rate of 0.5 mm/min. The machine used is a 10 tons Instron testing machine equipped with a 10 kN load cell to measure the load for lap shear fracture. The cross-head displacement and load histories were recorded. Three specimens were tested for assuring output data accuracy. The developed numerical model, created in ABAQUS and consisting of 2 titanium layers, a PEEK ply in between them and cohesive elements lying in the Ti/PEEK interface, is validated through comparison with experimental data (Figure 6.6a). The results designate that a good agreement is achieved in load-displacement response with an approximate 10% error in the predicted load for the specified displacement value. According to the numerical model, the evolution of the interface damage starts at 15% of the ultimate load and follows a faster trend closer to the final failure (Figure 6.6a).

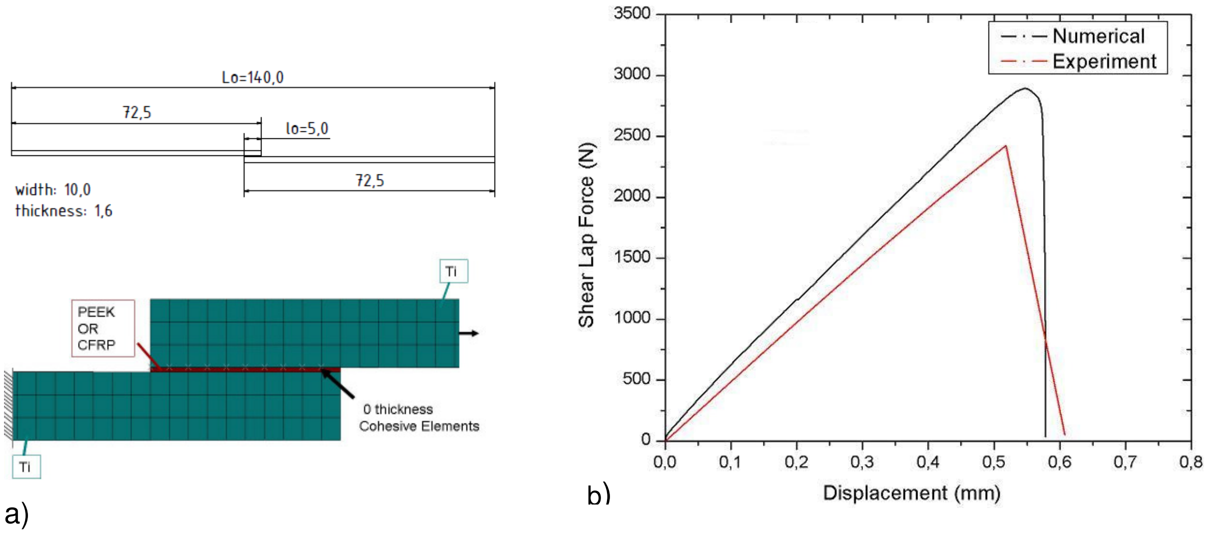

Figure 6.6 Lap-Shear Ti/PEEK Specimen a) and Lap-Shear load-displacement experimentally and numerically

Effects of specimen geometry on lap shear fracture of hybrid specimen

The effect of overlap length on the lap shear fracture of the hybrid laminate is shown in Figure 6.7a (both fracture load and overlap length values are normalized). Maximum value of the lap shear fracture load increases slightly with increasing overlap length, showing that high overlap length provides more resistance to fracture. However, the increase rate is low enough to conclude that the overlap length changes do not have a sensible effect on load-displacement response of the laminate. In other words an asymptotic steady state response is observed as long as the overlap length of the specimen is long enough. A slight increase was observed as total length of the hybrid specimen was increased (Figure 6.7b). Some inconsistencies viewed in the value of fracture load could be solved easily with increasing step time incrementation. Nevertheless, the obtained fracture load values were close enough to say the length of specimen does not have a strong effect on the maximum force value (both fracture load and total length values were normalized). The first higher initial increase rate which was observed by rising the overlap length is not observed here. Hence, it can be concluded that the lap shear fracture is less sensitive to total length changes than the changes in the overlap length.

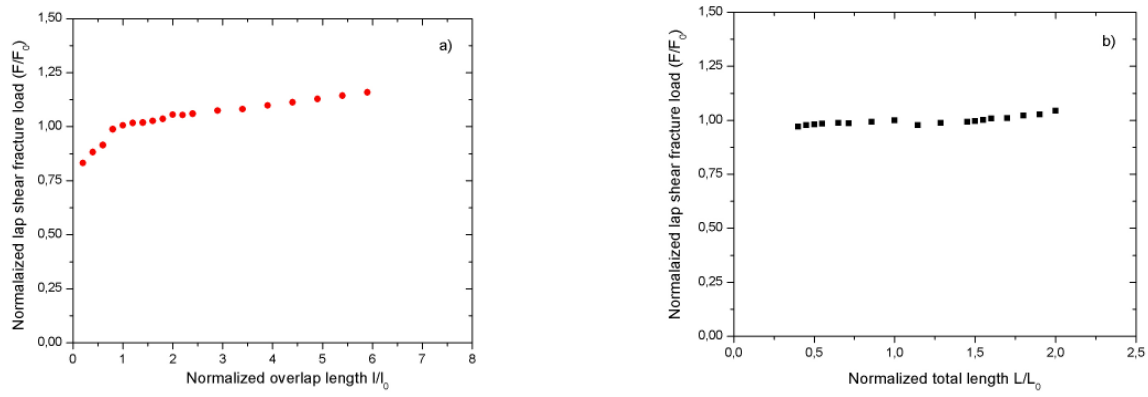

Figure 6.7 Effect of overlap length a) and total length b) on shear fracture response of the hybrid laminate

Outlook

The next step would be investigating the lap shear fracture between a carbon fibre reinforced PEEK (CFRP) layup and a Titanium layer. The lap shear load, fracture surfaces, and effects of interface properties on the fracture process will be studied thoroughly. Similar to this study, the results of numerical simulations will also be validated through corresponding experiments.

References

[1] Nilsson S. Increasing the strength of graphite/epoxy bolted joints by introducing an adhesively bonded metallic insert. J Compos Mater. 1989:643–50.
[2] Van Rooijen R. G. J, Sinke J, De Vries T. J, Van Der Zwaag S. The Bearing Strength of Fiber Metal Laminates. Journal of Composite Materials (40), 2006, 5-19.
[3] Camanho P.P, Fink A, Obst A, Pimenta S. Hybrid titanium–CFRP laminates for high-performance bolted joints. Composites: Part A 2009; 40: 1826–1837
[4] M. Papini, G. Fernlund, J.K. Spelt, “The effect of geometry on the fracture of adhesive joints”, International Journal of adhesion and Adheshives, (14), 1194, 5-13.
[5] M. S. Kafkalidis, M. D. Thouless, The effects of geometry and material properties on the fracture of single lap-shear joints, International Journal of Solids and structures (17), 2002, 4367-4383.
[6] Y.-L. Shen, N. Chawla, E.S. Ege, X. Deng. Deformation analysis of lap-shear testing of solder joints. Acta Materialia, 2005; 53: 2633–2642

6.5 Hybrid Composite Structures (HyCoS)

Dr. T. Haberle, E. Yip (RUAG)

The aim of the research project **Hy**brid **C**omposite **S**tructures (HyCoS) in collaboration with the Technical University of Munich (TUM) and the German Aerospace Institute (DLR) is directed to the feasibility of hybrid materials for aerospace applications.
The term hybrid material refers to the substitution of plies in a CFRP laminate with titanium or stainless steel. This hybrid material promises an improvement of the load carrying capacity compared to conventional CRFP materials in regions of high local load introduction, by combining the good bearing strength performance of metallic materials and damage tolerance behaviour of CFRP.

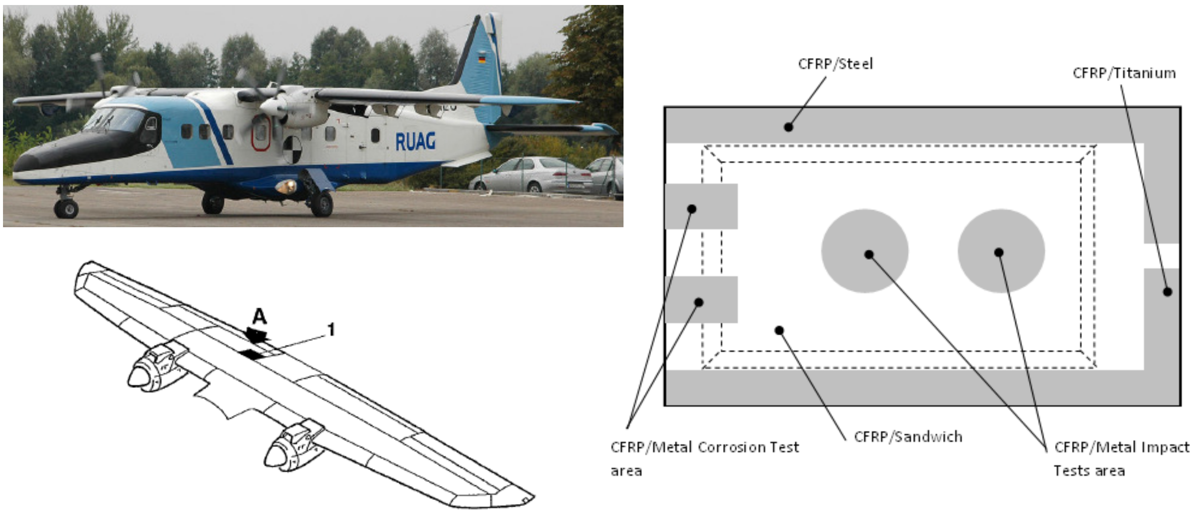

Figure 6.8: Test panel – Do228 NG

Within the research project focus is directed to the detailed study of the material properties by coupon and component testing (static and fatigue), determination of failure criteria through test and FEM simulation, implementation of simplified calculation methods, manufacturing processes and NDT/NDI methods.

As part of the testing campaign a flying test panel will be installed on the Do228 NG to study the long term behaviour and environmental effects on the hybrid material.

The runtime of the project is from 2009 to 2012. The research project HyCoS has received funding from the German Federal Ministry of Economics and Technology's LuFo-Project IV Call 2 under grant agreement no. 20W0806A.

6.6 Fundamental Science of Strength Data Unification, Modeling, Analysis, Processing, Approximation, and Estimation

L. G. Gelimson (IFS)

For strength data analysis and 2D interpreting 3D data, e.g. in aeronautical fatigue, use the principal stresses $\sigma_1 \geq \sigma_2 \geq \sigma_3$ [1, 2]. To provide stress sign unification both in technical mechanics and in geomechanics, introduce pressures [3]

$$p = - \sigma \ , \ p_1 = - \sigma_3 \ , \ p_2 = - \sigma_2 \ , \ p_3 = - \sigma_1 \ , \ p_1 \geq p_2 \geq p_3 \ .$$

Apply fundamental science of data modeling [4, 5]. Rotate coordinate system $O\sigma_1\sigma_2\sigma_3$ by the Euler angles [1, 6] of precession $\psi = \pi/4$, of nutation $\varphi = \arccos 3^{-1/2}$, and of intrinsic rotation $\theta = 0$. Rename the axes to obtain coordinate system $O\sigma_x\sigma_y\sigma_z$ whose z-axis provides $\sigma_1 = \sigma_2 = \sigma_3$ with

$$\sigma_x = 6^{-1/2}\sigma_1 + 6^{-1/2}\sigma_2 - (2/3)^{-1/2}\sigma_3 \ , \ \sigma_y = - 2^{-1/2}\sigma_1 + 2^{-1/2}\sigma_2 \ , \ \sigma_z = 3^{-1/2}\sigma_1 + 3^{-1/2}\sigma_2 + 3^{-1/2}\sigma_3 \ .$$

In any half-plane starting at this z-axis and for any strength data point $(\sigma_x , \sigma_y , \sigma_z)$ in this half-plane, introduce axis $O\sigma_m$ along $O\sigma_z$, $O\sigma_d$ with $\sigma_d = p_d = (\sigma_x^2 + \sigma_y^2)^{1/2}$, and place 2D diagram point $(\sigma_m , \sigma_d = p_d)$.

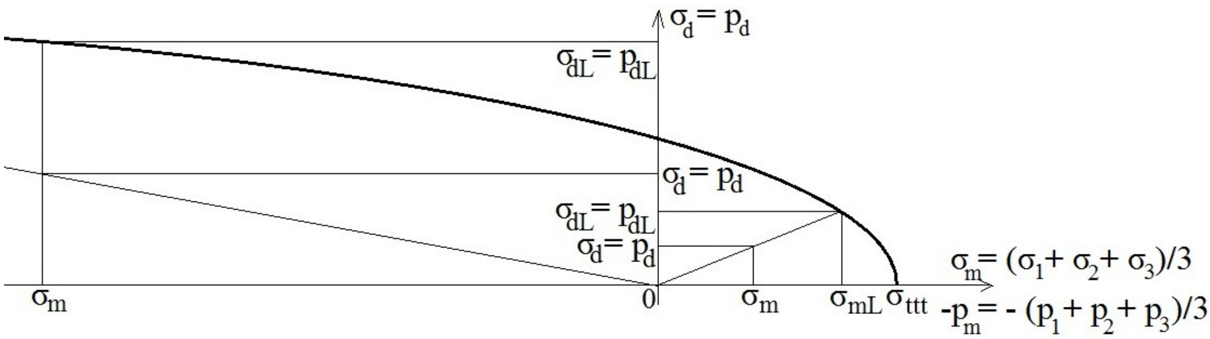

Figure 6.9

The curve in this Figure 6.9 shows the intersection of the limiting surface of a certain limiting strength criterion with this half-plane. If this limiting surface is rotationally symmetric about axis $O\sigma_z$, then the choice of this half-plane has no influence on the results and, in particular, on this diagram. By no rotational symmetry of this limiting surface, select any certain η-half-plane building angle η ($0 \leq \eta < 2\pi$) in the anticlockwise direction with axis $O\sigma_x$ and create here a unified end η-diagram:

1. For any η'-half-plane, determine η'-diagram point $[\sigma_m(\eta'), \sigma_d(\eta') = p_d(\eta')]$ for any limiting or nonlimiting η'-half-plane strength data point $[\sigma_x(\eta'), \sigma_y(\eta'), \sigma_z(\eta') = \sigma_m(\eta')]$:

$$\sigma_d(\eta') = p_d(\eta') = \{[\sigma_x(\eta')]^2 + [\sigma_y(\eta')]^2\}^{1/2} \ ,$$

limiting value $\sigma_{dL}(\eta')$ of $\sigma_d(\eta')$ either by the constant direction to (or from) the origin O if $\sigma_m(\eta') \geq 0$ or by constant value $\sigma_m(\eta')$ if $\sigma_m(\eta') \leq 0$, reserve $n(\eta') = \sigma_{dL}(\eta')/\sigma_d(\eta')$.

2. For η-half-plane and η-diagram, add (to their own η-points) remaining transformed η'-points ($\eta' \neq \eta$). Namely, take $\sigma_z(\eta) = \sigma_m(\eta) = \sigma_z(\eta') = \sigma_m(\eta')$ and $n(\eta) = n(\eta')$. To provide the last equality, first in this η'-diagram in this η'-half-plane, consequently take $\sigma_d(\eta')$, the corresponding values $\sigma_{dL}(\eta')$, and then $n(\eta')$. Secondly, consider this η-diagram in this η-half-plane, take $n(\eta) = n(\eta')$, $\sigma_z(\eta) = \sigma_m(\eta) = \sigma_z(\eta') = \sigma_m(\eta')$, then (by value $\sigma_z(\eta) = \sigma_m(\eta)$ in this η-diagram) determine $\sigma_{dL}(\eta)$, further

$\sigma_d(\eta) = p_d(\eta) = \sigma_{dL}(\eta)/n(\eta)$,

place desired **additional** η-diagram point [$\sigma_m(\eta)$, $\sigma_d(\eta) = p_d(\eta)$] and desired **additional** η-half-plane strength data point [$\sigma_d(\eta)\cos\eta$, $\sigma_d(\eta)\sin\eta$, $\sigma_z(\eta) = \sigma_m(\eta)$].
Placing all the spatial strength data points in one half-plane and in one two-dimensional diagram brings very many advantages by strength data analysis, comparing, processing, approximation, and estimation, e.g. in aeronautical fatigue.

References

[1] Filonenko-Borodich M. M. Mechanical Strength Theories. – Moscow State University Publishers, Moscow, 1961. – 92 pp. – In Russian.
[2] Gelimson L. G. Providing Helicopter Fatigue Strength: Unit loads. In: Structural Integrity of Advanced Aircraft and Life Extension for Current Fleets – Lessons Learned in 50 Years After the Comet Accidents, Proceedings of the 23rd ICAF Symposium, Dalle Donne, C. (Ed.), 2005, Hamburg, Vol. II, 589 – 600
[3] Gelimson L. G. Fundamental Science of Strength Data Unification, Modeling, Analysis, Processing, Approximation, and Estimation (Fundamentals). The "Collegium" All World Academy of Sciences Publishers, Munich (Germany), 2010
[4] Gelimson L. G. Providing Helicopter Fatigue Strength: Flight Conditions. In: Structural Integrity of Advanced Aircraft and Life Extension for Current Fleets – Lessons Learned in 50 Years After the Comet Accidents, Proceedings of the 23rd ICAF Symposium, Dalle Donne, C. (Ed.), 2005, Hamburg, Vol. II, 405-416
[5] Gelimson L. G. Fundamental Science of Data Modeling. The "Collegium" All World Academy of Sciences Publishers, Munich, 2010
[6] Encyclopaedia of Mathematics. Ed. M. Hazewinkel. Volumes 1 to 10. Kluwer Academic Publ., Dordrecht, 1988-1994

7 Fatigue and Fracture of Engine Materials

7.1 Fatigue Crack Propagation Measurements on IN718 in the Temperature and Stress Range of Dynamic Embrittlement

K. Wackermann (LMW), U. Krupp (HS Osnabrück), H.-J. Christ (LMW)

IN718 is a standard nickel-base alloy for high-temperature usage, e.g. as forged gas turbine disc or blade. At elevated temperature IN718 is prone to cracking by dynamic embrittlement which is caused by temperature- and tensile-stress-assisted oxygen grain boundary diffusion, resulting in time-dependent a loss of the grain boundary bonding. The result is fast intercrystalline crack propagation. In contrast, in vacuum or inert gas the crack propagation rate is slower and the crack morphology is ductile and transcrystalline. The crack propagation rate does not depend exclusively on the surrounding atmosphere but in air also on the dwell-time duration which is the holding time at maximum load in the fatigue cycle. Increasing dwell-time durations leads to faster crack propagation rates, cf. Figure 7.1.

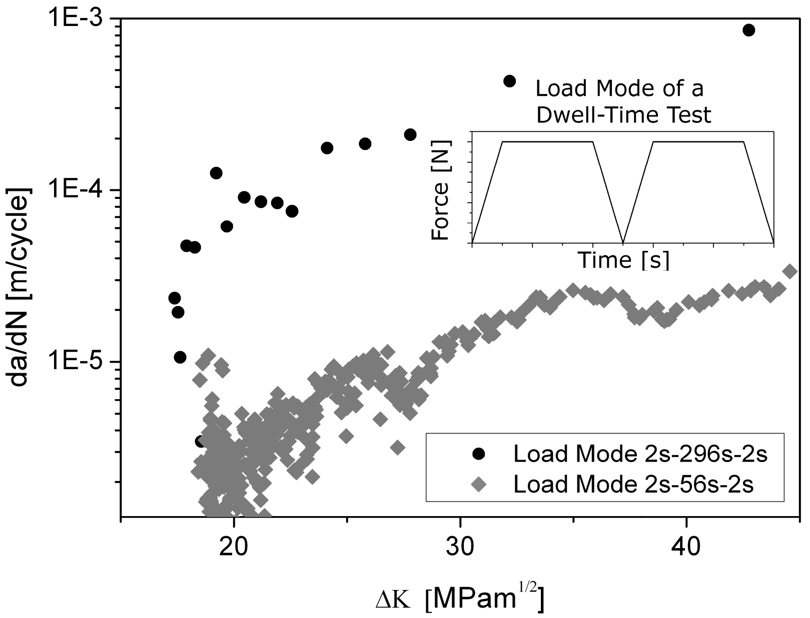

Figure 7.1 Crack propagation rates on IN718 at 650°C in laboratory air in dwell-time tests in stress-control for one load mode with 2s loading up to maximum force, 296s at maximum load and 2s to minimum load (load mode 2s-296s-2s) and one load mode with 2s loading up to maximum force, 56s at maximum load and 2s to minimum load (load mode 2s-56s-2s).

The objective of this research is a better understanding of the intercrystalline cracking phenomenon "dynamic embrittlement" by an analysis of the crack propagation behaviour and a correlation of the crack propagation with the microstructure. This shall be achieved by combined crack propagation measurements with (i) an alternate current potential drop system (ACPD) and with (ii) a Questar far-field microscope. The far-field microscope allows the observation of the crack propagation on the surface of one side of a corner-crack specimen. In contrast, the ACPD system measures the bulk crack size. The microstructure has been analyzed by scanning and transmission electron microscopy (SEM and TEM).

So far the first crack propagation tests with different dwell-time durations are performed, showing different crack propagation rates for different dwell-time durations, cf. Fig. 1.
Furthermore, the measurements of the alternate current potential drop system enable a correlation of crack growth to the three parts of a dwell-time test like loading to maximum force, holding at maximum force and unloading to minimum force. For the 2s-296s-2s load mode test shown in Fig. 1, it can be seen that there are conditions in which the main crack propagation in one loading cycle appears between two dwell-time durations. This becomes obvious by the step wise increase of crack size measurement by the alternate current potential drop, cf. Figure 7.2.

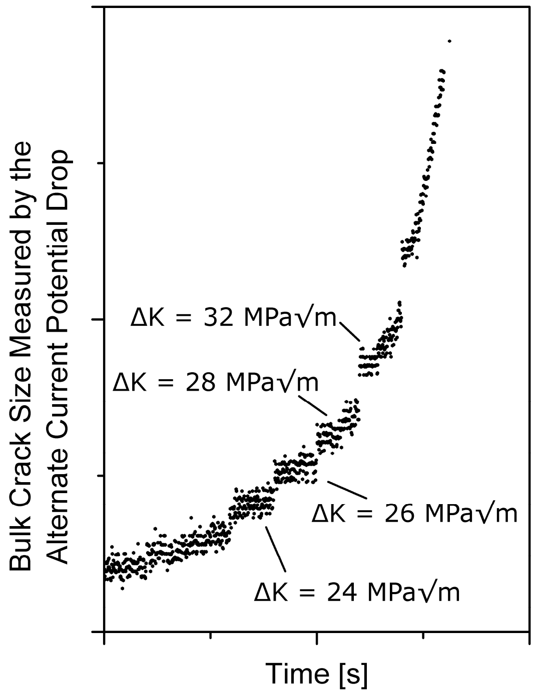

Figure 7.2 Bulk crack size v. time for a selected part of a crack propagation test in a dwell-time load mode at 650°C on IN718 with a dwell-time duration of 296 seconds at maximum load. The steps correspond exactly to the dwell-time duration of 296s for one single loading cycle, showing that for some test conditions the main crack propagation appears between two dwell-time durations.

7.2 Enhancing the fatigue properties of the metastable β Titanium alloy Ti 38-644 by obtaining a superior microstructure via duplex aging

Peter Schmidt, Ali El-Chaikh, Hans Jürgen Christ (LMW)

Highly stabilized (solute-rich) β titanium alloys are characterized by some outstanding (mechanical) properties. At low weight this alloy class can be heat-treated to a broad range of strength to ductility ratios. Excellent corrosion resistance, reasonable room temperature formability and a very good fatigue endurance (e.g. fatigue limit) make β titanium alloys attractive materials for fatigue critical components in structural aerospace applications requiring high strength and low weight at the same time (e.g. fastener, fuselage parts, etc.). In this context, the applicability range of β titanium alloys might be restricted due to their proneness to an inhomogeneous precipitation of the strengthening α phase within the β microstructure and to the formation of soft α phase layers along the β grain boundaries (see Figure 7.3). The formation of precipitate-free zones (PFZ) and grain boundary α phase (α_{GB} phase) are known to be the microstructural key features determining the fatigue life of highly stabilized β titanium alloys since monotonic and cyclic plastic deformation are concentrated on these weak regions. Extensive slip lengths for dislocations facilitated by large β grain sizes which are associated with β-annealed microstructures have to be considered in this context. Such microstructure phenomena do more and more control fatigue crack initiation as well as fatigue crack propagation with increasing yield strength of the material.

Since the β grain size is often considered to be the primary factor controlling the fatigue life of highly stabilized β titanium alloys a solution annealing usually slightly above the transition temperature T_β is recommended in order to avoid β grain coarsening. Subsequent aging in the (α+β)-regime causes a precipitation hardening effect as desired. A small β grain size and a huge driving force for α phase precipitation leads to high monotonic strength but the α phase forms directly ($\beta \rightarrow \alpha$) at preferred sites e.g. β grain boundaries or dislocation arrangements, meaning the α phase forms inhomogeneously due to the significant amount of residual work inherent the β grain boundaries. Microstructures obtained by direct aging are known to deteriorate the fatigue properties of highly stabilized β titanium alloys.

Duplex aging is a proper technique in order to establish a more homogeneous distribution of strengthening α precipitates. Pre-aging the material at low temperature enables the indirect formation of the α phase on metastable coherent particles ω and β'. In the present study a heat treatment cycle in case of the highly stabilized β titanium alloy Ti 38-644 (β-C) was developed. The results revealed clearly, that a heat treatment aiming at good fatigue properties differs strongly with respect to the solution-annealing and aging parameters, which are favourable to achieve maximum monotonic strength. Since β-C exhibits a very sensitive recrystallization and aging response upon the particular thermomechanical processing applied an individual duplex-aging cycle was designed taking the prior working history of the material into account. The results designate an optimized α precipitation based on a fully recrystallized β microstructure to be the controlling factor determining the fatigue limit of β-C titanium alloy and β grain size is considered to be less important. Therefore, β-C was completely recrystallized in the 1st heat treatment step for 30min at 920℃ leading to considerable β grain coarsening (62→120µm). Subsequently (2nd step) the alloy was pre-aged for 12hrs at 440℃ leading to intergranular formation of α precipitates based on β'-precursors according to the transformation $\beta \rightarrow \beta + \beta' \rightarrow \beta + \alpha$. In favour of sufficient ductility and at the expense of yield strength β-C was finally aged for 24hrs at a temperature of 500℃ thereby ultimately completing the hardening process. As opposed to the direct-aged microstructure, β-C neither exhibits PFZ nor α_{GB} phase formation in the duplex-aged condition as illustrated by a comparison between the corresponding Figure 7.3 (a) and (b).

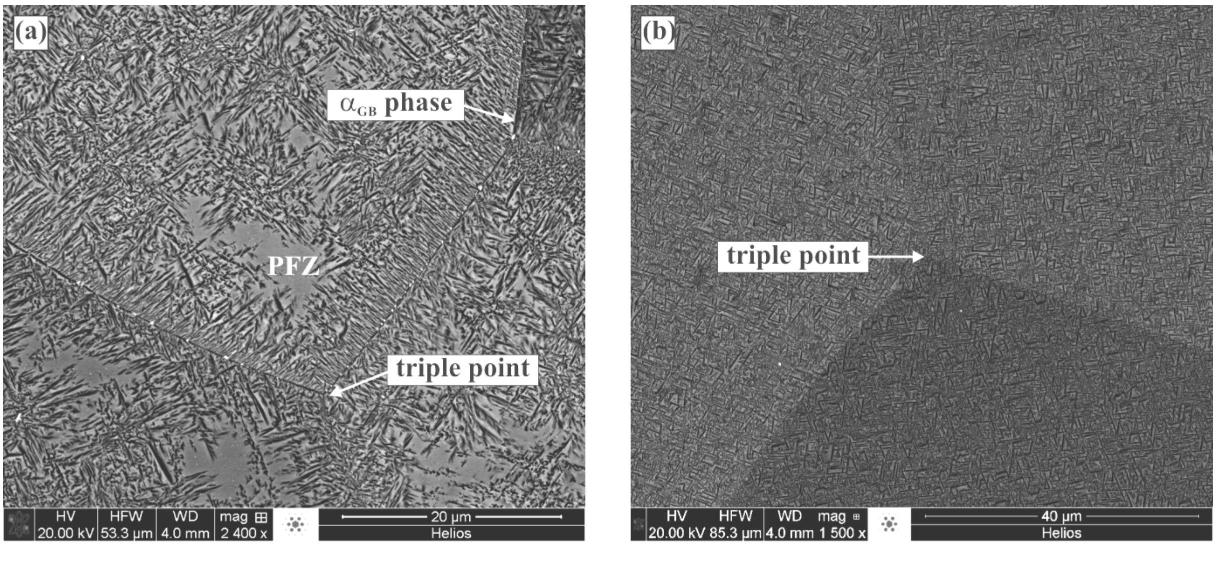

Figure 7.3 (a) Aging β-C titanium alloy to high monotonic strength leads to the formation of precipitate-free zones (PFZ) and soft α layers along the β grain boundaries (α_{GB} phase) deteriorating the fatigue properties. (b) Duplex-aging based on a fully recrystallized β microstructure clearly diminishes the negative impact of precipitate-free zones and α_{GB} phase on the fatigue endurance.

Tensile tests according to EN 10002 revealed a slightly better tensile ductility of duplex-aged β-C as compared to direct-aged conditions at identical monotonic strength and a transition towards intergranular fracture behavior. Since the fatigue limit is considered to be the most accurate parameter describing the resistance of β titanium alloys to fatigue reasonably, HCF-tests were conducted and a fatigue limit of 700MPa (745MPa) was determined under tension-compression (rotating bending) load at a limiting number of loading cycles of $N = 2 \cdot 10^6$. The values obtained are very reasonable as compared to literature data. As shown Figure 7.4, duplex-aged fatigue samples showed surface-related fatigue crack initiation while direct aging led to subsurface crack initiation sites which are related to the microstructure phenomena mentioned above.

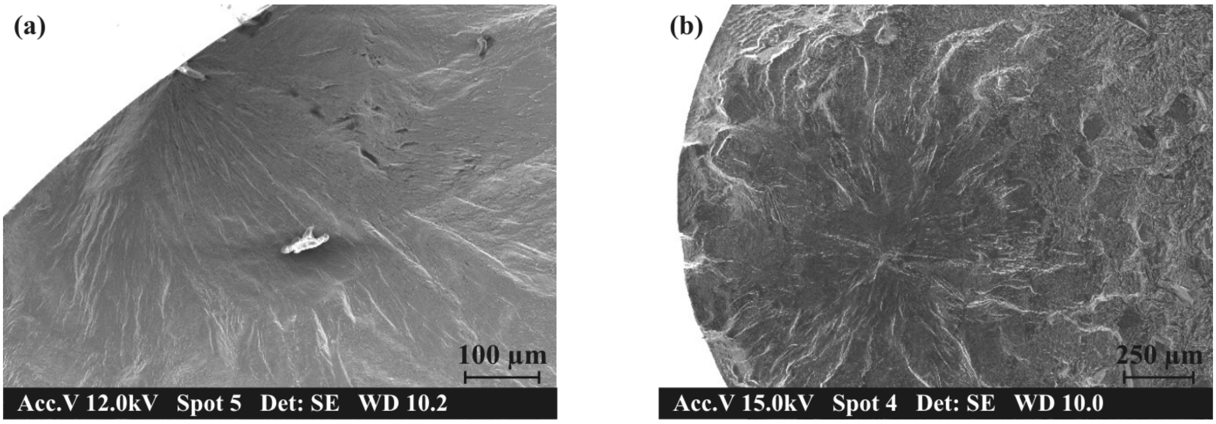

Figure 7.4 Fatigue crack nucleation sites in tension-compression fatigue samples: (a) surface-related in duplex-aged β-C, (b) subsurface crack nucleation in β-C directly aged to high monotonic strength.

Long crack propagation was studied according to ASTM E-647 (R=0.1) and the results revealed a slightly better fatigue crack growth behavior of the duplex-aged (ΔK_{th}: 2.9–3.3MPa$\sqrt{m}$) as compared to the direct-aged material (ΔK_{th}: 2.3–2.7MPa$\sqrt{m}$) at comparable yield strength, suggesting the α_{GB} phase to exert the most deteriorating effect not only on tensile ductility but also on the resistance of β-C to fatigue crack growth behaviour.

7.3 High-Temperature Low Cycle Fatigue Capability of Titanium Aluminides

Thomas K. Heckel, Ali El-Chaikh, Hans Jürgen Christ (LMW)

In recent times, γ-TiAl-based alloys have found large-scale implementation as blade material into advanced aero engines, substituting heavy-weight nickel-based alloys. A remaining crucial issue is however to assess the material's maximum reliable fatigue performance under operating conditions (i.e. guaranteeing a minimum LCF life of 10,000 cycles). Investigations conducted at the authors' institution have revealed that the high-temperature low cycle fatigue behaviour of the advanced γ-TiAl-based alloy TNB-V2, containing 8 at.-% niobium, is rather modest at an applied total strain amplitude of $\Delta\varepsilon/2$ = 0.7% under fully-reversed testing conditions. In the temperature field between room temperature and 850°C, fatigue life never exceeded 600 cycles.

Intermetallic alloys are quite brittle below their respective brittle-to-ductile transition temperatures, which can be found at approximately 800°C for TNB-V2, and in the case of γ-TiAl-based alloys engineering applications are basically limited to below this temperature since the material looses its beneficial creep properties above the transition. Therefore, a threshold value has been developed for providing a "safe" LCF life (TK Heckel, H-J Christ, *Advanced Engineering Materials* 12 (2010) 1142). This value limits the maximum strain amplitude to $\Delta\varepsilon/2$ = 0.35% in the entire intended operating temperature field (i.e. up to 750℃). The value corresponds to a stress amplitude of approximately $\Delta\sigma/2$ = 500 MPa.

Recent results on the LCF behaviour of TNB-V2 at lower strain amplitudes confirm the suggested threshold concept. In Figure 7.5a the LCF life versus temperature is plotted for the two strain amplitudes of 0.6 and 0.7%. A significant increase in fatigue life can be observed, reducing the strain from 0.7 to 0.6%. The different fatigue performance can be correlated with the amount of plastic strain amplitude. The values of plastic strain amplitude shown in Figure 7.5 have been calculated from Ramberg-Osgood parameters that are available in the above-cited reference. It is evident from Figure 7.5 b that the amount of plastic strain amplitude almost doubles between total strain amplitudes from 0.6 to 0.7%.

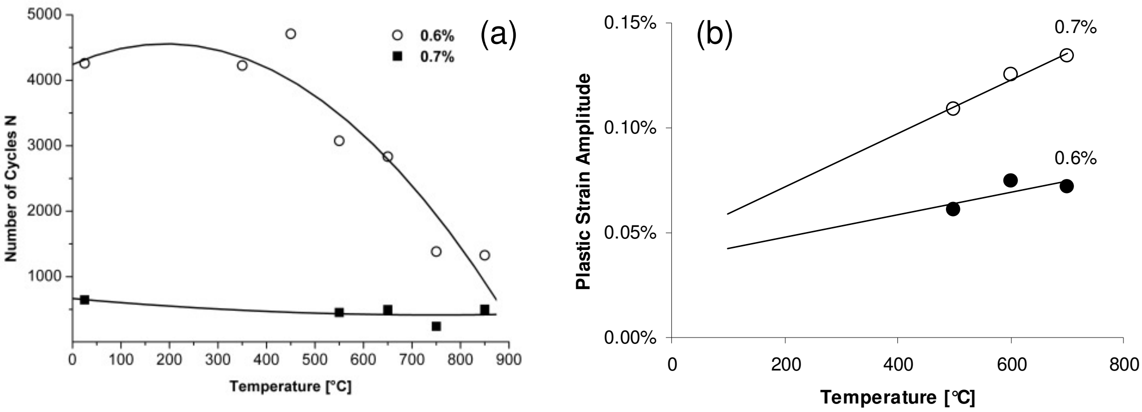

Figure 7.5 a) cycles to failure, and b) calculated plastic strain amplitude for two strain amplitudes vs. temperature.

7.4 Fatigue Investigations and Numerical Modelling of Forged Ti6Al4V in Different Microstructural Conditions

Helge Knobbe (LMW), Philipp Köster (IMR), Hans-Jürgen Christ (LMW), Claus-Peter Fritzen (IMR), Martin Riedler (Böhler)

Two different types of microstructure were investigated with respect to fatigue crack initiation and short crack growth characteristics. Both microstructures were of bi-modal nature. The first one was forged followed by a stress relieving annealing leading to a very fine microstructure with partly deformed primary alpha grains. The second one was forged as well followed by a solution heat treatment leading to an almost fully recrystallized microstructure with a higher secondary alpha colony size. Wöhler-type experiments, followed by interrupted fatigue tests were carried out using a servohydraulic test facility. Different stress levels were imposed at a constant R ratio of -1 and a frequency of 20Hz with a sinusoidal command signal. SEM together with the EBSD technique was applied for the crack observation as well as for the determination of local crystallographic orientations, in order to link crack paths and propagation rates to microstructural features. FIB technique was applied to selected secondary cracks to obtain a detailed analysis of the crack path in the depth. It was found that most of the cracks initiate on boundaries between two lamellae or between primary alpha grains and a lamella. FIB analysis revealed a strong influence of the phase boundaries, i.e. the remaining beta phase. Cracks are dominated by following favourably oriented boundaries in terms of the burgers relation. These cracks propagate rather fast on glide planes with high Schmid factors until they reach another phase boundary. In primary alpha grains prismatic or basal slip systems are activated. Crack deflection is also a common feature, and is probably related to high tilt and twist angles between the grains involved. The crack propagation and initiation mechanisms were the same for both microstructures, but the finer microstructure has higher fatigue strengths according to the Hall-Petch relation. Based on these experimental investigations a two-dimensional model for stage I-crack propagation is developed, which accounts for crack propagation on slip planes as well as grain boundaries. The model considers the barrier effect of grain boundaries and is solved numerically by dislocation dipole boundary elements. The verification of the model was achieved by calculating crack growth rates of cracks that were found experimentally in the microstructure (see Figure 7.6).

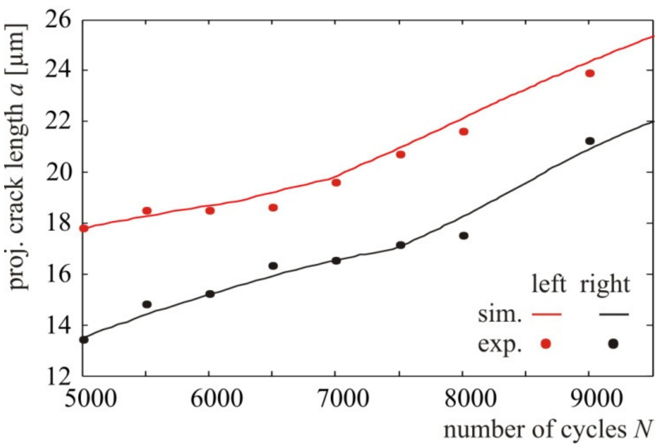

Figure 7.6 Comparison of crack growth between simulation and experiment

8 Non-Destructive Testing

8.1 Performance of Non Destructive Inspections on Example of a320 NEF2 & NEF3 Structural Fatigue Tests

J. Bolten (IABGmbH)

The increased efficiency requirements for the performance of structural fatigue tests has placed an increasing demand to reduce costs while ensuring the requirements of the customer as e.g. quality and time targets. Aim of the performed inspections on the structural fatigue tests Airbus A320 NEF2 & NEF3 was to achieve a high efficiency while ensuring the required quality without exceeding the designated time frame. In order to meet these targets an efficient inspection process has been created and advanced inspection equipment was used.

Inspection process

The inspection to be performed on A320 NEF2 & NEF3 were subdivided into daily inspections and larger inspection stops (2 – 3 days) whereby general visual, detailed visual and special detailed inspections using NDT methods like ultrasonic, eddy current, x-ray etc. have been executed. Basing on the inspection program provided by Airbus, jobcards have been created and bundled per inspection zone and NDT method before each inspection stop. The idea behind the bundling was to hand out a pack of jobcards to each inspector in order to reduce efforts like calibration of the NDT equipment, walk to the inspection area etc. Finally, this procedure led to an increased efficiency during the inspections.

In conjunction with the inspections it was necessary to provide access to some inspection areas whereas man hole covers, floor panels etc. had to be removed. In order to avoid unnecessary interruption of the inspection process, the strong coordination of the removals and the hand out of jobcards for these areas was another essential issue to perform efficient inspections.

Another important issue for efficient inspections was the use of an electronic inspection data base provided by Airbus which increased the inspection efficiency in case of inspection preparation, inspection results recording and approval and monitoring of the inspection.

Advanced inspection equipment

In addition to the commonly known state of the art NDT equipment, advanced NDT instruments basing on ultrasonic and eddy current technologies have been used within the inspections of A320 NEF2 & NEF3 in order to increase the efficiency and quality.

The eddy current testing instrument uses 4 adjustable frequencies for hand-, scan- and dynamic- testing. For the A320 NEF2 & NEF3 tests it has been used for bore hole and lap joint inspections. In case of the bore hole inspections the instrument offered the possibility to determine the crack length in the different layers and used a C-Scan visualization. For the lap joint inspection the usage of 4 different frequencies allowed different penetration depths and eased the signal evaluation. Combined with an initially performed base line inspection of the joints the quality of such inspections and the test speed could be increased in comparison to conventional joint inspections with eddy current.

For rivet row inspections an ultrasonic phased array instrument with an automatically varying sound beam has been used. Combined with the visualisation by an S-Scan the quality of such inspections and the test speed could be increased in comparison to conventional rivet row inspections using single element search units.

a.)

b.)
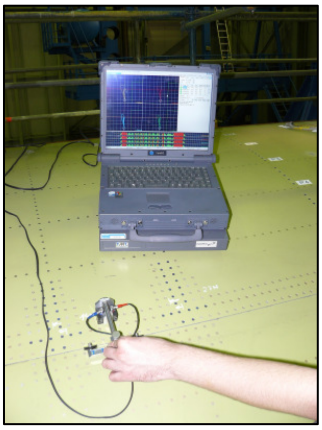
c.)


Figure 8.1 a.) 4 Frequency EC instrument for bore hole inspection, b.) 4 Frequency EC instrument for lap joint, c.) 4 Frequency UT phased array instrument rivet row inspection

In addition to the manual NDT equipment, a structural health monitoring (SHM) technology known as comparative vacuum monitoring (CVM) technique has been used to monitor a local area which had to be inspected daily and was hidden by big belly fairings. The usage of the

CVM technique avoided the daily removal of the belly fairings which had to be performed normally by 2 workers and saved 4 man hours per day, therefore.

8.2 Signed Geometric and Quadratic Mean Theories in Fundamental Sciences of Estimation, Approximation, and Data Processing

L. G. Gelimson (IFS)

To solving contradictory (e.g. overdetermined) problems in approximation and data processing, the least square method (LSM) [1] by Legendre and Gauss only usually applies. Overmathematics [2, 3] and fundamental sciences of approximation and data processing [4] have discovered a lot of principal shortcomings [2-5] of the LSM. Additionally, its errors increase with data scatter and approximation declination.
In these sciences, signed geometric and quadratic mean theories (SGQMT) are valid by coordinate system linear transformation invariance of the given data.

In the 2D case, centralize n ($n \in N+ = \{1, 2, ...\}$, $n > 2$) points [j=1n (x'j , y'j)] with any real

coordinates via $x = x' - \Sigma_{j=1}^{n} x'_j / n$, $y = y' - \Sigma_{j=1}^{n} y'_j / n$. Normalize x , y , y = ax via
$X = x/(\Sigma_{j=1}^{n} x_j^2)^{1/2}$, $Y = y/(\Sigma_{j=1}^{n} y_j^2)^{1/2}$, $A = (\Sigma_{j=1}^{n} x_j^2 / \Sigma_{j=1}^{n} y_j^2)^{1/2} a$.

Fit points $[_{j=1}^{n} (X_j , Y_j)]$ with a straight line Y = AX via minimizing the sum of the squared differences of their Y-coordinates and X-coordinates by $a \neq 0$ and $A \neq 0$:

$^2{}_{YX}S(A) = \Sigma_{j=1}^{n}[(AX_j - Y_j)^2 + (Y_j/A - X_j)^2]$, $(A^2 - 1)(A^2 - \Sigma_{j=1}^{n} X_jY_j A + 1) = 0$,
$A = (A_xA_y)^{1/2} \operatorname{sign} \Sigma_{j=1}^{n} x_jy_j = (\Sigma_{j=1}^{n} y_j^2 / \Sigma_{j=1}^{n} x_j^2)^{1/2} \operatorname{sign} \Sigma_{j=1}^{n} x_jy_j$,
$y = \operatorname{sign} \Sigma_{j=1}^{n} x_jy_j (\Sigma_{j=1}^{n} y_j^2 / \Sigma_{j=1}^{n} x_j^2)^{1/2} x$.

The 3D case with n > 3 points $[_{j=1}^{n} (x'_j , y'_j , z'_j)]$, centralization transformation $x = x' - \Sigma_{j=1}^{n} x'_j / n$, $y = y' - \Sigma_{j=1}^{n} y'_j / n$, $z = z' - \Sigma_{j=1}^{n} z'_j / n$, and a plane ax + by + cz = 0 gives

$z = \operatorname{sign}(\Sigma_{j=1}^{n} x_jz_j \Sigma_{j=1}^{n} y_j^2 - \Sigma_{j=1}^{n} x_jy_j \Sigma_{j=1}^{n} y_jz_j) \{[\Sigma_{j=1}^{n} y_j^2 \Sigma_{j=1}^{n} z_j^2 - (\Sigma_{j=1}^{n} y_jz_j)^2]/[\Sigma_{j=1}^{n} x_j^2 \times \Sigma_{j=1}^{n} y_j^2 - (\Sigma_{j=1}^{n} x_jy_j)^2]\}^{1/2} x + \operatorname{sign}(\Sigma_{j=1}^{n} x_j^2 \Sigma_{j=1}^{n} y_jz_j - \Sigma_{j=1}^{n} x_jy_j \Sigma_{j=1}^{n} x_jz_j) \{[\Sigma_{j=1}^{n} x_j^2 \Sigma_{j=1}^{n} z_j^2 - (\Sigma_{j=1}^{n} x_jz_j)^2]/[\Sigma_{j=1}^{n} x_j^2 \Sigma_{j=1}^{n} y_j^2 - (\Sigma_{j=1}^{n} x_jy_j)^2]\}^{1/2} y$.

Define and determine measures $S_L = [^2S_{min}(A) / {}^2S_{max}(A)]^{1/2}$ of data scatter and $T_L = 1 - S_L$ of data trend with respect to linear approximation. Also by nonlinearity, $S \leq S_L$. Unlike the LSM, SGQMT provide best linear approximation to the given data, e.g. in numeric tests, see Figure 8.2; Figure 8.3 with replacing (x’, y’) via (x, y):

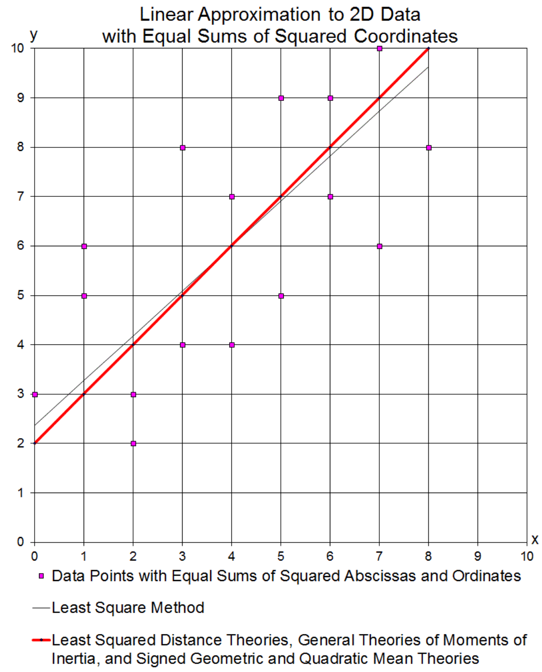

Figure 8.2 S_L **= 0.444.** T_L **= 0.556**

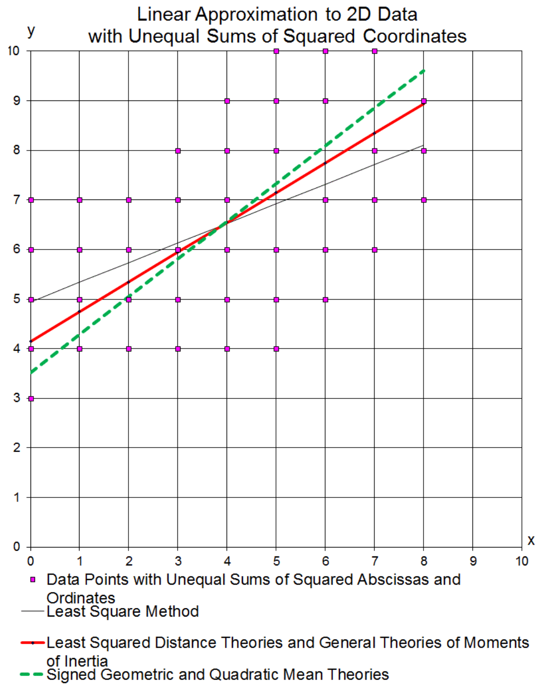

Figure 8.3 S_L**=0.53 (LSDT), 0.56 (SGQMT)**

Nota bene: By linear approximation, the results of least squared distance theories (LSDT) and general theories of moments of inertia (GTMI) [4] coincide. By $\Sigma_{j=1}^{n} y_j^2 = \Sigma_{j=1}^{n} x_j^2$ (and the best linear approximation $y = \pm x + C$), the same also holds for SGQMT. Here $y = x + 2$ (Figure 8.2). By $\Sigma_{j=1}^{n} y_j^2 \neq \Sigma_{j=1}^{n} x_j^2$, SGQMT give other results than LSDT and GTMI (Figure 8.3). But SGQMT are valid by another invariance type than LSDT and GTMI. SGQMT are very efficient in data estimation, approximation, and processing and reliable even by great data scatter, e.g. in aeronautical fatigue.

Acknowledgements

to Anatolij Gelimson for our constructive discussions on coordinate system transformation invariances and his very useful remarks.

References

[1] Encyclopaedia of Mathematics. Ed. M. Hazewinkel. Volumes 1 to 10. Kluwer Academic Publ., Dordrecht, 1988-1994
[2] Gelimson L. G. Providing Helicopter Fatigue Strength: Flight Conditions. In: Structural Integrity of Advanced Aircraft and Life Extension for Current Fleets – Lessons Learned in 50 Years After the Comet Accidents, Proceedings of the 23rd ICAF Symposium, Dalle Donne, C. (Ed.), 2005, Hamburg, Vol. II, 405-416
[3] Gelimson L. G. Overmathematics: Fundamental Principles, Theories, Methods, and Laws of Science. The "Collegium" All World Academy of Sciences Publishers, Munich, 2010
[4] Gelimson L. G. Fundamental Sciences of Approximation and Data Processing. The "Collegium" All World Academy of Sciences Publishers, Munich, 2010
[5] Gelimson L. G. Corrections and Generalizations of the Least Square Method. In: Review of Aeronautical Fatigue Investigations in Germany during the Period May 2007 to April 2009,

Ed. Dr. Claudio Dalle Donne, Pascal Vermeer, CTO/IW/MS-2009-076 Technical Report, International Committee on Aeronautical Fatigue, ICAF 2009, EADS Innovation Works Germany, 2009, 59-60

8.3 General Theories of Moments of Inertia in Fundamental Sciences of Estimation, Approximation, and Data Processing

L. G. Gelimson (IFS)

Area moments of inertia [1] apply to 2D continual sections in bending and torsion, whereas volume and mass moments of inertia [2] to rotating 3D continual objects.
General (also nonlinear) theories of moments of inertia (GTMI) in overmathematics [3, 4] and fundamental sciences of estimation, approximation, and data processing [5] apply to discrete and continual objects by coordinate system rotation invariance.
First, following the principle of tolerable simplicity [3-5], apply namely linear theories.

Linearly fit given n ($n \in N+ = \{1, 2, ...\}$, $n > 2$) 2D points [j=1n (x'j , y'j)] =$\{(x'1 , y'1), (x'2 , y'2), ... , (x'_n , y'_n)]$

with any real coordinates in a coordinate system x'O'y'. Statical moments $S_{y'} = \Sigma_{j=1}^n x'_j$ about the y'-axis and $S_{x'} = \Sigma_{j=1}^n y'_j$ about the x'-axis allow determining the data center $x'_c = S_{y'} / n$, $y'_c = S_{x'} / n$. Centralize the given data via $x = x' - x'_c$, $y = y' - y'_c$. In central coordinate system xOy , S_y and S_x vanish, whereas moments of inertia are $J_{yy} = \Sigma_{j=1}^n x_j^2$, $J_{yx} = \Sigma_{j=1}^n x_j y_j$, and $J_{xx} = \Sigma_{j=1}^n y_j^2$. Rotate xOy about its origin O by angles $\alpha_{1,2} = \arctan\{\{J_{xx} - J_{yy} \pm [4J_{yx}^2 + (J_{yy} - J_{xx})^2]^{1/2}\}/2/J_{yx}\}$ (positive in the anticlockwise direction). Obtained principal central coordinate system XOY provides vanishing J_{YX} and extremum values J_{XX} of J_{xx} and J_{YY} of J_{yy} , namely

$$J_{max} = (J_{xx} + J_{yy})/2 + [(J_{xx} - J_{yy})^2/4 + J_{yx}^2]^{1/2} , \quad J_{min} = (J_{xx} + J_{yy})/2 - [(J_{xx} - J_{yy})^2/4 + J_{yx}^2]^{1/2}$$

in principal central directions OX and OY, or vice versa. Such XOY always exists and is arbitrary by $J_{min} = J_{max}$ and unique by $J_{min} \neq J_{max}$. The 3D linear case brings similar results for solution existence and uniqueness due to the spectral theorem [6].
Define and determine measures $S_L = (J_{min} / J_{max})^{1/2}$ of data scatter and $T_L = 1 - S_L = 1 - (J_{min} / J_{max})^{1/2}$ of data trend with respect to linear approximation. Also by nonlinearity, $S \leq S_L$ and $T \geq T_L$. Unlike the LSM, GTMI provide best linear approximation to the given data, e.g. in numeric tests, see Figure 8.4 - Figure 8.5 with replacing (x', y') via (x , y):

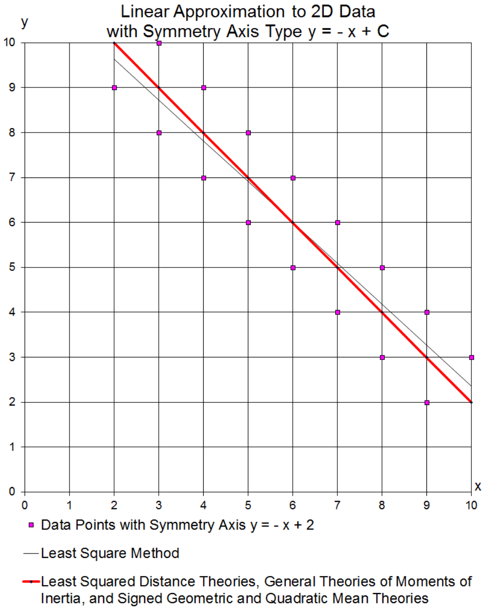

Figure 8.4S_L = 0.218. T_L = 0.782

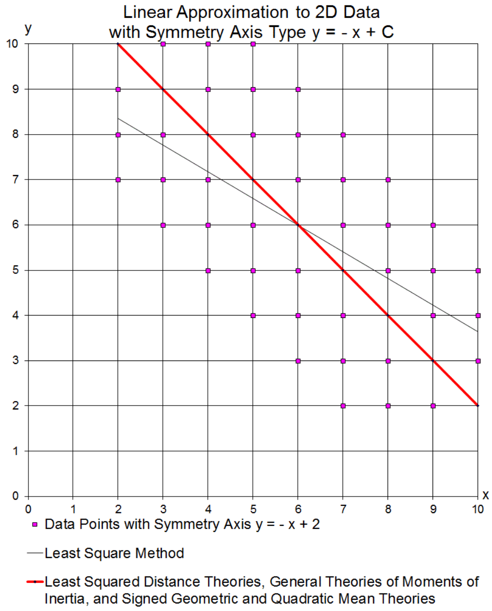

Figure 8.5 S_L = 0.507. T_L = 0.493

If necessary, use piecewise linear and further nonlinear theories of moments of inertia with respect to curvilinear axes, surfaces, etc. They bring deep theoretical fundamentals for data estimation, approximation, and processing, namely as applied to the problems of the existence and uniqueness of solutions, whereas least squared distance theories give more suitable explicit formulae, e.g. in aeronautical fatigue.

References

[1] Pisarenko G., Yakovlev A., Matveev V. Aide-memoire de resistance des materiaux. Mir, Moscou, 1985

[2] Gelimson L. G. Discretization Errors by Determining Area, Volume, and Mass Moments of Inertia. In: Review of Aeronautical Fatigue Investigations in Germany During the Period May 2005 to April 2007, Ed. Dr. Claudio Dalle Donne, Pascal Vermeer, CTO/IW/MS-2007-042 Technical Report, Aeronautical fatigue, ICAF2007, EADS Innovation Works Germany, 2007, 20-22

[3] Gelimson L. G. Providing Helicopter Fatigue Strength: Flight Conditions. In: Structural Integrity of Advanced Aircraft and Life Extension for Current Fleets – Lessons Learned in 50 Years After the Comet Accidents, Proceedings of the 23rd ICAF Symposium, Dalle Donne, C. (Ed.), 2005, Hamburg, Vol. II, 405-416

[4] Gelimson L. G. Overmathematics: Fundamental Principles, Theories, Methods, and Laws of Science. The ”Collegium” All World Academy of Sciences Publishers, Munich, 2010

[5] Gelimson L. G. Fundamental Sciences of Estimation, Approximation, and Data Processing. The ”Collegium” All World Academy of Sciences Publishers, Munich, 2010

[6] Encyclopaedia of Mathematics. Ed. M. Hazewinkel. Volumes 1 to 10. Kluwer Academic Publ., Dordrecht, 1988-1994

8.4 Group Center Theories in Fundamental Sciences of Estimation, Approximation, Data Modeling and Processing

L. G. Gelimson (IFS)

Along with great data scatter, there can be outliers usually ignored with losing valuable information on the directions of outlier deviation from the remaining data.
Group center theories (GCT) in overmathematics [1, 2] and fundamental sciences of estimation, approximation, and data processing [3] locally represent each data point group with its center whose quantity equals the number of the points in this group.

Let xi (i = 1, 2, ... , m , m ∈ N+ = {1, 2, ...}) be the ith coordinate, xij the ith coordinate of the jth data point quantielement [1, 2] (j = 1, 2, ... , n , n ∈ N+) of a group of data points quantielements, and q_j the quantity of the element in this quantielement. Replace this group with its weighted central data point quantielement whose ith coordinate is $x_i = \Sigma_{j=1}{}^n q_j x_{ij} / \Sigma_{j=1}{}^n q_j$ and quantity $q = \Sigma_{j=1}{}^n q_j$. Use either least squared distance theories (LSDT) and general theories of moments of inertia (GTMI) by rotation invariance or signed geometric and quadratic mean theories (SGQMT) [3] by linear transformation invariance along with centralizing the given data to determine their principal directions, scatter and trend measures. Compare such results for the total data and almost all (at least about 90 %) of them without outlier candidates. Replace outliers groups whose centers are appropriate (lying among the remaining data) with these centers whose quantities are the numbers of group data points. In the following numeric test, 3 outliers (Figure 8.6) are replaced and shown separately as adjacent points (Figure 8.7) along with data scatter measures S_L and $S_{TrialQuadratic}$.

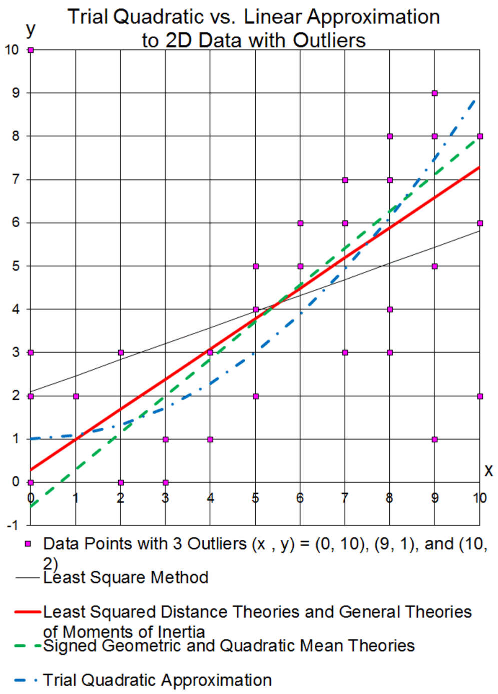

Figure 8.6 S_L=0.61 (LSDT), 0.63 (SGQMT)

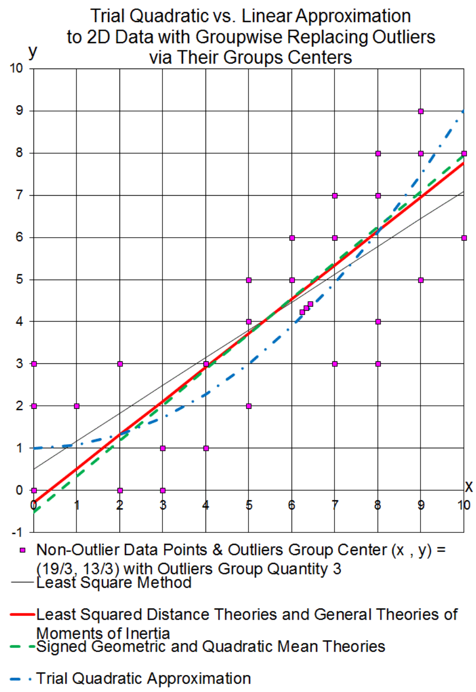

Figure 8.7 S_L = 0.35, $S_{TrialQuadratic}$ = 0.29

Nota bene: Simply ignoring the outliers gives here S_L = 0.34 (LSDT & GTMI), 0.35 (SGQMT) and best linear approximation y = 0.81x - 0.27 (LSDT & GTMI), y = 0.85x - 0.47 (SGQMT) instead of y = 0.81x - 0.30 (LSDT & GTMI), y = 0.84x - 0.51 (SGQMT) by groupwise centralizing

the outliers. Hence there is no necessity to ignore them. These both approaches make such results via LSDT & GTMI and SGQMT much nearer to one another. Due to overmathematics [1, 2], any point, e.g. an outlier, can be regarded as a quantiset of its parts (quantielements), the sum of their quantities being 1, to be included into appropriate groups. Also the remaining data points can be similarly groupwise (e.g. by moving along the coordinate axes, linear or nonlinear approximation graph) replaced via their quantified centers with comparing the results of distinct approaches to building data points groups. Groupwise compensating differently directed data errors can cardinally reduce initially great data scatter.
Group center theories can adequately consider outliers influence without losing any information and are very efficient in data modeling, estimation, approximation, and processing and reliable even by great data scatter, e.g. in aeronautical fatigue.

References

[1] Gelimson L. G. Providing Helicopter Fatigue Strength: Flight Conditions. In: Structural Integrity of Advanced Aircraft and Life Extension for Current Fleets – Lessons Learned in 50 Years After the Comet Accidents, Proceedings of the 23rd ICAF Symposium, Dalle Donne, C. (Ed.), 2005, Hamburg, Vol. II, 405-416
[2] Gelimson L. G. Overmathematics: Fundamental Principles, Theories, Methods, and Laws of Science. The "Collegium" All World Academy of Sciences Publishers, Munich, 2010
[3] Gelimson L. G. Fundamental Sciences of Estimation, Approximation, Data Modeling and Processing. The "Collegium" All World Academy of Sciences Publishers, Munich, 2010
[4] Encyclopaedia of Mathematics. Ed. M. Hazewinkel. Volumes 1 to 10. Kluwer Academic Publ., Dordrecht, 1988-1994

8.5 Coordinate Partition Theories in Fundamental Sciences of Estimation, Approximation, Data Modeling and Processing

L. G. Gelimson (IFS)

Group center theories (GCT) in overmathematics [1, 2] can cardinally reduce initially great data scatter due to groupwise compensating differently directed data errors. Appropriate data point groups are replaced with their centers whose quantities are the numbers of data points in these groups. It is very natural to build such groups of data points with near values of their coordinates separately using coordinate axes partitions like stationwise discretizing aircraft by determining its gravity center, principal axes and planes, as well as statical moments and moments of inertia [3].
Coordinate partition theories (CPT) in fundamental sciences of estimation, approximation, data modeling and processing [4] locally consider each coordinate axis separately, divide it in appropriate parts, select data points whose values of this coordinate belong to one of these parts, and unite these data points in a group. Then apply GCT to this group and replace it with its quantified data center. Compare results for all coordinate axes. Use either least squared distance theories (LSDT) and general theories of moments of inertia (GTMI) [4] by rotation invariance or signed geometric and quadratic mean theories (SGQMT) [4] by linear transformation invariance along with global data centralization to determine their principal directions, scatter and trend measures. Preliminarily replace outliers groups via GCT.
In the following numeric test (Figure 8.8, Figure 8.9), along with data point group centers and linear and nonlinear approximations to them, or their bisectors, initial data points including outliers are also shown, as well as data scatter measures S_L .

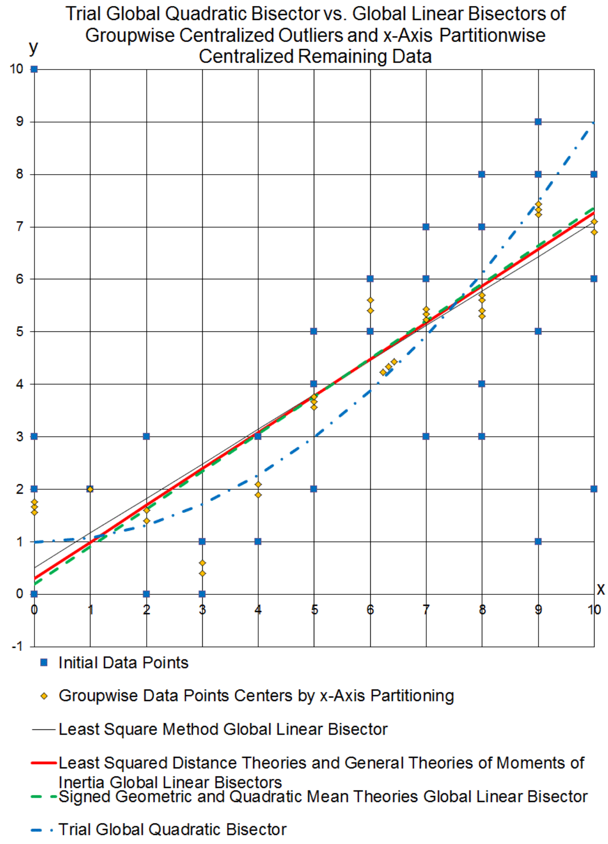

Figure 8.8 S_L=0.19 (LSDT), 0.21 (SGQMT)

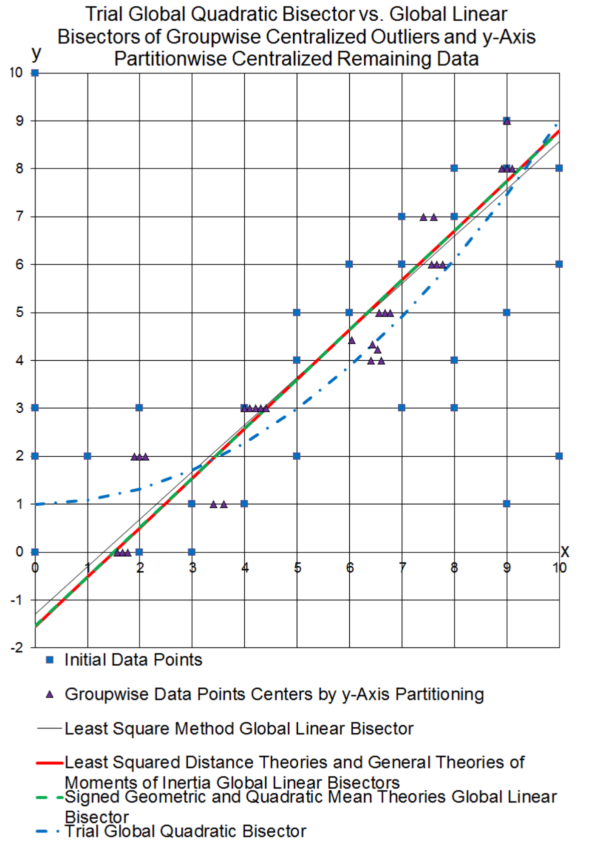

Figure 8.9 Figure 2. S_L = 0.15 (LSDT & SGQMT)

Nota bene: This straightforward approach to building data point groups so drastically reduces data scatter that LSDT & GTMI and SGQMT give almost coinciding global linear bisectors. All the more, by such small data scatter, even the least square method leads to sufficiently adequate results. Comparing all these global linear bisectors with those for the initial data shows that building the arithmetic and other mean values of the results for different axes provides still better fitting the given data. It is also useful to unite data point group centers for different axes and to rotate them.
CPT are very efficient in data modeling, estimation, approximation, and processing and reliable even by great data scatter, e.g. in aeronautical fatigue.

References

[1] Gelimson L. G. Providing Helicopter Fatigue Strength: Flight Conditions. In: Structural Integrity of Advanced Aircraft and Life Extension for Current Fleets – Lessons Learned in 50 Years After the Comet Accidents, Proceedings of the 23rd ICAF Symposium, Dalle Donne, C. (Ed.), 2005, Hamburg, Vol. II, 405-416

[2] Gelimson L. G. Overmathematics: Fundamental Principles, Theories, Methods, and Laws of Science. The "Collegium" All World Academy of Sciences Publishers, Munich, 2010

[3] Gelimson L. G. Discretization Errors by Determining Area, Volume, and Mass Moments of Inertia. In: Review of Aeronautical Fatigue Investigations in Germany During the Period May 2005 to April 2007, Ed. Dr. Claudio Dalle Donne, Pascal Vermeer, CTO/IW/MS-2007-042 Technical Report, Aeronautical fatigue, ICAF2007, EADS Innovation Works Germany, 2007, 20-22

[4] Gelimson L. G. Fundamental Sciences of Estimation, Approximation, Data Modeling and Processing. The ”Collegium” All World Academy of Sciences Publishers, Munich, 2010
[5] Encyclopaedia of Mathematics. Ed. M. Hazewinkel. Volumes 1 to 10. Kluwer Academic Publ., Dordrecht, 1988-1994

8.6 Principal Bisector Partition Theories in Fundamental Sciences of Estimation, Approximation, Data Modeling and Processing

L. G. Gelimson (IFS)

Group center theories (GCT) in overmathematics [1, 2] and fundamental sciences of estimation, approximation, data modeling and processing [3] can cardinally reduce initially great data scatter due to groupwise compensating differently directed data errors. Appropriate data point groups are replaced with their centers whose quantities are the numbers of data points in these groups. Coordinate partition theories (CPT) in these sciences build such groups of data points with near values of their coordinates.
In the simplest linear case by rotation invariance, principal bisector partition theories (PBPT) in these sciences apply CPT to the principal central coordinate system built with using the best linear approximation via least squared distance theories (LSDT) and general theories of moments of inertia (GTMI) [3, 4] to the given data, or their global linear bisector. Namely, divide its segment containing all the projections of the given data on this bisector in appropriate parts, select data points whose projections belong to one of these parts, and unite these data points in a group. Then apply GCT to this group and replace it with its quantified data center. Compare results for different partitions of this bisector, as well as the bisectors of data parts. By linear transformation invariance, use signed geometric and quadratic mean theories (SGQMT) [3] along with centralizing the global data to determine their principal directions, scatter and trend measures. Preliminarily replace outliers groups via GCT.
In the following numeric tests of PBPT (Figure 8.10) and CPT (Figure 8.11), data point group centers, linear and quadratic approximations to them, or their bisectors, and initial data points including outliers are shown, as well as data scatter measures S_L.

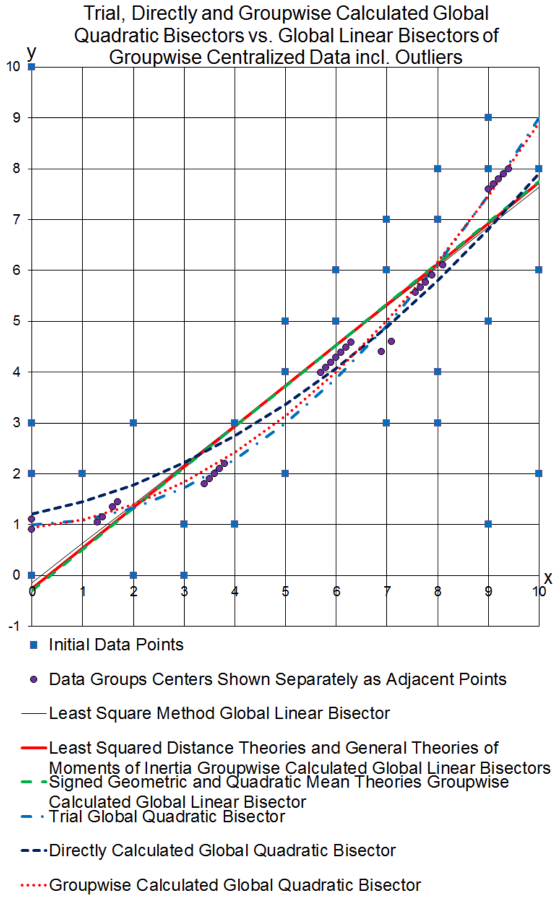

Figure 8.10 S_L=0.12 (LSDT), 0.13 (SGQMT)

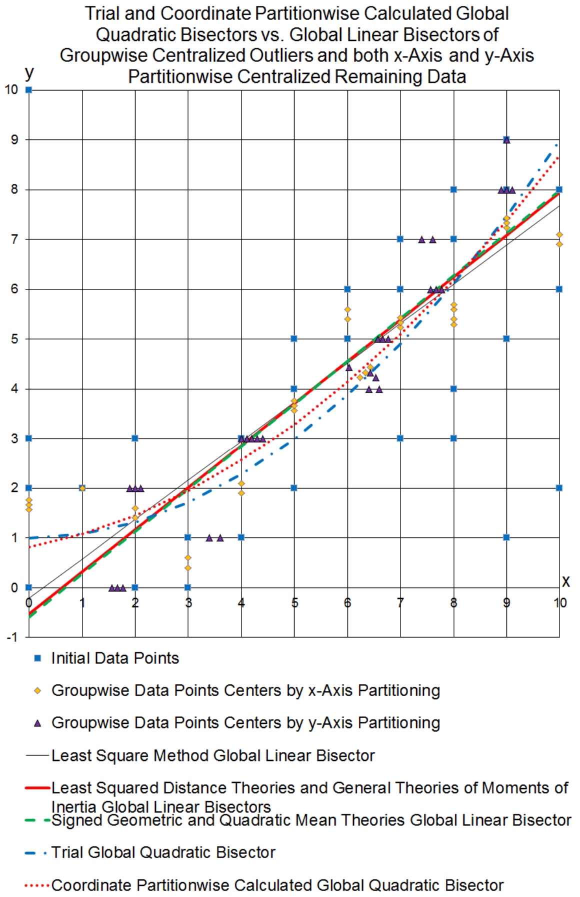

Figure 8.11 S_L = 0.20 (LSDT & SGQMT)

After centralizing the outliers, data scatter measure S with respect to the directly calculated global quadratic bisector is 0.34, whereas S_L = 0.35, $S_{TrialQuadratic}$ = 0.29. Data groups centers scatter measure is 0.046 for the trial and 0.043 for the groupwise calculated global quadratic bisectors. Coordinate partitionwise data groups centers scatter measure is 0.17 and 0.18 for the trial and the coordinate partitionwise calculated global quadratic bisectors. Groupwise centralizing the given data so drastically reduces data scatter that LSDT & GTMI, SGQMT, and even the least square method give almost coinciding global linear bisectors.
PBPT are very efficient in data modeling, estimation, approximation, and processing and reliable even by great data scatter, e.g. in aeronautical fatigue.

References

[1] Gelimson L. G. Providing Helicopter Fatigue Strength: Flight Conditions. In: Structural Integrity of Advanced Aircraft and Life Extension for Current Fleets – Lessons Learned in 50 Years After the Comet Accidents, Proceedings of the 23rd ICAF Symposium, Dalle Donne, C. (Ed.), 2005, Hamburg, Vol. II, 405-416

[2] Gelimson L. G. Overmathematics: Fundamental Principles, Theories, Methods, and Laws of Science. The "Collegium" All World Academy of Sciences Publishers, Munich, 2010

[3] Gelimson L. G. Fundamental Sciences of Estimation, Approximation, Data Modeling and Processing. The "Collegium" All World Academy of Sciences Publishers, Munich, 2010

[4] Gelimson L. G. Discretization Errors by Determining Area, Volume, and Mass Moments of Inertia. In: Review of Aeronautical Fatigue Investigations in Germany During the Period May 2005 to April 2007, Ed. Dr. Claudio Dalle Donne, Pascal Vermeer, CTO/IW/MS-2007-042 Technical Report, Aeronautical fatigue, ICAF2007, EADS Innovation Works Germany, 2007, 20-22